



HAL
open science

Fast scanning calorimetry combined with millisecond time-resolved x-ray micro-diffraction to study the reorganization phenomena in poly (ether ether ketone)

Mariia Vlasova

► **To cite this version:**

Mariia Vlasova. Fast scanning calorimetry combined with millisecond time-resolved x-ray micro-diffraction to study the reorganization phenomena in poly (ether ether ketone). Theoretical and/or physical chemistry. Université de Haute Alsace - Mulhouse, 2019. English. NNT : 2019MULH3542 . tel-03711807

HAL Id: tel-03711807

<https://theses.hal.science/tel-03711807>

Submitted on 1 Jul 2022

HAL is a multi-disciplinary open access archive for the deposit and dissemination of scientific research documents, whether they are published or not. The documents may come from teaching and research institutions in France or abroad, or from public or private research centers.

L'archive ouverte pluridisciplinaire **HAL**, est destinée au dépôt et à la diffusion de documents scientifiques de niveau recherche, publiés ou non, émanant des établissements d'enseignement et de recherche français ou étrangers, des laboratoires publics ou privés.

Année 2019

UNIVERSITÉ DE HAUTE-ALSACE

UNIVERSITÉ DE STRASBOURG

THESE

Pour l'obtention du grade de

DOCTEUR DE L'UNIVERSITÉ DE HAUTE-ALSACE

ECOLE DOCTORALE: Physique et Chimie-Physique (ED 182)

Discipline: Chimie des matériaux

Présentée et soutenue publiquement

par

Mariia VLASOVA

le 25 octobre 2019

**FAST SCANNING CALORIMETRY COMBINED WITH
MILLISECOND TIME-RESOLVED X-RAY MICRO-DIFFRACTION
TO STUDY THE REORGANIZATION PHENOMENA IN
POLY(ETHER ETHER KETONE)**

Sous la direction de: Prof. Dimitri IVANOV et Dr. Martin ROSENTHAL

Jury:

Prof. Dario CAVALLO	Universita degli Studi di Genova	(Rapporteur)
Prof. Bart GODERIS	KU Leuven	(Rapporteur)
Prof. Andrei PETUKHOV	Utrecht University	(Président)
Dr. Larissa Tsarkova	DTNW - Universität Duisburg-Essen	(Examinateur)
Prof. Dimitri A IVANOV	IS2M, Université de Haute-Alsace	(Directeur de these)
Dr. Martin ROSENTHAL	ESRF- The European Synchrotron	(Co-directeur de these)

There is a Russian novel written by Boris and Arkady Strugatsky - “Понедельник начинается в субботу” or “Monday Begins on Saturday” when translated into English. It tells of an idealistic world in which the scientists of a research institute accepted the working hypothesis that “happiness lays in continuous exploring of the unknown and that this is the meaning of life”. And as the title tells, the scientists disregarded weekends and believed that every Monday begins on Saturday. The same atmosphere I observed at the beamline where I was having the chance to do my PhD work. When experiments lasted through whole days and nights and the scientists continued to solve scientific problems with an endless enthusiasm accompanied by huge debates about one or another scientific issue.

Acknowledgements

Most cordially I want to thank my PhD supervisors: Dr Dimitri A. Ivanov and Dr Martin Rosenthal for their scientific guidance through all three years of my PhD. I want to thank them for sharing scientific knowledge, and also for their patience and time. I want to thank Dimitri Ivanov for the possibility to perform my experiments at BM26, for the assistance with the DSC measurements in UHA, for the help with designing experiments, for the new insights and ideas. I want to thank Martin Rosenthal for the continuous support during my PhD work, for the long hours of scientific discussions, for the help, explanations, for the technical and scientific input during all experiments.

I am especially grateful to Manfred Burghammer for his great consideration to my PhD project, for his help during beamtimes at ID13, for the discussions, for his critical reading of the manuscript, for the help with all official formalities. Furthermore, I want to thank him for the freedom of participating in workshops, summer schools and conferences.

Special thanks to Christian Riekkel for our experiments with the micro-droplet system, for the discussions and encouragement during my PhD work, for sharing his experience.

I warmly thank all the rest of ID13 team: Tilman Grünewald, Andreas Johannes, Michael Sztucky and Lionel Lardiere, for their help with experiments, for all the advice, and for the encouraging me.

Apart from the colleagues mentioned before, I want to thank Daniel Hermida, Sarah Saidi and Michela Brunelli from BM26B beamline for the technical support during beamtimes and help with the sample preparation.

I want to thank the group of colleagues from the PSCM laboratory with Diego Pontoni being in charge, for sharing of part of their laboratory to accommodate our nanocalorimetry setup after the beginning of the long shutdown.

I want also to thank Clement Girard for the help with DSC measurements in UHA.

My personal thanks to Anastasiia Shilova for the information about this PhD position and for the support after my arrival. I want to thank Mikhail for the encouragement in the time of interviews and for the freedom to choose my way in life. I want to thank Oonagh and Martin for the time when we shared the same office. It was a great time. I want to thank Oonagh for our long discussions, for her support. I want to thank Marija for our coffee-breaks conversations, for her wisdom, for the advice she gave me. I want to thank Philip and Camille for the British-style dinners and long-long conversations. I want to thank all my friends here in Grenoble and also in Russia for their trust in me. I want to thank Vladimir for his love, endless patience and support during the last two years.

I want to thank my parents for my education, for their trust and love.

I would also like to thank the members of the jury for reading this manuscript.

I also would like to thank the IS2M (CNRS) in Mulhouse for hosting me as a PhD student at the UHA and for providing the possibility to utilize infrastructure and laboratories and to conduct complementary thermal analysis measurements. I would like to thank an engineer Gautier Schrodj for help with providing DSC measurements.

Finally, I would like to acknowledge the ESRF for the funding of the PhD programs and for the possibility for the thesis students to work at the ESRF.

Table of Contents

1	Introduction.....	1
2	A brief background in polymer crystallization and analysis.....	3
2.1	Polymer crystallization.....	4
2.1.1	Crystallization of small molecules and polymers: a comparative analysis.....	5
2.1.2	Crystallization theories - a historical overview.....	6
2.1.3	Melt-crystallized polymers: morphology and growth from the melt.....	8
2.1.4	The Hoffman-Lauritzen theory.....	10
2.1.5	Gibbs-Thomson equation for polymer crystal melting.....	15
2.1.6	Lamellar thickness.....	16
2.1.7	Gibbs-Thomson equation applied for the lamellar crystal.....	16
2.1.8	Hoffman-Weeks plot.....	19
2.1.9	Avrami kinetics.....	20
2.1.10	The phenomenon of polymer recrystallization.....	24
2.2	Thermal analysis of polymers.....	26
2.2.1	DSC instrumentation and formalism.....	27
2.2.2	Thermal characteristics of polymers.....	28
2.2.3	Main events on DSC curve.....	29
2.2.4	Effect of polymer molecular rigidity on thermal properties.....	30
2.2.5	Limits of DSC.....	31
2.2.6	Nanocalorimetry.....	31
2.2.7	Combination of nanocalorimetry with X-rays.....	37
2.3	X-ray analysis of polymers.....	38
2.3.1	Bragg's law.....	39
2.3.2	X-ray powder diffraction.....	41
2.3.3	Structural parameters from X-ray powder diffraction pattern.....	43
2.3.4	Scherrer equation.....	47
2.3.5	Crystallinity in polymers from 1D powder diffraction curves.....	48
2.4	Synchrotron radiation.....	52
2.4.1	ESRF storage ring.....	53
2.4.2	ID13 generic description.....	54
2.4.3	BM26 beamline.....	57
3	Polyetheretherketone state of art and open questions.....	59
3.1	PEEK a high-performance polymer.....	60
3.2	Physical parameters and crystalline structure.....	60

Table of Contents

3.3	The complex thermal behavior of PEEK	65
4	A new approach: nanocalorimetry vs. time resolved micro-XRD	79
4.1	Custom developed Nanocalorimeter	80
4.1.1	The MEMS-based calorimetric sensor	80
4.1.2	Working modes of the Nanocalorimeter.....	82
4.1.3	Calibration of the calorimetric sensor	83
4.1.4	Thermal gradients and the extrapolation of the sample temperature.....	90
4.1.5	Shape of peaks and time constants in nanocalorimetry	92
4.1.6	Thermal lag of the Nanocalorimeter.....	94
4.1.7	High-temperature version of the Nanocalorimeter	96
4.1.8	Technical aspects of the sample preparation	98
4.2	Nanocalorimetry combined with microfocus X-ray diffraction	100
4.2.1	Sample holders	100
4.2.2	The X-ray micro diffraction setup.....	103
4.2.3	Analysis of two dimensional X-ray diffraction data.....	110
4.2.4	Peak fitting algorithms used for analysis of diffraction data	111
4.2.5	Challenges	113
5	Calorimetry vs X-ray micro-diffraction to address the recrystallization phenomenon in PEEK	121
5.1	The double-melting of PEEK accessed by nanocalorimetry	122
5.1.1	Thermal programs and nanocalorimetric data analysis	122
5.1.2	Slow DSC vs. fast chip calorimetry.....	126
5.1.3	Hoffman-Weeks analysis of the first melting peak	132
5.1.4	Hoffman-Weeks analysis of the second melting peak.....	135
5.1.5	The double melting of PEEK	139
5.1.6	Recrystallization diagram from calorimetry	140
5.1.7	Early stages of crystallization in PEEK.....	141
5.2	The double-melting of PEEK by fast chip calorimetry and WAXS.....	146
5.2.1	Structural Signature of PEEK during heating.....	146
5.2.2	Recrystallization and critical heating rates in PEEK.....	150
5.2.3	Recrystallization diagram from calorimetry and X-ray micro-diffraction.....	155
6	Conclusions and Outlook.....	157
7	References.....	167

List of abbreviations

Materials:

LLDPE – Linear Low Density Polyethylene

HDPE – High-Density Polyethylene

P3HT – Poly(3-hexylthiophene)

PAEKs – Polyaryletherketone polymers

PE – Polyethylene

PEEK – Polyetheretherketone

PEKs - Polyetherketons

Techniques:

AFM – Atomic Force Microscopy

DSC – Differential Scanning Calorimetry

DTA – Differential Thermal Analysis

FSC – Fast Scanning Calorimetry

MDSC – Modulated Differential Scanning Calorimetry

SAXS – Small-Angle X-ray Scattering

SEM – Scanning Electron Microscopy

TEM – Transmission Electron Microscopy

WAXD – Wide-Angle X-ray Diffraction

WAXS – Wide-Angle X-ray Scattering

XRD – X-ray Diffraction

Other:

A_a – Area of an amorphous phase

A_c – Area of a crystalline phase

AC – Alternating Current

BM – Bending Magnet

DC – Direct Current

ESRF – European Synchrotron Radiation Facility

FWHM – Full-Width at Half Maximum

ID – Insertion Device

LH-theory – Lauritzen-Hoffman Theory

q – Scattering Vector

X_c – Crystallinity Index

1 Introduction

The study of structure and properties of polymer materials is currently in the focus of both fundamental and applied science. Understanding correlations between the thermal properties and structure of semicrystalline polymers is important for a variety of practical applications. However, the metastable nature of the nanometer-sized polymer crystals results in their notoriously complex thermal behavior, which is largely dependent on the thermal history.

Since about 60 years, there is an intense on-going discussion on the so-called multiple melting behavior pertinent to many commodity semicrystalline polymers. This phenomenon consists of the presence of multiple melting peaks in the DSC traces of polymers which do not exhibit polymorphism. Such thermal behavior is particularly pronounced for the semicrystalline polymers belonging to the semi-rigid chain family. In order to explain the origin of multiple melting peaks in the DSC traces of these polymers, several models were put forward, however, no consensus was found to explain entirely the phenomena observed. One of the widely discussed models, the so-called “melting-recrystallization model”, assumes that the multiple melting originates from a continuous process of melting and recrystallization operating on heating. During this process, the metastable crystals initially formed at low temperature would recrystallize at a higher temperature to form more stable crystals.

The reason why the conventional combination of calorimetry with X-ray scattering has not yet provided a comprehensive answer on this question is due to the fact that the reorganization processes can operate on the scale of a millisecond, i.e. in the range which has been until recently absolutely inaccessible by the classical calorimetry and X-ray scattering. Multiple-melting behavior of semi-rigid chain polymers can be a manifestation of the structural reorganization processes occurring during thermal analysis itself. If such a reorganization is indeed taking place during the experiment, one cannot get any information on the initial state of the material because it would uncontrollably evolve during temperature scanning.

Taking into account the fact that the classical thermal analysis techniques are inadequate for the comprehension of the described phenomenon, with this work, we are aiming at employing the technique of fast scanning calorimetry (FSC), or nanocalorimetry instead. This technique operates at much higher heating or cooling rates and, therefore, allows monitoring the

reorganization processes operating at the scale of a few milliseconds. The phenomenon of multiple melting behavior was explored using PEEK as a typical semi-rigid chain commodity polymer. The term “recrystallization” or “reorganization” is often used when discussing the multiple-melting behavior of PEEK. However, there still is no experimental evidence for structural changes during such a reorganization process, produced by application of X-ray diffraction methods. In addition, the reported rate of the recrystallization process was estimated by means of solely nanocalorimetry measurements¹ and did not have the corresponding information on the structural transitions. In the current work, the necessary structural information was obtained with an experimental setup combining nanocalorimetry and *in-situ* X-ray scattering available at the ID13 beamline of the European Synchrotron Radiation Facility (ESRF).

In the present manuscript, the development of a setup combining fast chip calorimetry *in-situ* with X-ray micro-diffraction to study the thermal behavior of PEEK is extensively discussed in Chapter 4. It also contains an overview of the working principles of the home-built nanocalorimetric device, the new calibration procedure for the employed MEMS-based nanocalorimetry sensors and a detailed discussion of the calorimetric data treatment related to experiments with nanocalorimetry heat-flux devices. Chapter 4.2 contains detailed information about the integration of the nanocalorimetry device to micro-focus beamline ID13, ESRF including information about the beamline optical arrangement used, as well as synchronization scheme for all devices in order to perform time-resolved measurements with millisecond resolution. Chapter 4.2 also contains information about X-ray data treatment and analysis and a discussion about challenges and compromises which had to be made when performing such measurements. Ways to manage radiation damage induced by X-ray exposure of PEEK samples in order to assure the validity of *in-situ* heating experiments are discussed in the same Chapter 4.2.5.

Chapter 5 is devoted to discussion of the results on PEEK multiple-melting behavior obtained by nanocalorimetry measurements, describing the setup combining fast chip calorimetry *in-situ* with X-ray micro-diffraction. The process of PEEK recrystallization will be extensively discussed from both, a purely calorimetric and also a structural point of view, via observation of the movement of melting peaks with respect to the employed heating rate and crystallization conditions. The structural signature of the recrystallization process can be found in the results of X-ray measurements. Finally, conclusions about the critical heating rate of recrystallization in the dependence of different crystallization

2 A brief background in polymer crystallization and analysis

This chapter presents a short overview of the existing models of polymer crystallization and melting. The specific features of the semi-rigid chain polymers' thermal behavior will be discussed and compared to those of flexible chain polymers, and the concept of polymer recrystallization will be introduced and described. Two main techniques employed in the current work, i.e. the thermal analysis and X-ray diffraction will be discussed in relation to polymer characterization.

2.1 Polymer crystallization

Polymers can exhibit different morphologies on the nanometer and micrometer level; these supramolecular structures dramatically affect their macroscopic properties. In the solid state, polymers can be amorphous, liquid-crystalline or semicrystalline, depending on the long range order in their structure. When the long range order is not present polymers can be viewed as amorphous liquids. In other cases, polymers exhibit in their structure regions with long range order, which can be similar to low-molecular weight liquid-crystalline or crystalline materials. For semicrystalline polymers, their structure and crystalline state define its different physical properties including thermal, mechanical and optical ones. For example, below the glass transition temperature, the amorphous polymers are usually firm and crisp because of the reduced mobility of their chain segments but by raising the temperature the molecular motion develops resulting in appearing of rubbery properties. In contrast to the amorphous polymers, the semicrystalline polymers have melting points above the glass transition temperature. Their elastic modulus changes significantly only at the corresponding high (melting) temperature.

The degree of crystallinity also results in the properties of polymers: higher crystallinity leads to higher thermal stability and firmness, but also makes the material more breakable whereas the unoriented regions add to the specimen elasticity and reinforce mechanical resistance. Thus, polymers with high crystallinity have a higher stiffness, tensile strength, hardness and are more resistant to solvents and high-temperature conditions, but they are often more brittle and less impact resistant.

It was observed that the ability of a polymer to crystallize depends on different parameters including their chemical structure. For example, crystallization can occur much readily in the case of isotactic polypropylene than in the syndiotactic form. Atactic polymers have the ability to crystallize only when the side groups are relatively small, i.e. as in polyvinyl alcohol and they do not crystallize in the case of large substituents. Crystallinity is also affected by other different factors such as crystallization temperature and previous thermal history, cooling rate, and in the special case of strain-induced crystallization, by the drawing ratio, strain rate, and by the processing conditions of the material. This chapter has aim to provide a general view of polymer crystallization and answer the basic questions such as why polymers, in general, have the ability to crystallize and in what manner. Does it happen in the

same way as for small molecules? The chapter also includes a discussion on the most important crystallization theories and models.

2.1.1 Crystallization of small molecules and polymers: a comparative analysis

As stated above, crystallization is the process of forming solid material from a solution or melt, whereby the solid material formed has a highly organized crystalline (as opposed to amorphous) structure. Crystallinity is usually induced by cooling a melt or a dilute solution below its melting (dissolution) temperature.

A study of polymer crystallization can be started with a consideration of related but simpler systems – sharp oligomer fractions. These are molecules that consist of a few repeating units with a sharp distribution of molecular mass in contrast to a typical polymer where the number of monomers is much larger and which can have a broad distribution of molecular weights. Oligomers were found to readily crystallize in the following way: The crystals are composed of stacked layers, each layer being assembled of chain molecules with identical conformations.² The endgroups of the molecules occupy the interfaces. Oligomer molecules in the melt exist in coiled conformations just like polymers. In order to form a crystal, these chains have to be straightened and separated from each other and then attached to the growing lateral crystal surface.

Polymers with a uniform molecular weight can form the same type of crystal composed of extended straight chains with the endgroups disposed in planar interfaces, and this would represent the equilibrium state with the lowest free energy. However, in most cases, the semicrystalline morphology is more complex. In reality, in the melt the polymer coils interpenetrate each other. Polymer crystallization with extended chains requires eliminating the entanglements, which can be problematic within the time frame of the process. Reaching the state of complete disentangling can take too long time because of the necessity to overcome an extremely high entropic activation barrier. For kinetic reasons cooling the polymer melt below the melting point produces semi-crystalline structures and there exist plenty of examples of such systems such as linear polyethylene (PE), polyethylene terephthalate (PET), polytetra-fluoroethylene (PTFE) or isotactic polypropylene (PP).

The structure of the lamellar semi-crystalline polymers can be viewed (at a certain level of simplification) as a two-phase layered system which consists of crystallites separated by

amorphous disordered regions. So the formation of two-phase structures in polymer systems can be seen as a natural way to deal with entanglements as well as with chemical defects in the chain like endgroups, chain branches, etc. The solid-liquid segregation process which occurs during crystallization shifts them into amorphous regions accompanied by reeling the chains from the melt, stretching and incorporating them into a growing crystal.

During polymer crystallization, the structure formation process is governed by kinetic criteria rather than by equilibrium thermodynamics. The structure which develops at a given temperature is the one with the maximum growth rate rather than the one with the lowest free energy. As a consequence, the treatment of the crystallization behavior of polymers requires kinetic considerations. Being kinetically controlled, the structures of partially crystalline samples are always stronger affected by the processing conditions and thermal history, i.e. temperatures and times of crystallization, cooling rates, etc.

2.1.2 Crystallization theories - a historical overview

The early studies on crystalline polymers were based on the X-ray diffraction technique³. Bragg diffractions of the polymers were broad and diffuse compared to the Bragg peaks of well-developed small-molecule single crystals, and these features were attributed to small crystal sizes as well as the existence of defects.

Diffraction experiments with macroscopic X-ray beams provided insights that polymer crystals were several nanometers in size, randomly oriented in space and comprising about 30-80% of the material. The fact that polymer chains were much longer than the crystal dimensions pushed the development of models which can explain this. Thus, the earliest one was the 'fringed micelle' model proposed by Herrmann et al.⁴ having the aim to explain the crystalline state of natural polymers as gelatin and starch (Figure 2.1). According to this model, the polymer in a crystalline state looked like a three-dimensional network composed of micro-crystallites which crosslink amorphous regions of flexible-coil chain segments and where crystallized segments of one macromolecule belong predominantly to different crystals⁴

Later, this model was criticized by Flory⁵ who calculated the free energy of the fringed micelle model and found that the non-crystalline parts located at crystal surfaces were overcrowded, which limited the motion of these amorphous chains, leading to a large amount

of the conformational entropy loss. In addition, Zachmann⁶ estimated the optimal aspect ratio of the fringed micelle and identified that it could be up to 56.8. In the disordered liquid state, the formation of such substantially asymmetrical fiber-like structures is quite difficult to imagine from spontaneous fluctuations. In addition to that, the fringed micelle model could not readily explain the growth of such generally spherical symmetrical superstructures as spherulites whose existence was first found experimentally⁷.

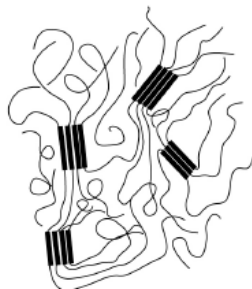


Figure 2.1 Schematic representation of the fringed micelle model, taken from⁸

In 1938 Storks³ in a work on synthetic linear polyesters observed very thin lamellar crystals. Considering that the polymer chain is much longer than the lamellar thickness he declared that the polymer chains are folded back and forth upon themselves in such a way that the neighboring straight sections remain parallel. It was the first step toward developing the folded chain model of lamellar crystals.

Before 1957, several research groups⁹⁻¹¹ almost simultaneously obtained polyethylene single crystals. Keller's work in which he indicated that the molecular backbone is oriented along the thinnest dimension of the crystal and could be extended in a continuous manner no more than 10 nm was of primary importance. Analysis of the corresponding diffraction patterns revealed that the chain molecules are in parallel alignment within the crystals like an assembly of parallel strings of beads. The beads (the atoms along the chain), defined a three-dimensional lattice repeating, for the purposes of traditional structure analysis, indefinitely. The strict periodicity in the direction along the molecular backbone is naturally limited to the extension of the molecule¹². Investigating the low-angle X-ray scattering Keller found the periodicity of 120 Å, which was produced by the layered structure of the single crystals. The latter was interpreted as resulting from the regularity of chain folding.

Based on electron diffraction patterns, Keller⁹ proposed a reliable physical picture of the organization of the polymer chains in the lamellar crystals, which is known as the “folded chain model”. In this model, Keller assumed that a polymer chain should fold back and forth on itself in an adjacently re-entered manner (Figure 2.2).

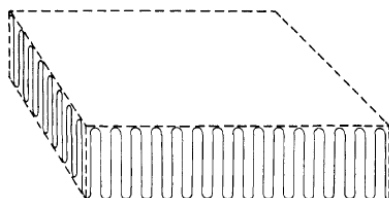


Figure 2.2 Schematic representation of chain folding in polymer crystals according to Keller¹²

Since its very discovery, the folded chain model became widely accepted and the formation of folded chain crystals has been proven to be a common morphological habit. Such a model fits particularly well to the case of dilute solutions. In such a system polymer coils are separated from each other. Apart from several exotic cases (e.g., anabaric polyethylene) the extended-chain polymer crystals correspond to the most thermodynamically stable but kinetically unfavorable state.

2.1.3 Melt-crystallized polymers: morphology and growth from the melt

As described by Keller at the molecular level, polymer chains align perpendicular or at a small angle to the lamella surface via chain folding⁹. Because of the very small thickness of the crystallites along the chain direction, a single polymer chain must penetrate the crystallite from which it originates many times.

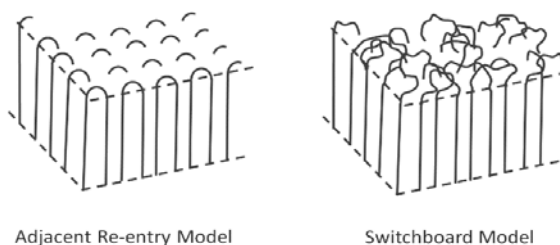


Figure 2.3 Models of chain folding

The natural trend of a polymer chain surrounded by other chain-like objects is to penetrate with neighboring chains rather than individually collapse because the resulting entangled configuration retains the maximal entropy^{13,14} and thus eventually forms an intertwined network structure, which is frequently referred to as “entanglement”. Entanglements lead to a certain type of topological constraints, which force the polymer chain to move along its contour path.¹⁵

Two variants of the model can potentially describe the polymer chain folding⁵: a random (switchboard) model, where polymer chains fold at random, or, alternatively, the polymer chains are regularly folded, making hairpin turns at the surface, which is known as the adjacent re-entry model (Figure 2.3)

Flory⁵ demonstrated that the adjacent re-entry model cannot precisely describe the crystal formation in long-chain molecules. He demonstrated that a significant amount of chains not returning to the lamella after departure from it. Furthermore, the re-entry of the folded polymer chains at the lamellar surface causes some disorder because polymers usually do not fold regularly along the growth plane. In many cases, the re-entry of the polymer chains is completely random which creates a diffuse phase boundary. Only in a few cases, polymer chains fold back into the lamellae in an ordered pattern.⁵ Thus, an irregular re-entry model with variable lengths of chain loops was proposed. It also happens that some chains do not re-enter the same lamella. Such chains may eventually come back to the amorphous region or re-enter at a distant location or enter other crystals. This conformation of chain folding is often referred to as the switchboard model for the irregular entrance and exit of chains from the lamella surface which makes the lamella look like old switchboards.¹⁶ The switchboard model can be also applied to explain the melt crystallization^{17,18} and also confirms the existence of multi-layer crystals and loose end chains which were found by small-angle neutron scattering experiments of melt-crystallized polymers^{19,20}.

Flexible chain polymers such as polyethylene will mainly re-enter the lamellae at adjacent points when slowly crystallized whereas fast cooling will result in some random re-entry at distant locations. Another small portion of the chain ends remains in the amorphous phase or enters a neighboring lamella. In many other cases, polymer crystal growth with adjacent re-entry in the melt is either not possible or very unlikely. For example, polymers with a semi-rigid backbone such as PEEK or PES are incapable of adjacent re-entry as these polymers

cannot bend over short distances, and hence, can only re-enter the crystal several stems away from the exit point, whereas stiff polymers such as liquid crystals will predominantly enter other crystals and/or a large portion of the chains will remain in the amorphous phase.

Branching of polymers will also affect the structure and degree of crystallinity. For example, short branches such as butyl, hexyl and octyl, which are intentionally introduced in linear low density polyethylene (LLDPE), reduce the overall crystallinity and the size of the spherulites whereas long branches can undergo side-chain crystallization in the same manner as the backbone. Branching also increases the amorphous portion in the spherulites because side chains disturb the lamellar growth.

2.1.4 The Hoffman-Lauritzen theory

There are two most important models employed for the analysis of polymer crystallization kinetics: The Avrami equation and the Hoffman-Lauritzen growth theory.

The Hoffman-Lauritzen theory (HL)²¹ is a theory which was developed in the 1960s by John D. Hoffman and coworkers. It describes the polymer crystallization process as a system of differential equations describing the kinetics and thermodynamics of conversion of the chain molecules in the random coil conformations to the chain-folded lamellar crystals. The theory employs the notion of lateral growth, which is a surface-nucleation controlled process, to describe the growth rates of polymer lamellar crystals. An existing crystal with a defined atomically smooth surface provides the template for the crystal growth. The chain molecules deposit onto the growth plane one stem at a time to form a lamella. The crystal growth rate perpendicular to the growth front is constant at a constant T_c .

The elementary process involved in the HL theory consists of two steps: the creation of a new nucleus and lateral growth. In the initial stage, as shown in Figure 2.4, a molecular stem each of the length comparable to the lamellar thickness L loses conformational entropy by attaching to the smooth crystal growth surface, whose lateral dimension is denoted further as L_p . After this step, the secondary nucleus spreads out laterally at a rate g . The thickness of the stem a is along the lateral direction and b is along the growth direction with growth rate G . This process, which is called surface nucleation, or secondary nucleation, generates two new lateral surfaces, leading to an increase of the overall free energy:

$$\Delta G_1 = -abL\Delta\mu + 2bL\sigma \quad (\text{Eq. 2.1})$$

Two new lateral surfaces, each of area bL , are created in this step. Since the first stem does not generate any chain folds on the fold surfaces, the free-energy cost associated with the fold surface areas ($2ab$) is ignored for the first stem. According to the model, the first step is associated with the largest free-energy barrier that consequently determines the growth rate (Figure 2.5). The value of the barrier increases with increasing lamellar thickness L . The initial and final states of this step are assumed to be separated by a free-energy barrier, which is taken to be the lateral surface free energy ($2bL\sigma_l$) reduced by an arbitrary fraction of the free energy of crystallization ($abL\Delta\mu$) for the forward process.

$$\Delta G_1^* = -\psi abL\Delta\mu + 2bL\sigma_l \quad (\text{Eq. 2.2})$$

For the reverse process the barrier is $(1-\psi)abL\Delta\mu$, where ψ is the so-called “apportioning” parameter. The free-energy change associated with the second stem (with the first fold) is:

$$\Delta G_2 = -abL\Delta\mu + 2abL\sigma_f \quad (\text{Eq. 2.3})$$

The initial and final stages of the deposition of the second stem are assumed to be separated by the following barrier:

$$\Delta G_2^* = -\psi abL\Delta\mu + 2abL\sigma_f \quad (\text{Eq. 2.4})$$

The barrier for the reverse direction of the second step is $(1-\psi)abL\Delta\mu$. The free-energy changes associated with the lateral attachment of subsequent stems are the same as for the second stem.

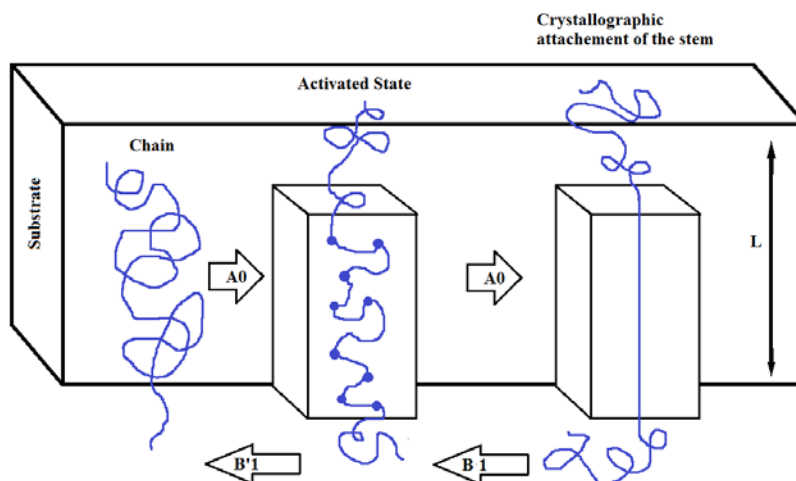


Figure 2.4 Scheme of the activated complex formation and its transformation to a crystallographically attached first stem. A_0 – is the slowest, time-limiting process

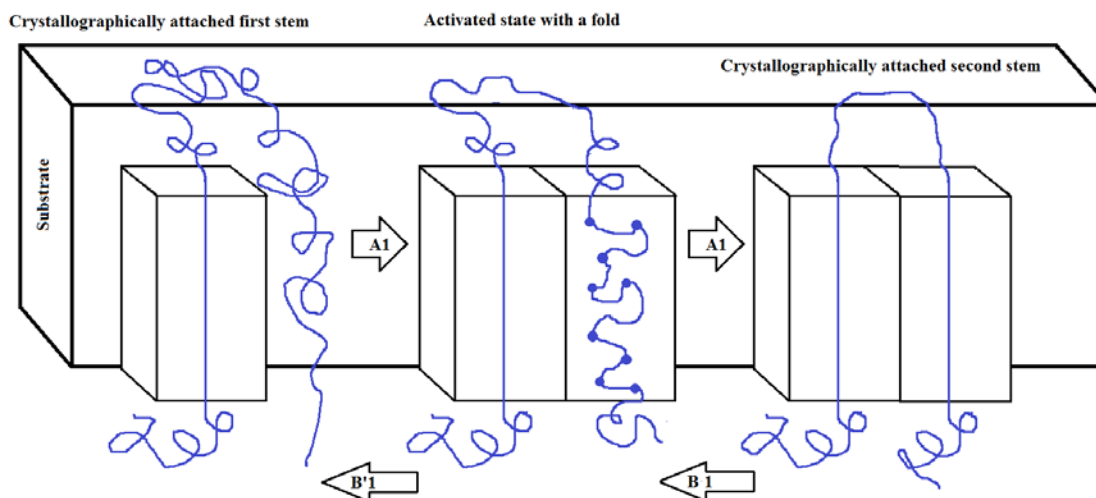


Figure 2.5 Scheme of the activated complex formation and its transformation to a crystallographically attached second stem with a fold

In the following steps, subsequent stems fold back and are deposited adjacent to the attached stems to further lower the overall free energy until reaching a negative global free energy change. Figure 2.6 shows the connection between rate constants A_0 , A , B and a free-energy of the process of folded polymer crystal formation.

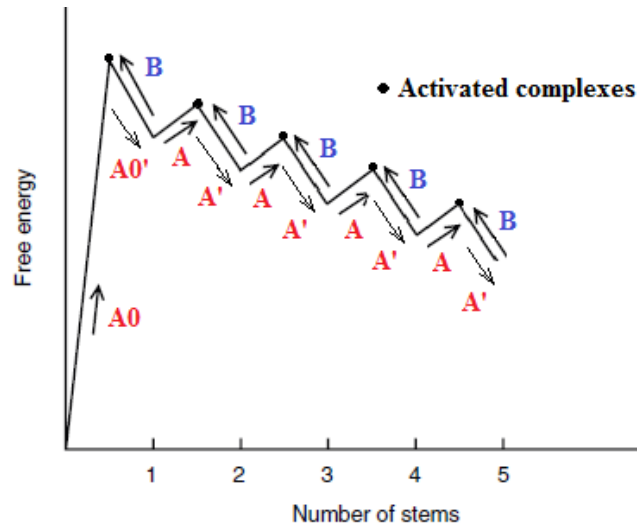


Figure 2.6 Free-energy landscape of the LH-model with corresponding barriers for fast, slow and backward steps

The rate constant of each step can be expressed with an Arrhenius equation:

$$A_0 = \beta \exp(-2b_0\sigma_l/KT), \quad (\text{Eq. 2.5})$$

$$B = \beta \exp(-a_0b_0L(\Delta G)/KT), \quad (\text{Eq. 2.6})$$

$$A = \beta \exp(-2a_0b_0\sigma_e/KT), \quad (\text{Eq. 2.7})$$

where A_0 is the rate constant of the activated state formation, B is the rate constant of the detaching of one stem back, A is the rate constant of deposition of one following stem to a surface, and β accounts for the approach rate of polymer segments at the growth front.

The flux of stems through the nucleation barrier is constant and is given by the balance equation:

$$S = v_0A_0 - v_1B = v_1A - v_2B = v_2A - v_3B = \dots, \quad (\text{Eq. 2.8})$$

where v_i is a number density of systems with i stems in the growth layer. Thus,

$$v_1 = 1/A(S + v_2B) \quad (\text{Eq. 2.9})$$

Substituting ((Eq. 2.9) in ((Eq. 2.8) we obtain:

$$S \left(1 + \frac{B}{A} \right) = v_0 A_0 - (B^2/A)v_2 \quad (\text{Eq. 2.10})$$

then

$$S(1 + B/A + B^2/A + \dots) = v_0 A_0 \quad (\text{Eq. 2.11})$$

so for the flux:

$$S = v_0 A_0 (1 - B/A) \quad (\text{Eq. 2.12})$$

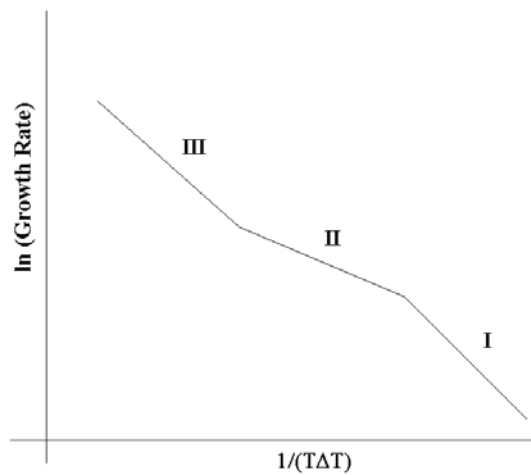


Figure 2.7 Three regimes in the LH model; figure adapted from²²

The HL theory uses three growth regimes, depending on the value of undercooling (ΔT). The Lauritzen–Hoffman plot models these regimes when $(\log G) + U^*/k(T-T_0)$ is plotted against $(T\Delta T)^{-1}$.²² It can be used to describe the rate at which secondary nucleation competes with lateral addition at the growth front among the different temperatures. This theory can be used to help understanding the preferences of nucleation and growth based on polymer properties such as its standard melting temperature. The three regimes are schematically shown in Figure 2.7.

Chain sliding diffusion model

Chain sliding diffusion model was proposed by Hikosaka²³ as another model of polymer crystallization when existence of extended-chain crystals of PE were observed in the

experiments where special conditions such as high pressure were used during crystallization. The term “chain sliding diffusion” describes the self-diffusion of a polymer chain along its chain axis direction⁸ and the phenomenon was explained by high chain mobility along the chain direction of the new phase of PE grown under high pressure. The chain sliding model adds to the classical HL model the ability of chains to move not only laterally but also along the chain direction. Such movement potentially can lead to a recrystallization phenomenon in polymers which will be described in 2.1.10. However, besides PE, only few polymers can exist in a form of extended-chain crystals⁸: polychlorotrifluoroethylene, polyvinylidene difluoride, trans-1,4-polybutadiene, and polyethylene terephthalate blend with bisphenol A polycarbonate²⁴ and there is no evidence that PEEK can be found in a form of extended-chain crystal. According to this, during further discussion of complex thermal behavior of PEEK the model of chain sliding diffusion will not be accounted as an explanation of the recrystallization phenomena in PEEK.

2.1.5 Gibbs-Thomson equation for polymer crystal melting

From thermodynamic considerations Gibbs free energy G of an infinite-sized polymer crystal below its melting point T_m should have a lower value than the corresponding volume in the liquid state because the negative value of ΔG is a necessary condition for any spontaneous process at constant temperature and pressure.

In the case of polymer crystals, the equilibrium melting temperature T_m^0 differs from the actual melting temperature, T_m . The latter depends on the fold length, or crystal thickness. From the kinetic point of view, the process of formation of the folded-chain crystals is faster because of the lower energy barrier compared with formation of fully extended chain crystals. As a consequence, the Gibbs free energy of folded-chain crystals is higher than that of the equilibrium extended-chain crystals, and they will, accordingly, melt at a lower temperature.

The thermodynamic driving force for crystallization from a liquid state to a folded-chain crystal at a given crystallization temperature T_c , can be written as:

$$\Delta G = \Delta H - T\Delta S \quad (\text{Eq. 2.13})$$

At the equilibrium melting temperature, T_m^0 , $\Delta G = 0$ and

$$T_m^0 = \Delta H / \Delta S \quad (\text{Eq. 2.14})$$

Substituting ((Eq. 2.14) into (Eq. 2.13) gives:

$$\Delta G = \Delta H(T_m^0 - T) / T_m^0 \quad (\text{Eq. 2.15})$$

At a particular crystallization temperature T_c , the driving force for crystallization can be expressed as:

$$\Delta G = \Delta H \Delta T / T_m^0, \quad (\text{Eq. 2.16})$$

where $\Delta T = (T_m^0 - T_c)$ is so-called supercooling.

2.1.6 Lamellar thickness

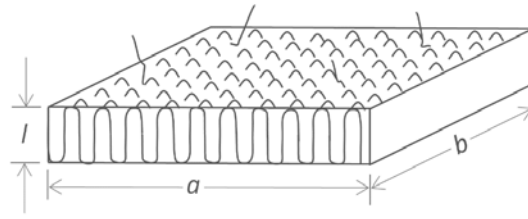
The initial lamellar thickness L depends on the crystallization conditions and degree of supercooling according to Organ and Keller²⁵:

$$L = C_1 / \Delta T + C_2, \quad (\text{Eq. 2.17})$$

where C_1 and C_2 are system-dependent constants related to the melting enthalpy and the surface free energy in at given crystallization conditions. When the lamellae are annealed at a given temperature, they may thicken with time. The thickening is usually continuous and L increases logarithmically with time. However, there are several examples, where the lamellar thickness increases in a stepwise manner²². As the thickening process continues, the lamellar thickness jumps discontinuously to three folds, and so on. This phenomenon is referred to as quantized thickening²⁶ and is typical for short (oligomeric) chains.

2.1.7 Gibbs-Thomson equation applied for the lamellar crystal

As mentioned before, the folded-chain crystals are metastable and melt well below the equilibrium melting temperature T_m^0 . The dependence of the melting point on crystal size can be described with the Gibbs-Thomson equation. In this model it is assumed that the thickness l of the lamellae is much smaller than its lateral dimensions.


 Figure 2.8 Lamellar crystal with chain folds, adopted from Keller¹²

The change in Gibbs free energy associated with the formation of crystalline lamellae consists of three terms; the first two terms describe the energy necessary to create new surfaces and the third is the bulk free energy of fusion:

$$\Delta G_{lam} = 2ab\sigma_e + 2l(a + b)\sigma - abl\Delta G_f \quad (\text{Eq. 2.18})$$

Where σ and σ_e are the surface free energy of the lateral and basal surfaces of the lamella (Figure 2.8). Both σ and σ_e are considered constants that are difficult to measure or to calculate, that is, usually only estimates exist. In many cases, $l \ll a, b$, so that the contribution of σ to the crystal energy can be neglected,

$$\Delta G_{lam} \approx 2ab\sigma_e - abl\Delta G_f \quad (\text{Eq. 2.19})$$

At the melting point of the crystal $\Delta G_{lam} = 0$, thus

$$\Delta G_f \approx 2\sigma_e/l \quad (\text{Eq. 2.20})$$

The free energy of fusion for infinite-sized crystal at equilibrium melting point T_m^0 involves both enthalpic and entropic changes:

$$\Delta G_f^\infty(T_m^0) = \Delta H_f^\infty(T_m^0) - T_m^0 \Delta S_f^\infty(T_m^0) \quad (\text{Eq. 2.21})$$

Assuming that $\Delta S_f^\infty(T_m^0)$ and $\Delta H_f^\infty(T_m^0)$ show only a weak temperature dependence, both quantities have values very similar to those of an infinite large crystal which melts at T_m :

$$\Delta H_f^\infty(T_m^0) \approx \Delta H_f^\infty(T_m) \quad (\text{Eq. 2.22})$$

$$\Delta S_f^\infty(T_m^0) \approx \Delta S_f^\infty(T_m) \quad (\text{Eq. 2.23})$$

Thus:

$$\Delta G_f^\infty(T_m) = \Delta H_f^\infty(T_m^0) - T_m^0 \Delta S_f^\infty(T_m^0) \quad (\text{Eq. 2.24})$$

and

$$\Delta G_f^\infty(T_m) \approx \Delta H_f^\infty(T_m^0)(1 - T_m/T_m^0), \quad (\text{Eq. 2.25})$$

or

$$\frac{2\sigma_e}{l} = \Delta H_f^\infty(T_m^0)(1 - T_m/T_m^0). \quad (\text{Eq. 2.26})$$

This can be rewritten to give the Gibbs-Thomson relation:^{1,2}

$$T_m = T_m^0[1 - 2\sigma_e/l\Delta H_f^\infty(T_m^0)] \quad (\text{Eq. 2.27})$$

The equation allows to determine the dependence of the melting point T_m as a function of the lamellar thickness l . Also it serves for estimation the value of the equilibrium melting point T_m^0 and obtaining the surface energy σ_e . It is possible to obtain these quantities by plotting the observed melting points T_m vs $1/l_c$ where the value of σ_e can be computed from the slope, and the intercept gives the value of T_m^0 (Figure 2.9).

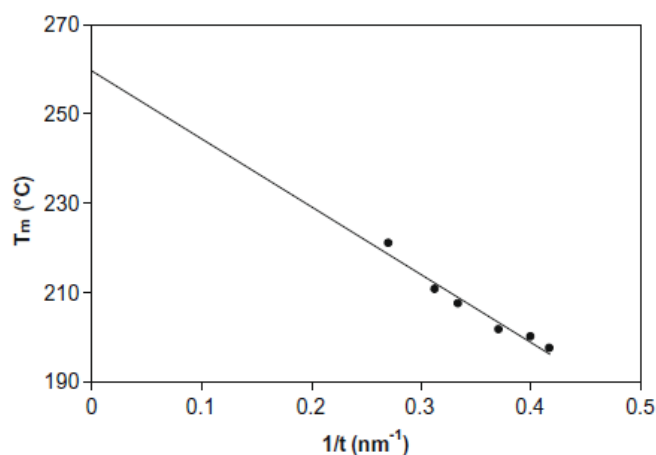


Figure 2.9 Gibbs-Thomson plot of melting temperature versus the reciprocal of lamellar thickness for poly(3-hexylthiophene) (P3HT)²⁷

The Gibbs-Thomson equation has been applied to many linear polymers such as isotactic polypropylene and polyethylene. It was shown to give reliable predictions of the melting point as a function of lamellar thickness.²⁸

2.1.8 Hoffman-Weeks plot

Hoffman and Weeks²⁹ proposed a different representation of the Gibbs-Thomson equation by linking the observed melting point $T_{m,obs}$ to its crystallization temperature T_c and equilibrium melting point $T_{m,\infty}$. To this end, the sample is crystallized isothermally at T_c and then subsequently heated into the main melting region at a specified rate. The experiment is then repeated for different T_c values. Hoffman, Lauritzen, and Weeks²⁹ found that the curves of $T_{m,obs}$ vs T_c can be described with the following relation:

$$T_{m,obs} \approx T_{m,\infty}(1 - 1/\gamma) + T_c/\gamma \quad (\text{Eq. 2.28})$$

The equilibrium melting point can be found at the crossing of these lines with the line $T_m = T_c$ (Figure 2.10) and γ is the thickening coefficient that can be computed by this method.

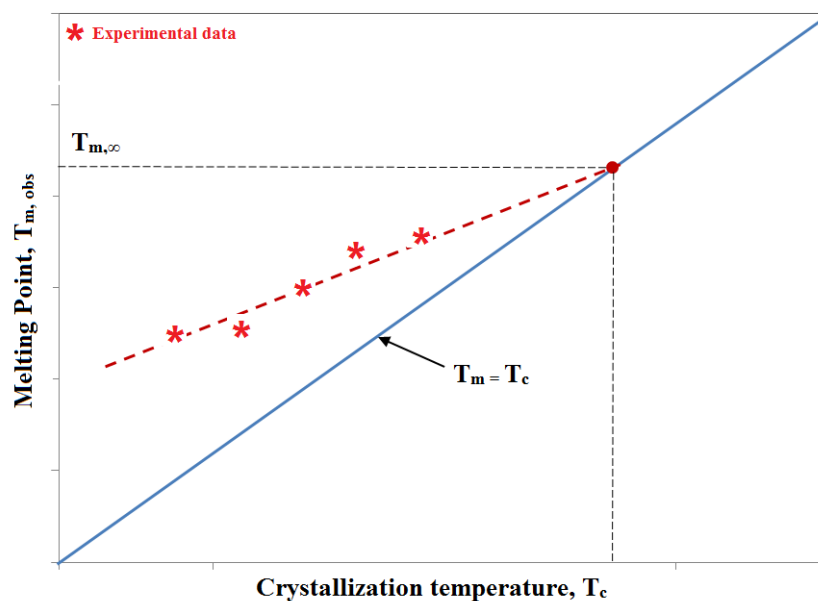


Figure 2.10 Hoffman-Weeks plot

2.1.9 Avrami kinetics

The Avrami equation describes the kinetics of phase transformations in solids. It can be also applied to other phase transitions in materials, such as chemical reactions, and can even be meaningful in analyses of ecological systems³⁰. The equation is also known as the Johnson-Mehl-Avrami-Kolmogorov, or JMAK, equation. The equation was first derived by Kolmogorov in 1937 and popularized by *Avrami* in a series of papers published from 1939 to 1941.^{31,32-33} *Avrami* in his works adapted the formulations originally intended for metallurgy to the needs of polymer crystallization, the original derivations were simplified and rearranged for polymer crystallization by *Meares* and *Hay*.³⁴ For the bulk crystallization of polymers, the overall crystallization kinetics can be represented as:

$$1 - X = \exp^{-vt}, \quad (\text{Eq. 2.29})$$

where X is the degree of crystallization, Vt is the volume of crystallization material.

Considering the two different cases:

- a) The nuclei are predetermined, they all develop at once on cooling the polymer;
- b) The crystals nucleate sporadically.

Considering the crystal has a spherical shape and is of a case:

$$dV_t = 4\pi r^2 L dr, \quad (\text{Eq. 2.30})$$

where r is the radius of the spherical crystal at time t , while L is the number of nuclei. Assuming the radius grows linearly with time, $r = kt$, by integrating ((Eq. 2.30) and substituting in ((Eq. 2.29) we obtain:

$$1 - X = \exp(-Kt^3), \quad (\text{Eq. 2.31})$$

where $K = (4/3)\pi k^3 L$ is a growth rate (Eq. 2.32)

For the case b , sporadic nucleation and the number of spherical nuclei is allowed to increase linearly with time at rate u . The nucleation is happening from time t_i to time t and will create a volume increase of:

$$dV_t = (4/3)\pi k^3 (t - t_i)^3 u dt_i \quad (\text{Eq. 2.33})$$

By integrating ((Eq. 2.33) between $t_i=0$ and t and substituting in (Eq. 2.29), we obtain:

$$1 - X = \exp(-Kt^4), \quad (\text{Eq. 2.34})$$

where $K = (1/3)\pi k^3 u$ (Eq. 2.35)

Both equations can be generalized and then the ratio of the crystalline phase, X , with respect to time, t , can be described by the following equation:

$$1 - X = \exp(-Kt^n), \quad (\text{Eq. 2.36})$$

or in a more common way:

$$X(t) = 1 - \exp(-Kt^n) \quad (\text{Eq. 2.37})$$

where n is the Avrami exponent, which depends on nucleation type and growth geometry ($n=3$ for spherical particles, $n=2$ for discs and $n=1$ for rods), K – is an overall crystallization

rate constant, depending on the type of nucleation mechanism, shape of the growing crystalline entities, and the amount and type of nucleation, X – volume fraction of crystallinity, t – crystallization time. If nucleation occurs concurrently with growth, for a 3D spherical particle, n can be 4 or 5 under various conditions and even non-integer values in real experiments for irregular-shaped particles (Table 2.1).

Table 2.1 Avrami exponents for various types of crystal growth geometry

Morphology	Instantaneous (Heterogeneous)	Sporadic (Homogeneous)
Rod	1	2
Disc	2	3
Sphere	3	4
Sheaf	5	6

Plotting $X(t)$ as a function of $\ln(t)$ we obtain a “S”- shaped crystallization curve (or sigmoidal profile) (Figure 2.11). It corresponds to low crystallization rates at the beginning and end but high in the middle.

During the intermediate period, the crystallization rate is rapid while there is still a sufficient amount of the parent phase. During this phase, the spherulites rapidly grow in radius. Closer to the end of the process there is only little untransformed material for the nuclei to form therein and the production of new particles becomes slow. Further, the particles already existing begin to impinge on each other, forming a boundary where growth stops.

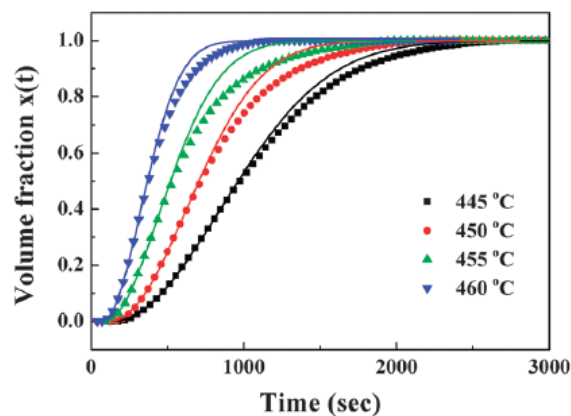


Figure 2.11 Isothermal transformed volume fraction x as a function of time at 445, 450, 455 and 460 °C for a LiNbO_3 glass. Points are data and the solid lines are fits using Johnson–Mehl–Avrami–Kolmogorov parameters³⁵

Complete crystallinity is almost never achieved, and the final degree of crystallinity is for example molecular-weight dependent²². The Avrami equation is analyzed in the double logarithm coordinates such as:

$$\ln[-\ln(1 - X)] = \ln K + n \ln(t) \quad (\text{Eq. 2.38})$$

Plotting the crystalline fraction X in the form $\ln[-\ln(1 - X)]$ as a function of $\ln(t)$ yields the characteristic Avrami plot (Figure 2.12). The initial slope of this plot gives the Avrami constant n , which with knowledge of the nucleation step can provide insights in the crystal geometry.

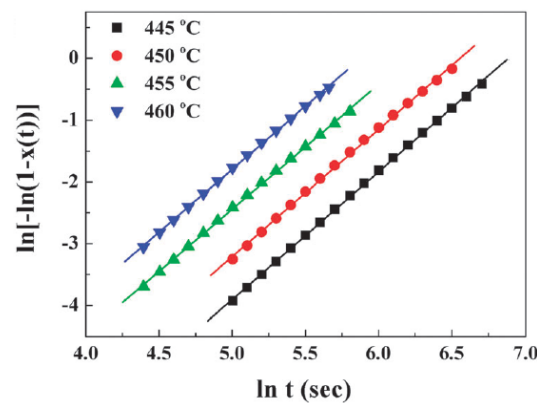


Figure 2.12 Johnson–Mehl–Avrami–Kolmogorov plot for the isothermal crystallization of the LiNbO_3 glass at various temperatures

The value of K is usually obtained by using the value of X at $t=t_{1/2}$, where $t_{1/2}$ is the half-time, i.e. the time required for the volume fraction of crystallinity to reach 50%. The volume fraction of crystallinity X can be obtained for example from the analysis of DSC curves as will be described in a following chapter. Knowing half-time of crystallization, one can obtain K as:

$$K = \ln 2 / t_{1/2}^n \quad (\text{Eq. 2.39})$$

The Avrami approach supposes several assumptions, as summarized from.^{35–38}

- (i) The nuclei are randomly distributed in the bulk;
- (ii) No volume change during the process;
- (iii) The growth rate is only dependent on temperature at a given pressure;
- (iv) Constant radial growth is assumed;

- (v) The nucleation rate is also only dependent on temperature at a given pressure;
- (vi) Constancy of growing shapes (sphere, disc, rod);
- (vii) Disappearance of potential nuclei when activated or absorbed.

In the case of polymer crystallization, the thermal conditions are much more complex, including non-isothermal crystallization and volume change. This explains often obtaining non-integer values of n in the experiments and difficulties to attribute the correct geometry to the system. Theoretical treatment requires the development of appropriate models to describe the associated kinetics.³⁸

2.1.10 The phenomenon of polymer recrystallization

After it was discovered that polymers crystallize in the form of lamellar structure, studies about changing this structure during thermal treatments appeared. Investigations of the changes in crystalline and amorphous structure were usually made by means of small and wide-angle X-ray scattering.

The recrystallization process was explained by the fact that any polymer crystallizes in a metastable state far from equilibrium state and such system tries to reach an equilibrium state. Here the term “recrystallization” means a process of post crystallization occurring at the same temperature or with the rise in temperature after partial melting, and the effect of recrystallization is determined by its rate^{41,42}. It was observed^{43,44} that when polymers are crystallized at large supercoolings a subsequent heating is accompanied by the recrystallization processes. *Statton* et al.⁴³ in his studies of polyethylene crystals described the recrystallization process taking place during annealing of the dry crystals as a process of refolding of the chains resulted in increasing lamellar thickness observed as an increase of long period in the SAXS analysis. He observed considerable molecular motion involving the movement of the entire chain.

The recrystallization was found⁴¹ to lead to the appearance of a multiplicity of the melting peaks in the DTA and dynamic calorimetry curves. The first part of recrystallization is melting; the melting range was connected with the existence of crystallites of different thickness. With the rise of temperature, the smallest and more defective crystals (or crystal surfaces) melt and the amorphous phase becomes enriched in raw material, capable to crystallize. *Yagfarov* mentioned that the rate of recrystallization is not constant during the whole heating process but decreases with increasing temperature. He believes that there exists a certain temperature T_c above which a system has no longer time to recrystallize at this heating rate. On the graph, the exothermic peak of recrystallization is superposed to the

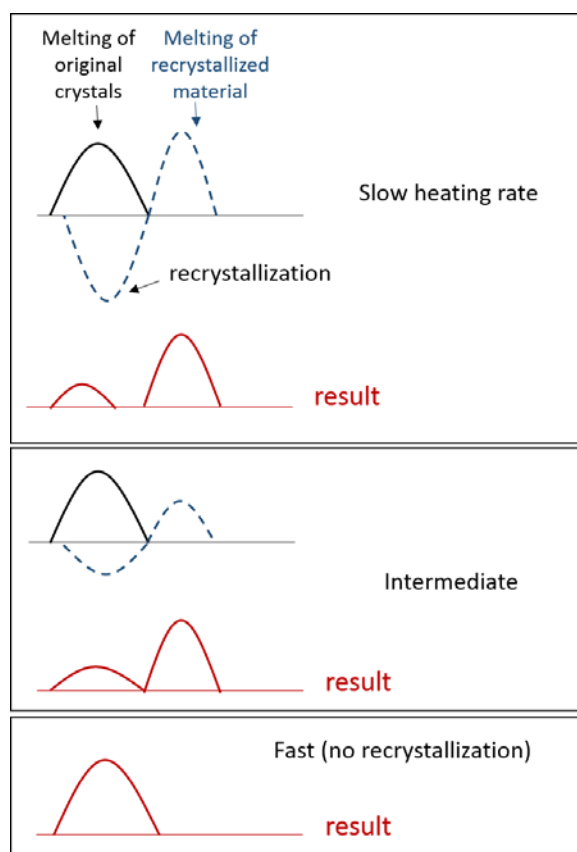


Figure 2.13 Scheme of recrystallization model adapted from^{39,40}

endothermic peak of fusion. As a result of compensation, no effect is observed on the graph. The corresponding scheme of such compensation on the calorimetry curve was proposed by *Rim and Runt*⁴⁰ and then adopted by *Lee and Porter*³⁹ for the case of PEEK (Figure 2.13).

2.2 Thermal analysis of polymers

Thermal analysis is a classical technique of polymer characterization. There is a battery of different methods belonging to the thermal analysis family, including differential thermal analysis (it allows to measure phase transition temperatures, enthalpy changes, specific heat capacity changes), thermo-gravimetry (the mass changes due to decomposition, evaporation, dehydration, etc. can be evaluated), thermomechanical analysis (changes of size of material, deformations, determination of viscoelastic properties, density changes, etc. are assessed), thermo-physical measurements (thermal diffusivity, thermal conductivity, transport properties), adiabatic calorimetry (accurate measurements of heat of reactions, phase transitions, thermal stability, etc.).

One of the most widely used techniques of thermal analysis is Differential Scanning Calorimetry (DSC). DSC measures the difference in heat flow to or from the sample and to or from a reference which is monitored as a function of temperature or time, while the sample is subjected to a temperature program. Depending on whether more or less heat is flowing to the sample the thermal processes are called *exothermic* (heat release to surroundings) and *endothermic* (heat absorption). Examples of endothermic processes are evaporation, melting, sublimation, protein denaturation. Exothermic processes are combustion, oxidation reactions, nuclear fusion in bombs, some of the polymerization reactions, cross-linking processes, and crystallization.

In polymer physics, not only the heat of melting or crystallization but also other more subtle thermal changes as for example glass transitions can be studied by DSC. Information about the degree of crystallinity, polymorphic and eutectic transitions, reaction kinetics, the effect of ageing and many other phenomena connected with a change in enthalpy or heat capacity are also addressable by DSC. DSC analysis has become a standardized tool for industrial analysis and quality control. Different types of products are analyzed by DSC; it is widely used in pharmaceutical, polymer, food, electronic industries and many others due to fast and accurate analysis of the thermal properties of the materials of interest.

2.2.1 DSC instrumentation and formalism

In a DSC device, the sample and reference materials placed in DSC pans are heated or cooled typically with a linear temperature program and deviations of sample temperature from the reference temperature are measured and converted to heat flow.

A heat-flux DSC measuring cell consists of a single furnace containing both the sample and reference. They are heated together according to a temperature program. When both pans containing the sample and reference are heated or cooled the temperature difference between the sample and reference is recorded. When a thermal transition (e.g., first-order phase transition) occurs in the sample the temperature of the sample will not change until the end of the process. However, the temperature of the reference material will continue to change with the same rate as before. The overall differential signal corresponding to the run will be presented as a linear baseline before and after the event and a peak in the range of the transition. With respect to endothermic or exothermic effects, the occurring peak will be pointing downwards or upwards.

It is noteworthy that the two methods, heat-flux DSC and DTA (differential thermal analysis) are similar in the approach and for both of them the measured signal is the temperature difference between the sample and the reference. This value is then converted to a heat-flux difference in mW by means of an appropriate calibration.⁴⁵ Unlike DTA analysis with two not connected pans for the sample and the reference, in the heat-flux DSC the heat flow path between the sample and the reference is provided by a metal “bridge” with a high and well defined thermal conductivity. Such construction minimizes the temperature difference between the sample and the reference material. The heat-flux difference in its turn is proportional to the difference in the extensive heat capacities between the sample and the reference. The area under the peak is correlated to the heat of the transition.

The term “differential scanning calorimeter” was originally applied to instruments with separate furnaces for the reference and sample⁴⁵. Nowadays, such type of DSC devices is called “power-compensation DSC”. In the case of power-compensation DSC the temperatures of the sample and the reference material are controlled independently using the separate furnaces. In the case of power-compensation DSC the signal directly measures heat fluxes. The peak area is then directly proportional to the amount of energy released or consumed during thermal transitions.

The DSC signal consists of the total heat flow rate (dq/dt) and under quasi-equilibrium assumption can be expressed as^{46,47}:

$$\frac{dq}{dt} \approx \frac{dH}{dt} = C_p \frac{dT}{dt} + f(T, t), \quad (\text{Eq. 2.40})$$

where $C_p \frac{dT}{dt}$ is a reversing heat flow component (heat capacity-dependent process) and $f(T, t)$ is a non-reversing heat flow component (time- and temperature-dependent processes). Reversible and non-reversible components can be separated using the modulated DSC technique. In equation ((Eq. 2.40) $\frac{dH}{dt}$ – is the total heat flow, C_p – is the extensive heat capacity, $\frac{dT}{dt}$ – is the heating rate. (Eq. 2.40 reflects the difference in heat capacity between the sample and the reference as the slope of the plot of a heat-flow change as a function of heating rate.

2.2.2 Thermal characteristics of polymers

The heat capacity of a system is the amount of heat needed to increase its temperature by 1 K (SI unit is J/K). The heat capacity of the sample normalized by its mass is called specific heat capacity (at constant pressure - C_p , J/K/kg). The specific heat capacity is a measure for the energy storage capacity of a substance. Heat capacity of a material increases with temperature, in the case of polymers it was also observed that a liquid or rubbery polymer can hold more energy than a solid polymer⁴⁸. From a DSC measurement, specific heat capacity can be obtained by dividing the measured heat flux by the heating rate. If the heat capacity of

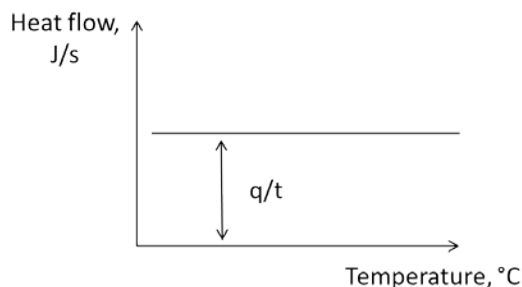


Figure 2.14 Determination of heat capacity from the plot of heat flow as a function of temperature, adapted from⁴⁹

a material is constant over some temperature range, then the plot of heat flow against temperature will be a line with a zero slope⁴⁹ as shown in Figure 2.14.

Thermal properties of polymers can be described by two main characteristics: melting temperature (T_m) and glass transition temperature (T_g). The glass transition temperature, T_g , is the temperature below which the amorphous phase exhibits characteristic glassy-state properties: brittleness, stiffness and rigidity. Above the glass transition temperature polymers acquire a rubbery, flexible form. Such change in mechanical properties is explained by a sufficient amount of energy for the rotations about chemical bonds and of freedom through changes of torsion angles of a polymer backbone. Below the glass transition temperature the only molecular motions that can occur are short-range motions, i.e. secondary relaxations.

The melting temperature, T_m , is the melting temperature of the crystalline phase. This is a first-order transition corresponding to a sharp change of the different properties as density, refractive index, heat capacity, enthalpy, light transmission. Polymers exhibit both T_g corresponding to amorphous regions and crystalline melting temperature (T_m).

2.2.3 Main events on DSC curve

All the thermal characteristics of polymers discussed in the previous section can be evaluated from the DSC measurements. A typical DSC curve of a polymer heating consists of the glass transition step, exothermic (crystallization) and endothermic (melting) peaks as shown in Figure 2.15.

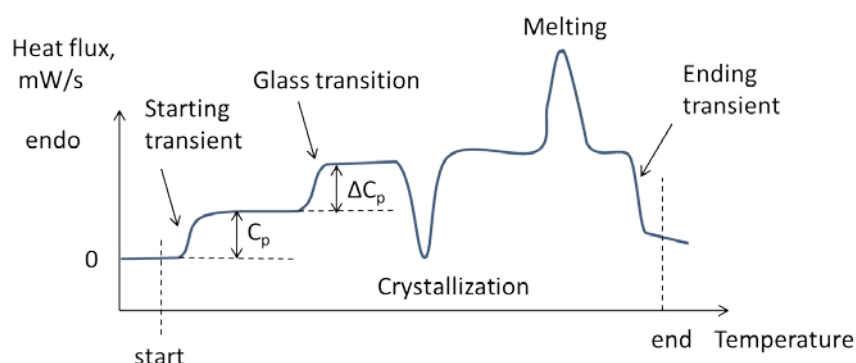


Figure 2.15 Typical DSC curve of a polymer

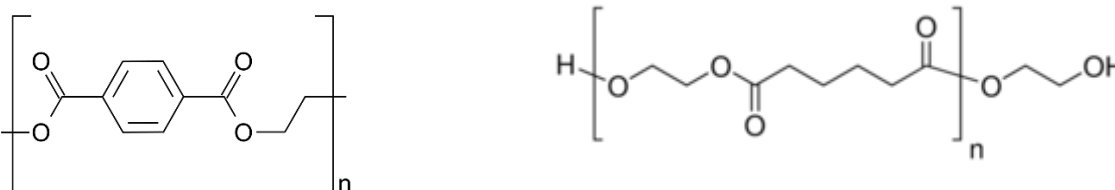
2.2.4 Effect of polymer molecular rigidity on thermal properties

Thermal transitions of typical polymers are given in Table 2.2.

Table 2.2 Melting and a glass transition temperatures of typical polymers⁵⁰

Polymer	T_g , °C	T_m , °C
Poly(ethylene), high-density	-120	135
Polycaprolactone	-60	61
Poly(vinylidene fluoride)	-45	172
Polyoxymethylene	-85	195
Poly(vinyl alcohol)	85	258
Poly(hexamethylene adipamide) (nylon-6,6)	49	265
Poly(ethylene terephthalate)	69	265

The rigidity of polymer chains is increased when there are cyclic structures in the main polymer chains which highly restrict the flexibility of the backbone^{50,51}. Polymers with rigid chains are slow to crystallize because crystallization requires movement of the chains to arrange them in the crystalline phase. For example, poly(ethyleneterephthalate) is more rigid than poly(ethylene adipate) due to the presence of a benzene ring (Figure 2.16) and has a significantly higher value of the glass transition temperature.

Figure 2.16 Polyethyleneterephthalate (left), $T_g = 69$ °C, polyethylene adipate (right), $T_g = -70$ °C

In general, all the phenomena which cause restriction of long-range segmental motion and rigidity of the main chain in polymers result in an increasing glass transition temperature of the material. For example, polar, intermolecular forces, bulky side groups, syndiotacticity cause an increase of the glass transition temperatures. In contrast, an increase in flexibility and branching of the backbone results in a decrease of the glass transition temperature. For example, highly branched poly(vinylacetate) has a T_g of 25.4 °C when the same polymer with only a few branches has $T_g = 32.7$ °C

2.2.5 Limits of DSC

As discussed in Chapter 2.1, semicrystalline polymers have a metastable structure and can, therefore, reorganize to lower their free energy. In this respect, one of the limitations of DSC is that by limiting the heating rate this technique cannot prevent reorganization processes during the thermal experiment. Thermal analysis with sufficiently higher heating rates (such as fast scanning calorimetry) can bypass polymer reorganization and provides an interesting tool for studies of fast thermal transitions.

2.2.6 Nanocalorimetry

Nanocalorimetry is the technique designed to perform thermal analysis of nanograms of materials with nano-Joule sensitivity and sub-mK temperature resolution.⁵²⁻⁵⁴ The released or absorbed heat of thermal transitions of nanogram sized materials is in the range of nW or μ W and cannot be detected by means of classical DSC devices.

Nanocalorimetry is a field of growing interest. A large and rapidly growing number of publications related to this technique has appeared since the 1990s (Figure 2.17). Nanocalorimetry has been applied across a variety of materials studies involving metals, ceramics, polymers, and biological materials⁵⁴.

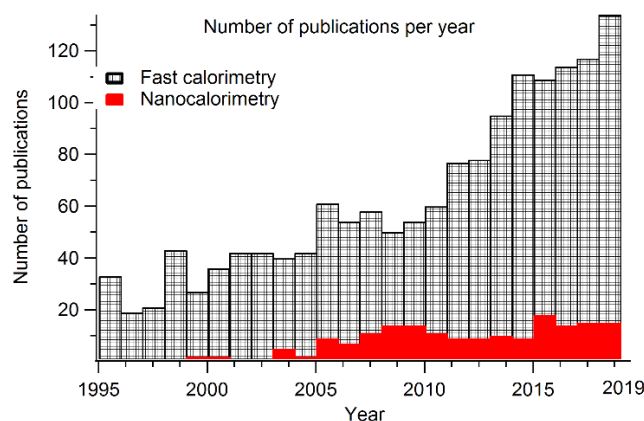


Figure 2.17 Number of publications connected with the terms “nanocalorimetry” and “fast scanning calorimetry” (from “Science Direct” database, state Sep 2019)

Nanocalorimetry has several advantages compared to classical calorimetric devices. Due to the small size of the measuring cell, the device allows reaching heating rates up to 10^6 K/s, which is valuable for analysis of fast processes.

Different types of MEMS-based nanocalorimeters have been recently developed. However, not all technical problems are solved yet. For example, extending the working temperature range would be essential for studies of inorganic materials. For the present moment only Mettler Toledo has a commercialized high-temperature FSC chips (MultiSTAR UFH 1) enabling measurements up to 1000 °C. Further developing of calibration procedures, reference samples, thermal models and software for the devices is also crucial for the field. For example, the temperature calibration at high temperatures (from 573 to 873 K) by optical pyrometry has been suggested⁵⁵ to prevent errors arising in the case of extrapolation of calibrations to higher temperatures.

In polymer science, fast calorimetry has become a unique tool. As was discussed in the previous chapters, semicrystalline polymers form metastable structures. Conventional DSC cannot provide such high heating rates to perform studies of semicrystalline polymers in the conditions where the reorganization process on heating would be bypassed. Extending the range of scanning rates in order to allow investigations of metastable materials is one of the motivations to develop the fast calorimetry technique⁵⁶.

The nanocalorimeter can operate in quasi-adiabatic or non-adiabatic conditions. For the quasi-adiabatic conditions⁵⁷ the heat capacity of a calorimetric cell can be calculated as:

$$P(t) = -\frac{\Delta T}{R_{CG}} = C_p(T)\beta, \quad (\text{Eq. 2.41})$$

where ΔT is a temperature difference between the calorimeter and the surrounded gas, R_{CG} is a thermal resistance between the calorimeter and the gas, $C_p(T)$ is a heat capacity of the calorimetric cell (addenda), β is the scanning rate, $\beta = \frac{dT_c}{dt}$.

In order to reach high heating rates, the heat capacity of the calorimeter itself must be small. To reduce the heat capacity of the calorimeter the measuring cell should be small and light. Therefore, the calorimeter usually consists of a thin silicon nitride membrane with thin-film electronics assembled on it. In order to reach high cooling rates and to be able to study crystallization kinetics of polymers and the amorphization processes on quenching, A. Minakov and co-workers⁵⁸ developed the design of a non-adiabatic fast scanning calorimeter in cooperation with Xensor Integration company. In the developed design of the measuring cell, the active area of the sensor is 50 μm x 100 μm^2 which was small enough to be considered as a point source. The resistive heater provides the heat flux $\Phi_0(t)$, which

increases the temperature of sample, membrane and ambient gas. The heat-flow is proportional to the thermal conductivity of the gas. According to *Minakov et al.*⁵⁸ the heat-balance equation can describe the time dependence of the temperature of the membrane/sample interface in the case of a non-adiabatic calorimeter:

$$(C + C_0) \frac{dT}{dt} = \Phi_0(t) - (T(t) - T_0)G, \quad \text{Eq. 2.42}$$

where C and C_0 are the heat capacities of the sample and addenda. The dependence $C_0(T)$ can be determined from the measurements on the empty cell. The heat capacities of the film heater and film-thermopile can be considered as negligibly small. The main heat capacity of the cell is therefore the effective heat capacity of the heated part of the membrane.

State of art in nanocalorimetry

In 1995 *Allen et al.*⁵⁹ presented the design of the first nanocalorimeter device where resistive heating and simultaneous temperature measurement was performed on a Ni thin film deposited on a 50 nm thick amorphous silicon nitride membrane supported by a Si frame⁵⁷ (Figure 2.18). The sensitivity of this device reached a few J/m^2 and it was possible to heat the sample with the rates up to 10^5 K/s. Such construction of the device allowed measuring several nanometer thick samples at fast heating rates under quasi-adiabatic conditions when the cell is placed in vacuum 10^{-5} - 10^{-6} Pa.^{60,61}

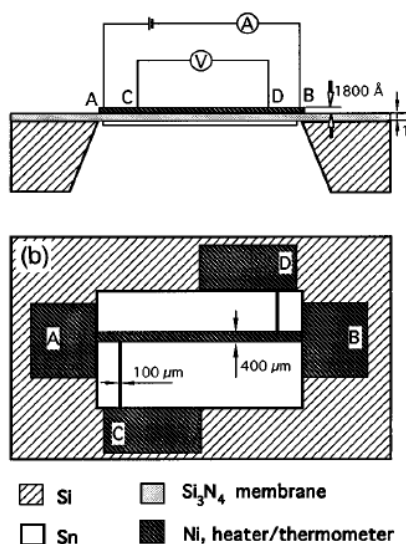


Figure 2.18 Nanocalorimeter designed by *Allen et al.*⁵⁹.

Based on the *Allen et al.* construction, nowadays there is a number of modifications of the device designed to perform nanocalorimetry measurements combined with other in-situ techniques (Figure 2.19 - Figure 2.21) and also to measure liquid samples (Figure 2.22).

In a recent work, *Grapes et al.*,⁶² presented a combination of nanocalorimetry with time-resolved electron microscopy to study the kinetics of an interfacial reaction between Ni and Al at a wide range of heating rates from 1000 to 100000 K/s. The Al/Ni interfacial reaction has been studied extensively using conventional calorimetry, however in the referenced work the authors managed to study the reaction in conditions where the samples were only 100 nm thick and contained just two reacting interfaces. The kinetics of the reaction for the case of fast heating was established by the authors. The schema of the device is shown on Figure 2.19.

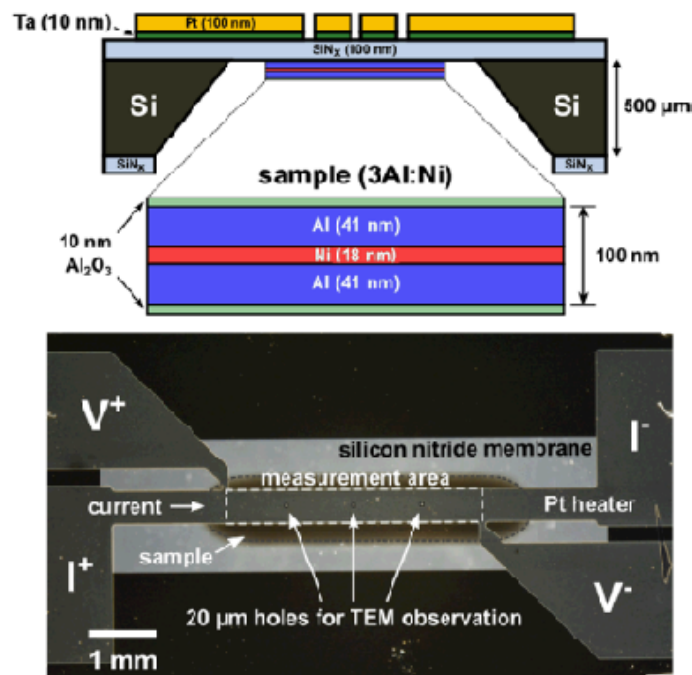


Figure 2.19 Design of a nanocalorimeter for simultaneous TEM analysis developed by *Grapes et al.*⁶²

Yi et al.,⁶³ developed a new nanocalorimeter sensor which was successfully combined with in-situ SEM analysis (Figure 2.20) to perform different types of analysis such as study of melting and solidification of polyethylene oxide, measuring the temperature dependence of the conductivity of a nanowire, the an electron beam induced current measurements (EBIC) of a nanowire in vacuum and air.

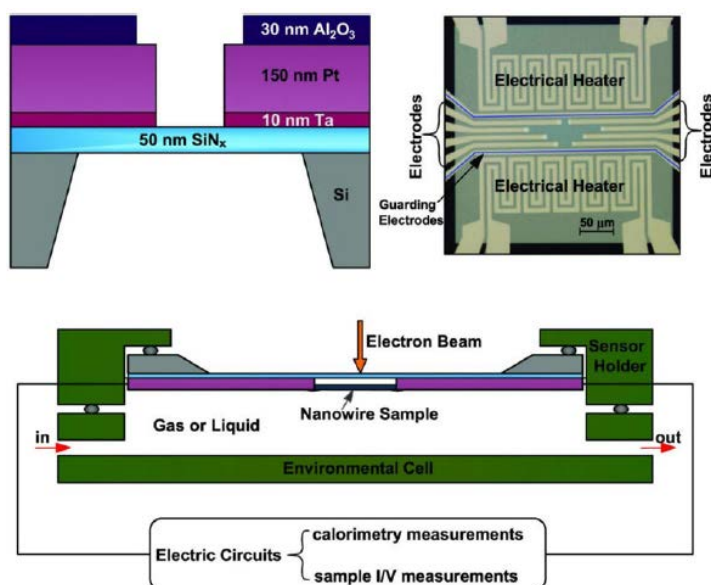


Figure 2.20 Design of the nanocalorimeter for simultaneous SEM analysis developed by Yi et al⁶³

The combination of a nanocalorimeter with time-of-flight mass spectrometer⁶⁴ opened a possibility to perform simultaneous thermal measurements at high heating rates. The nanocalorimeter sensors were inserted into the vacuum chamber of the mass spectrometer (Figure 2.21). Heating was performed at rates of up to 10^5 K/s and mass spectra were recorded simultaneously at 100 μ s intervals. Yi et al.⁶⁴ demonstrated the efficiency of the

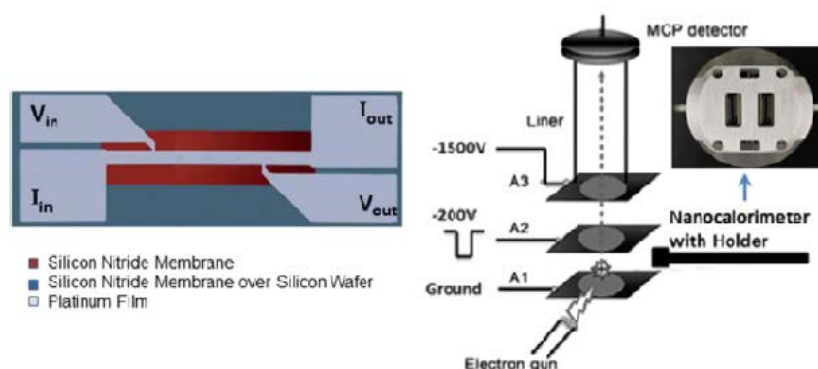


Figure 2.21 Design of the nanocalorimeter for simultaneous mass spectrometry analysis developed by Yi et al⁶⁴

device for three different model systems: organic salt - sodium azotetrazolate, an inorganic compound - ammonium perchlorate, and a metal oxide nanoparticle - copper oxide (CuO). In this work, the heating rate was over 10^5 K/s, where the experiment with copper oxide took 10

milliseconds and a temperature of 1000 °C was reached. This method has a high potential and will allow improving the understanding of energetic reactions.

For the liquid-phase measurements, open and closed-chamber nanocalorimeters are developed. For open-chamber nanocalorimeters deposition systems, working with liquids using syringe pumps, micropipettes or inkjet heads is possible.⁶⁵⁻⁶⁸ Remarkably such open-chamber nanocalorimeters are designed in a way of “enthalpy arrays” where calorimetric sensors are arranged in a plate of about 100 units which became a high-throughput assay tool to detect enthalpies of chemical reactions for biological liquids.

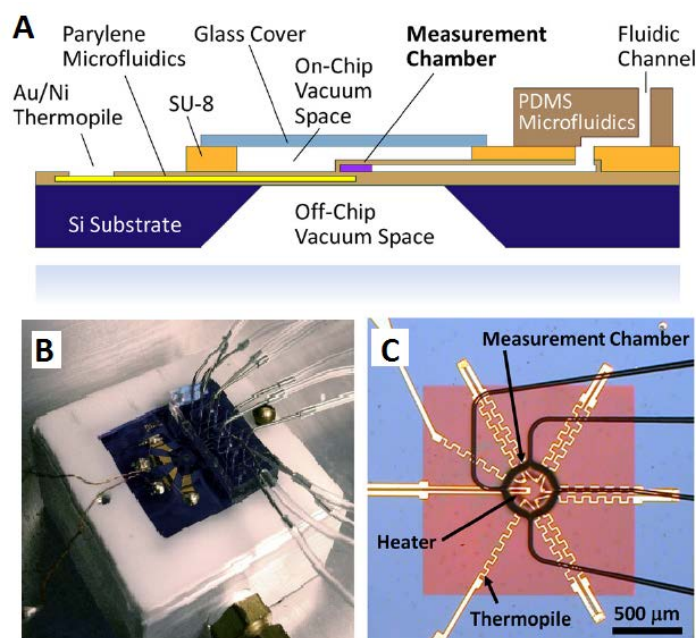


Figure 2.22 Closed-chamber nanocalorimeter for microfluidic measurements by *Lee et al.*⁶⁵

A closed-chamber nanocalorimeter was developed for the microfluidic measurements (Figure 2.22). *Lee et al.*⁶⁵ improved the sensitivity of the device by vacuum encapsulation of the chip providing good thermal isolation. This device was capable of measuring the heat of a reaction of 3.5 nL sample with 4.2 nW resolution. In the experiment, the authors used a model reaction of urea hydrolysis and measured the enthalpy of mixing of water with methanol.

2.2.7 Combination of nanocalorimetry with X-rays

Vlassak and co-authors^{69,70} presented a “parallel nanoscanning calorimeter” which is a micromachined device consisted of a silicon substrate with a 5x5 array of independently controlled calorimeter sensors (the scheme of the device is shown on Figure 2.23).

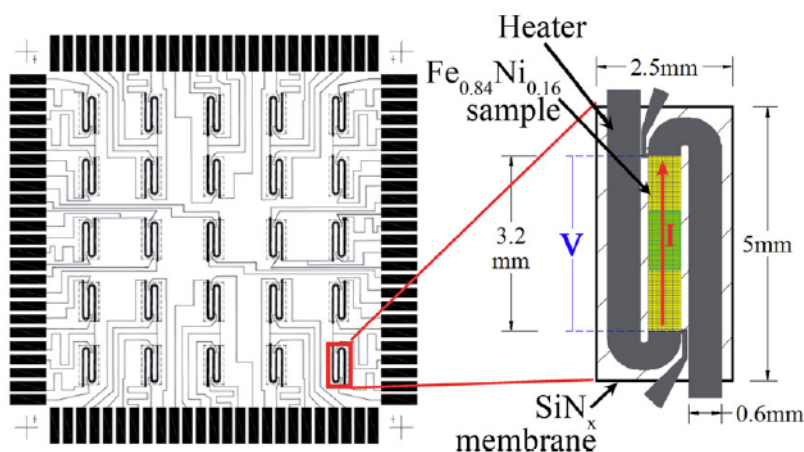


Figure 2.23 Parallel nanoscanning calorimeter by *Vlassak et.al.*^{69,70}

Each sensor contains a tungsten electrical probe that operates both as a heating element and a resistance thermometer and is encapsulated in a silicon nitride membrane. For a simultaneous nanocalorimetry and X-ray diffraction the authors passed a 30 keV synchrotron beam through the vacuum chamber and nanocalorimetry device. The $\text{Fe}_{0.84}\text{Ni}_{0.16}$ thin-film sample exhibiting a martensitic transformation with over 350 K hysteresis was studied using an average heating rate of 85 K/s and cooling rate of 275 K/s. The data acquisition rates provided a nominal temperature resolution of approximately 10 K or better. The heating rates reached 1000 K/s. The X-ray beam had dimensions of 0.6 x 1 mm in cross-section with a flux of $4.5 \cdot 10^{10}$ photons per second at 30 keV. The detector was able to image 30 frames per second, which allowed for lowest acquisition times of 0.2 s.

The most recent research paper combining nanocalorimetry with synchrotron X-ray micro-diffraction was published by K. Willa and co-workers⁷¹ who used a setup for experiments on micrometer-sized single-crystalline samples at low temperatures (4K) in magnetic field.

2.3 X-ray analysis of polymers

The morphology of polymers comprising the size, distribution and orientation of crystallites as well as degree of crystallinity determine their physical and chemical properties. Several techniques are widely used to examine the structure and the morphology of polymers at different length scales: wide and small angle X-ray scattering techniques in all their different variants, as well as electron diffraction and neutron scattering are only a few methods mentioned next to the field of microscopy ranging from electron microscopy, e.g. transmission electron microscopy and scanning electron microscopy, to scanning force microscopy and optical microscopy. However, in the frame of this project mainly wide angle X-ray diffraction (XRD) will be used.

X-ray diffraction analysis of crystalline materials is based on the interaction of an X-ray wave with the electrons orbiting in the electron shells of the atoms comprising the material. In case of the periodic variations of the electron density of a crystal lattice, the interaction will result in constructive and destructive interferences of waves scattered from the atoms. The direction of constructive interference, which leads to the appearance of diffraction peaks in XRD patterns, is determined by Bragg's law. From X-ray diffraction patterns different parameters can be extracted, such as the lattice parameters of crystals, the degree of crystallinity of a material, information about structural disorder and orientation amongst others.

The main components for establishing of an X-ray diffraction experiment are a sample, an X-ray source and an X-ray detector. Laboratory X-ray generators are typically X-ray tubes which convert electrical energy into X-rays. A typical X-ray tube consists of a cathode which emits electrons and an anode which is a target for the electrons sealed inside a vacuum vessel or tube. As a result of the collision of electrons with the target material, usually made from copper, tungsten or molybdenum, the electrons of the electron target are transformed to the excited state. When collapsing back to their ground state an X-ray beam of a characteristic line spectrum for the particular target material is emitted. In addition to the characteristic line spectrum a broad continuous spectrum, i.e. "bremsstrahlung", is emitted as a consequence of the deceleration effect of the electron in the target material. A single characteristic X-ray emission line is monochromatic and can be used for diffraction experiments. Modern X-ray tubes apply the rotating anode technology to use the target material more efficiently and to dissipate heat more efficiently. The application of rotating anode sources allows for higher X-

ray flux and better defined X-ray beams. In order to obtain a micro-focus X-ray laboratory source improvements have been made for electron focusing coupled with confocal optics. Other X-ray sources are also widely used in experimental practice. Examples for this are radioactive isotopes, synchrotrons and free-electron lasers. Since radioactive isotopes produce X-ray radiation together with α - and β -rays these sources are typically limited to medical or military purposes. Synchrotron radiation facilities and free-electron lasers produce much more intense beam with better optical properties compare to X-ray tubes. The use of synchrotron radiation will be discussed in Chapter 2.4 in more detail.

For X-ray diffraction experiments X-rays with wavelengths in the order of the interatomic spacing of crystals are typically used. The typical wavelength range applied in polymer characterization is in the range from 0.7 to 2 Å (17 - 7 keV). Laboratory sources typically employ X-ray tubes emitting Cu K α radiation with $\lambda = 1.5406$ Å.

Wide-angle X-ray diffraction (WAXD) is a method of X-ray diffraction analysis used for resolving sub-nanometer sized structures (inter-planar distances in crystals and atomic positions) while Small-angle X-ray Scattering (SAXS) is used for resolving larger structures, ranging from several nanometers to micrometers, including aggregates of particles, fibrillar and lamellar morphology, crystallite organization in semicrystalline polymers and other.

Wide-angle X-ray scattering (WAXS) is a more general term than Wide-angle X-ray diffraction (WAXD) which refers to the interference of radiation scattered from periodic structures in the sample, however, both of the terms are often used interchangeably. Main focus of the current research was laid on WAXD analysis and all the later discussion will be devoted to this method.

2.3.1 Bragg's law

Bragg's law was formulated after observation of strong reflections appearing as the result of interaction of X-rays with crystalline solids. Bragg explained the observed pattern by the existence of discrete parallel planes in crystals separated with a precise distance, i.e. the d -spacing or simply d .

An X-ray diffraction peak can be observed when the X-ray waves diffracted from neighboring planes will interfere constructively. Mathematically, Bragg's law can be expressed in the following way:

$$n\lambda = 2d \sin \theta \quad (\text{Eq. 2.43})$$

with
$$d = \frac{2\pi}{q}, \quad (\text{Eq. 2.44})$$

where d is the distance between atomic planes (d -spacing), λ is the wavelength and n denotes to an integer value representing the order of the diffraction. When written in this scalar form q denotes to the modulus of the scattering vector of the interference maxima.

Equation ((Eq. 2.43) represents Bragg conditions for the diffraction experiment. Bragg peaks can be observed in the diffraction pattern at the points where the scattering angles satisfy Bragg conditions. Schematically Bragg's law can be represented as shown on Figure 2.24. Two plain waves with the same wavelength and phase approach a crystalline structure. After scattering off two atoms in the neighboring planes waves will be constructively interference if the difference in their path $d \sin(\theta)$ will be equal to an integer multiplied by the wavelength of the radiation.

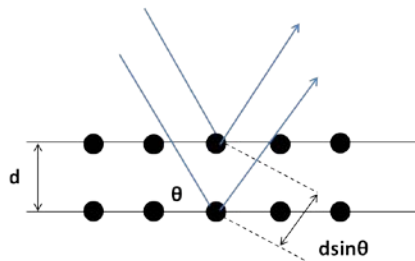


Figure 2.24 Diffraction of two waves from the crystalline structure

The visual representation of the phenomenon of diffraction connecting the wave vectors of the incident and diffracted X-ray beams, the diffraction angle and the reciprocal lattice of the crystal was introduced by Ewald. The geometrical construction is based on the wave vectors k_0 and k_1 , where k_0 is a propagation vector of the incident beam with the length equal to the reciprocal of the wavelength (Figure 2.25):

$$|k_0| = 1/\lambda \quad (\text{Eq. 2.45})$$

Here k_1 corresponds to the scattered vector of the same length. The aim of the Ewald sphere construction is to determine which lattice planes will result in a diffraction signal for a given wavelength of the incident radiation. The term "Bragg condition" simply refers to the fact that diffraction will occur only for reciprocal lattice points that lie on the surface of the Ewald sphere.

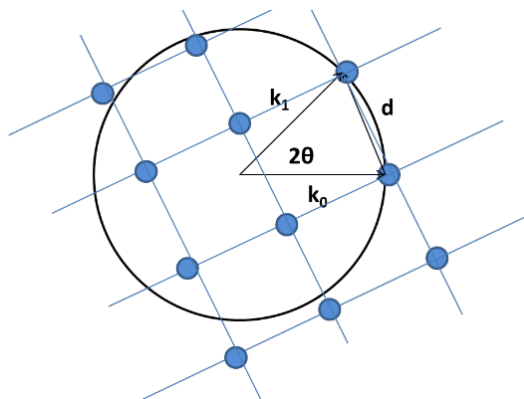


Figure 2.25 Representation of Ewald sphere, where k_0 is a wave vector of the incident beam, k_1 is a wave vector of the diffracted wave, 2θ is the diffraction angle, d is the interlayer distance

Bragg's law is often applied to analyze the diffraction patterns of crystalline materials in order to obtain the interlayer distance d . However, the mathematical relation between the modulus of the reciprocal vector q and distances in real space d can also be used to obtain information about short-range order and the network configuration in the amorphous materials, i.e. in glasses even though no real crystallographic planes are present. This statement can be derived from the Fourier theorem for diffraction where the reciprocal intensity distribution corresponds to the Fourier transform of the auto-correlation function of electron density distribution.

2.3.2 X-ray powder diffraction

When recording X-ray diffraction patterns of single crystals not all the crystalline planes may be oriented to fulfil the Bragg conditions at any moment. In order to collect the diffraction peaks of all possible crystalline planes, accessible at a given energy, the sample has to be rotated around at least 2 axis in case a two dimensional detector is applied.

Another solution to this problem is to use powder samples. Powder samples consist of a lot of small crystallites (or grains) with coherently scattering domains usually from sub micrometer

to several micrometers with all crystallite orientations homogeneously distributed. The particle geometry of a powder can influence the degree of preferred orientation. In order to provide accurate measurements the grain size should be smaller than $10\ \mu\text{m}$.⁷² In case of polymers this conditions are typically matched since polymers consist of small crystallites arranged in the bulk sample usually with a broad and smooth distribution of their orientation. Thus, for practical purposes, X-ray diffraction of bulk polymer samples can be considered as the equivalent to powder diffraction. However, one particular restriction to this statement should be added regarding this study. In the case where sub-micron sized beams are used to study thin polymer samples or films, the polymer can often show texture effects caused by crystal superstructures, e.g. fibrils, spherulites and dendrites, etc.

To be able to collect a valid X-ray powder diffraction pattern a statistically significant number of crystallites has to fulfill the Bragg condition. In this case, cones of diffracted rays for different planes appear as concentric rings, known as Debye-Scherrer rings, on the flat surface of a two-dimensional area detector positioned at normal incidence to the primary X-ray beam as shown at Figure 2.26.

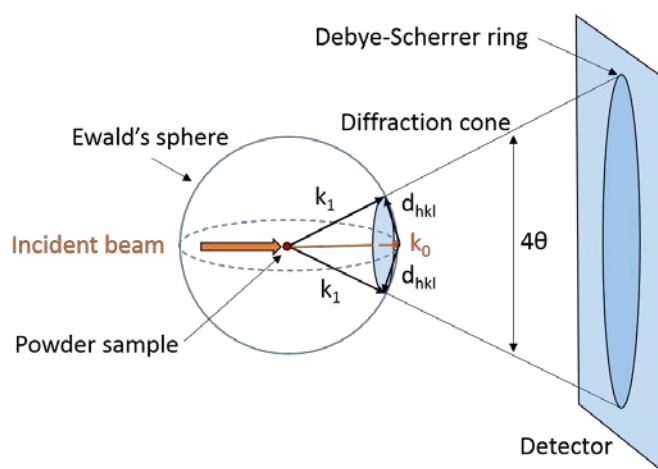


Figure 2.26 Scheme of powder X-ray diffraction, adapted from ⁷³, k_0 is a wavevector of the incident beam, k_1 is a wavevector of the diffracted wave, d_{hkl} is the interlayer distance

In X-ray diffraction experiments the diffracted intensities are recorded as a function of the modulus of the scattering vector q , which is related to the scattering angle 2θ . X-ray detectors can be 0D (point detectors), 1D or 2D. By azimuthal integration of 2D powder diffraction patterns a 1D pattern can be obtained and then analyzed. The positions of the crystallographic reflections can be directly obtained by applying Bragg's law, while the intensity of the

crystallographic reflections is calculated by integrating the diffraction profiles in both directions, azimuthally and radially.

2.3.3 Structural parameters from X-ray powder diffraction pattern

The information that can be extracted from X-ray diffraction patterns is mostly contained in position, intensity and shape of crystalline reflections and the shape and position of the amorphous halo which is usually present in the case of semicrystalline materials. These parameters encode information related to the crystal structure, crystallographic defects and intrinsic strain in the lattice, degree of crystallinity, size of crystalline domains and many more. A collection of the most important structural features and the corresponding structural parameters that can be derived from X-ray diffraction are presented in the Table 2.3, as summarized from.⁷³⁻⁷⁵

Table 2.3 Structural parameters accessible by WAXD analysis as summarized from⁷³⁻⁷⁵

Structural feature	Characteristic parameter	Feature in the WAXS pattern
Crystal structure	Unit cell dimensions, translational symmetry	Positions of the crystalline reflections
	Atomic positions	Positions and the intensities of crystalline reflections
Crystallites	Total weight fraction of the crystalline domains	Area under the crystalline reflection peak relative to the scattered intensity
	Size, defects, inhomogeneous composition, instrumental function	Width of the Bragg peaks
	Disorder, strain	Increase in the width of the peak with scattering angle, shape of peak
	Orientation, aggregate structure	Azimuthal spread of the intensity in the crystalline reflections
Polymorphs, composition	Relative fractions	Relative intensities of the corresponding reflections
Amorphous domains	Inter-chain distance	Positions of the amorphous halo
	Orientation	Azimuthal spread of the amorphous halo
	Oriented or intermediate phase	Ratio of the areas due to the oriented and unoriented components

Peak position width and intensity and shape

When analyzing crystallographic reflections from reduced one dimensional diffraction curves in more detail the necessity of using analytical functions to describe the Bragg peaks becomes obvious. However, before introducing the most suitable analytical functions for this purpose some general considerations should be made on the contributions contained in a diffraction peak.

In general, the observed diffraction peak shape (so-called peak shape function, PSF) is a convolution of three different contributions⁷³: the instrument function Ω , describing the shape of the beam, the wavelength dispersion function Λ and the sample function Ψ . The PSF can be generalized essentially:

$$PSF(\theta) = \Omega(\theta) \otimes \Lambda(\theta) \otimes \Psi(\theta) + b(\theta), \quad (\text{Eq. 2.46})$$

where $b(\theta)$ corresponds to the background function.

The instrument function Ω , depends on geometrical parameters such as the location and geometry of the X-ray source, divergence of the beam, slits settings, point spread function of the detector, etc. The wavelength dispersion function Λ accounts for the distribution in wavelength (or photon energy) of the incoming beam and varies depending on the nature of the used X-ray source. The specimen function Ψ originates from dynamic scattering and from the physical properties of the sample, e.g. crystallite or grain size and their distribution, crystallographic defects and macrostrains present in the crystals, etc.

The two simplest peak shape functions typically used to approximate experimentally measured Bragg diffraction peaks are the Gaussian and Lorentzian distribution functions. The analytical formalisms for both distribution functions are given below.

Gauss:

$$y(x) = G(x) = \frac{C_G^{1/2}}{\sqrt{\pi}H} \exp(-C_G x^2) \quad (\text{Eq. 2.47})$$

Lorentz:

$$y(x) = L(x) = \frac{C_L^{1/2}}{\pi H'} (1 + C_L x^2)^{-1} \quad (\text{Eq. 2.48})$$

The shape of the Gaussian and Lorentzian distribution function, normalized to the maximum amplitude, are represented in Figure 2.27 to appreciate the difference close to the base of the peak. According to *Langford*⁷⁶ diffraction peaks are better described using the Lorentzian function when a monochromatic X-ray source is used and the instrument function is negligible, while the Gaussian distribution is better suited when the profile has contributions from lattice strain. However, in the case when X-ray focusing optics are used, or when the primary beam is large compared to the pixel size of the used detector the shapes of real diffraction peaks can rarely be described accurately by solely Gaussian or Lorentzian distributions.

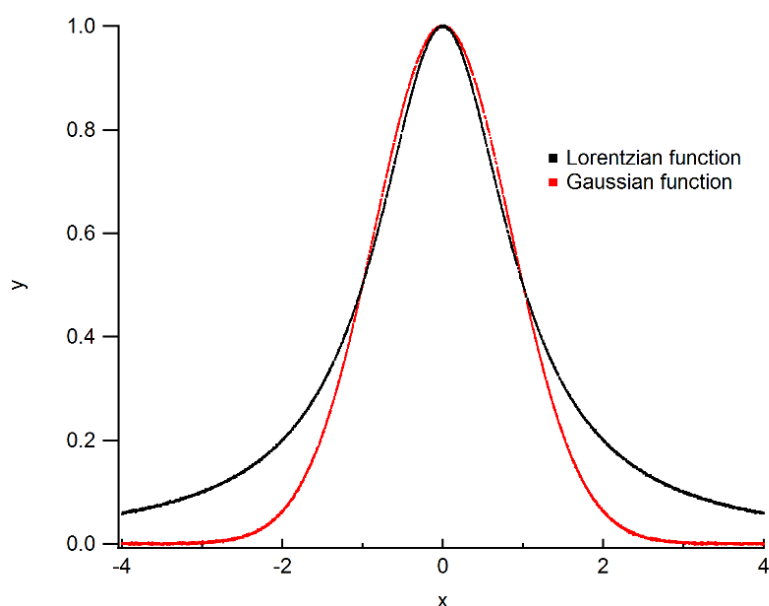


Figure 2.27 Gaussian and Lorentzian distributions normalized to the maximum

Usually real peak shapes are located somewhere between the Gaussian and Lorentzian distribution and they can be better represented as the combination of the two functions. The function obtained as the result of the convolution of Gaussian and Lorentzian functions is known as Voigt function. Indeed, the Voigt function is commonly applied to analyze diffraction or spectroscopy data. However, when refining a diffraction pattern with a multitude of diffraction peaks a linear combination of the Gaussian and Lorentzian distribution to approximate the Voigt profile is easier to handle numerically and still sufficiently accurate in its approximation of the diffraction peaks. The Gaussian and Lorentzian are mixed in η to $1-\eta$ ratio, so that the value of the mixing parameter, η , varies

from 0 (pure Lorentz) to 1 (pure Gauss). This linear combination is usually called pseudo-Voigt function.

Pseudo-Voigt:

$$y(x) = PV(x) = \eta \frac{C_G^{1/2}}{\sqrt{\pi}H} \exp(-C_G x^2) + (1 - \eta) \frac{C_L^{1/2}}{\pi H'} (1 + C_L x^2)^{-1} \quad (\text{Eq. 2.49})$$

Where H and H' are the full widths at half maximum (FWHM),

$$C_G = 4 \ln 2 \quad \text{with} \quad \frac{C_G^{1/2}}{\sqrt{\pi}H} \quad (\text{Eq. 2.50})$$

is the normalization factor for the Gauss function so that

$$\int_{-\infty}^{\infty} G(x) dx = 1 \quad (\text{Eq. 2.51})$$

and

$$C_L = 4 \quad \text{with} \quad \frac{C_L^{1/2}}{\sqrt{\pi}H'} \quad (\text{Eq. 2.52})$$

is the normalization factor for the Lorentz function such that

$$\int_{-\infty}^{\infty} L(x) dx = 1 \quad (\text{Eq. 2.53})$$

An alternative peak shape function sometimes used in the literature is the Pearson-VII distribution function.

Pearson-VII:

$$y(x) = PVII(x) = \frac{\Gamma(\beta)}{\Gamma(\beta - 1/2)} \frac{C_p^{1/2}}{\sqrt{\pi}H} (1 + C_p x^2)^{-\beta} \quad (\text{Eq. 2.54})$$

where Γ is the gamma function,

$$C_p = 4(2^{1/\beta} - 1) \quad (\text{Eq. 2.55})$$

and

$$[\Gamma(\beta)/\Gamma(\beta - \frac{1}{2})]C_p^{1/2} / \sqrt{\pi}H \quad (\text{Eq. 2.56})$$

are the normalization factors for the Pearson function so that

$$\int_{-\infty}^{\infty} PVII(x)dx = 1 \quad (\text{Eq. 2.57})$$

Pearson-VII provides an intensity distribution close to the pseudo-Voigt function: when the exponent $\beta=1$, it is identical to the Lorentz distribution, and when the exponent is close to 10, Pearson-VII becomes nearly pure Gaussian. Both the pseudo-Voigt and Pearson-VII functions are centrosymmetric.

2.3.4 Scherrer equation

While the positions of the diffraction peaks reflect the lattice parameters, the width of the diffraction peaks contains information about crystallite size and the possible presence of crystalline defects^{74,77}. The Scherrer formula gives an approximation for the size of coherently scattering domains, L , which, in the simplest case, reflect the size of the crystallites. In 2θ notation the Scherrer formula can be written as:

$$L = \frac{K\lambda}{\beta_0 \cos \theta}, \quad (\text{Eq. 2.58})$$

where K is a shape factor, which is typically equal 1, λ is the wavelength of the used radiation, β_0 is the line broadening at half maximum intensity in radians, while θ is the Bragg reflection angle.

Besides the crystallite size the crystalline disorder also contributes to the peak broadening. In the case of polymeric materials, linkages between polymer chains in the amorphous and crystalline phases intrinsically increase the structural disorder^{74,78}, and thus are leading to much broader crystallographic reflection as compared to e.g. metals or protein single crystals. Therefore crystalline disorder and crystallite shape have to be considered when concluding on the actual sizes of the crystallites.⁷⁷

Two kinds of crystalline disorder can be identified from X-ray diffraction patterns: whether they leave the long-range order unchanged or not. The former are caused by thermal vibrations and static defects that alter the position of the atoms locally around the lattice points (vacancies, interstitials, displacements, substitutions). Such kind of disorder decreases the intensity of Bragg peaks without changing their width and contributes to diffuse scattering under the Bragg peak. The second kind of disorders cause broadening of the crystalline peaks with growing q .

2.3.5 Crystallinity in polymers from 1D powder diffraction curves

Polymers can contain a big variety of different structures from almost defect-free crystalline lamellae to partially or highly disordered structures: crystals with dislocations and other defects, 1D and 2D ordered aggregates and resin-like fully amorphous domains.⁷⁴ Usually, the diffraction patterns are modeled as the incoherent sum of contributions from disordered and crystalline parts. For the subsequent analysis it is wise to separate the scattering pattern into a sum of narrow *Bragg* reflections attributed to crystalline phase and a broad halo arising from the diffuse scattering of the amorphous phase.

Assuming a polymer as a two-phase system containing a crystalline and an amorphous phase. Then the total crystallinity can be calculated as a ratio between the area under the crystalline peaks and the total scattered intensity⁷⁹. The scattered intensity under the crystalline peaks can be expressed as a volume integral of the diffracted peaks^{74,80}:

$$V_c \sim \int_0^{\infty} I_c(q) dV_Q = \int_0^{\infty} q^2 I_c(q) dq \quad (\text{Eq. 2.59})$$

The weight fraction of crystallinity φ_c is then:

$$\varphi_c = \frac{\int_0^{\infty} q^2 I_c(q) dq}{\int_0^{\infty} q^2 [I(q) - I_{\text{compt}}(q)] dq}, \quad (\text{Eq. 2.60})$$

where $I_c(q)$ corresponds to the scattered intensity under the crystalline reflections along the scattering vector q , $I(q)$ is the overall scattering intensity. I_{compt} is an intensity of incoherent (Compton) scattering along the scattering vector q making an additional contribution to the diffuse background.

Lorentz correction

Care has to be taken, that when working with experimental diffraction data the scattering intensities integrated from the diffraction pattern are properly weighted, after integration to one dimensional scattering curves, in order to account for the decreasing scattering intensity with increasing q . The so called Lorentz correction accounts for the fact that the scattering intensity at a certain q -value is distributed over a sphere in the reciprocal space with the diameter q , called sometimes the *Polanyi* sphere. The surface of this sphere, where the scattered intensity is distributed over, increases with the square of the radius resulting in an apparent reduction of the scattering signal per square unit of the spheres surface.

When using a point detector, as it was done typically in the past, the "area" of the point detector stays constant with the scanning angle while the surface of the Polanyi sphere the background corrected scattering signal needs to be multiplied by the square of the Polanyi sphere radius q . This also applies when it comes to the use of 2D detectors where the integrated scattering intensity is normalized by the length of the ring segment along which the intensity was integrated.

Alternatively, the crystallinity index (X_c) can be approximated through the areas of amorphous (A_a) and the crystalline (A_c) phases without applying a Lorentz correction. However, the comparability of the crystalline index is somehow reduced to qualitative comparison within on set of experiments. The crystallinity index can be written as:

$$X_c = 100 \times \frac{A_c}{A_a + A_c} \quad (\text{Eq. 2.61})$$

For an accurate calculation of crystallinity several important steps should be made before the calculation⁷⁸:

The amorphous halo

The amorphous halo represents the distribution of intra- and inter-molecular distances present in the amorphous phase. The peak position of the amorphous halo corresponds to an average of the distance of closest approach of the scattering entities⁸¹. One approach for the estimation of the parameters of an amorphous halo for semicrystalline polymers is to make an X-ray diffraction measurement of a fully amorphous (quenched) sample⁷⁸. Then, upper limits

for the width of the amorphous halo and lower limits for their positions in q can be extracted from the X-ray diffraction pattern of the amorphous sample and applied to the XRD pattern of the semicrystalline material. However, for some groups of materials, e.g. the semi-rigid chain polymers, the amorphous phase in the fully quenched sample does not contain constraint molecule entities, while the inter-lamellar amorphous phase of those materials does. This can reflect in a slight change of position and shape of the halo.

In principle there is no general distribution function that can model different amorphous halos for all different materials. The shape of an amorphous halo is determined by the composition, orientation and configuration of the molecules in the particular polymer and can be both almost symmetric (as in the case of polyethylene) and asymmetric as a function of q . In the current work the shape of the amorphous halo was described by two Pearson-VII functions connected in their maximum points to account for the asymmetrical shape of the amorphous halo in PEEK.

Background subtraction

Scattering background is caused by scattering of the direct beam from air, the sample holder, X-ray windows, and other components of the setup. In order to estimate and subtract the scattering background normalization of the beam upstream and downstream the sample should be performed regarding the absorption of the sample. In the general case the background can be estimated by carrying out an empty cell measurement which can be subtracted from the raw signal. In the current work at ID13 various precautions were taken to reduce the background scattering level as much as possible. Therefore, a flight-tube filled with helium was placed about two millimeters downstream the sample to reduce the air path and consequently reduce the air scattering. In addition a collimation scheme with three pinhole apertures was used where the last pinhole was less than three millimeter upstream the sample position to reduce the free path of air scattering further. The collimation scheme used will be discussed in Section 4.2.2.

In addition the MEMS based calorimetry chip with thin amorphous SiN membrane was used as sample support for the experiments combining nanocalorimetry with X-ray micro-diffraction. Such membrane material has an extremely low scattering background. As it comes to absorption of the primary beam one has to state that the polymeric samples

investigated for this study do not contain any heavy elements and are only 20 μm in thickness. Therefore the absorption can be neglected in the considered cases.

2.4 Synchrotron radiation

Synchrotron and X-ray Free Electron Laser radiation facilities are the most powerful artificial sources of X-rays currently available. In a synchrotron storage ring beams of accelerated electrons, or in some exceptions positrons, are moving on a nearly circular or polygonal orbit, controlled by magnetic fields, at relativistic velocities⁷³. Synchrotron radiation with wavelengths ranging from the radiofrequency to the high energy X-ray region is emitted in the direction tangential to the electron/positron orbit. The main advantages of synchrotron radiation compared to laboratory sources are: high intensity, collimation, coherence of the beam and a continuous wavelength spectrum and, thus, tunable X-ray energy. The brilliance of X-ray beams (usually measured in photons per second per solid angle per cross-sectional beam area per fractional bandwidth) of third-generation synchrotron sources is up to 12 orders of magnitude higher compared to typical fixed-target X-ray tubes^{73,75} used as laboratory sources.

X-ray optics at synchrotrons provides beams with high flux and high brilliance. With the introduction of synchrotron radiation sources, new types of experiments became possible, i.e. fast time-resolved measurements or X-ray diffraction analysis of poorly scattering materials such as polymers and biomaterials. Synchrotron sources provide better angular resolution for XRD patterns and most of the time a better signal-to-noise ratio when compared to laboratory sources.

Time-resolved micro-diffraction experiments on polymers, conducted for the reported project, demand high X-ray beam flux, sensitive and fast detector operating with a time resolution in the range of milliseconds. In addition, a special optic scheme to minimize the scattering background is required. The ID13 beamline of European Synchrotron Radiation Facility (ESRF) in Grenoble meets all the requirements for such experiments. At this moment, the setup combining fast scanning calorimetry in-situ with X-ray micro-diffraction implemented at the beamline is unique giving the opportunity to study fast structural transitions and complex melting behaviors of polymeric and other organic materials.

2.4.1 ESRF storage ring

The ESRF synchrotron consists of three main elements: the linear accelerator (linac), the booster synchrotron and the storage ring. The linac is a straight section of vacuum tubes where electrons, produced by an electron gun, are accelerated up to 200 MeV before getting injected into the booster synchrotron. In the booster synchrotron electrons are further accelerated to a final energy of 6 GeV before being injected into the storage ring. In the storage ring the electrons orbit in ultra-high vacuum conditions. The storage ring itself consists of alternating straight and curved sections and has an average circumference of about 850 m. The curved sections of the storage ring contain bending magnets, forcing the electron beam on its curved trajectory, while in the straight section focusing magnets (multipoles) and radio frequency cavities are placed in alternation with undulators also termed as insertion devices (Figure 2.28). The radio-frequency (RF) cavities are installed in the ring in order to recover the energy loss of the electrons while passing along the orbit.

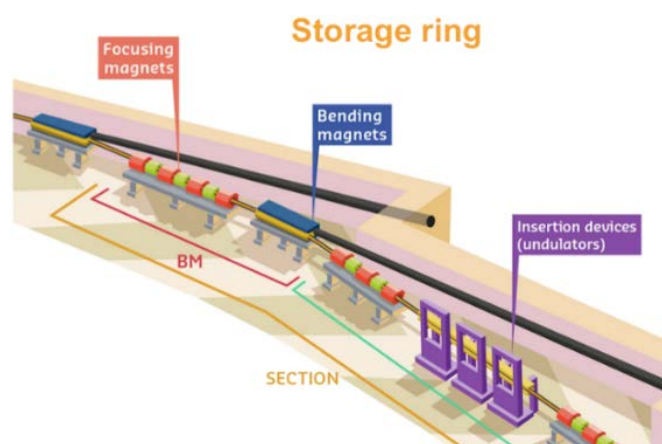


Figure 2.28 Scheme of storage ring, reprinted from⁸² showing BM and ID types of beamlines. BM-beamlines use the radiation produced by Bending Magnets while X-ray radiation for ID-beamlines is produced by undulators

X-ray sources at the ESRF

Two types of sources are used in the ESRF to produce X-ray radiation: bending magnets and undulators. As discussed above the main purpose of the bending magnets is the deflection of the electron orbit. However, as a result of deflection from the straight pass electrons emit a spray of X-rays tangentially to the plane of the electron beam. The spectrum obtained from a bending magnet is wide and continuous, covering the whole range from microwaves to hard X-rays. However, the brilliance is much lower than the brilliance of the beam obtained from

an undulator. In the undulator electrons pass through an alternating periodic magnet structure, which forces them to oscillate and to emit a highly brilliant spectrum, narrowly distributed in wavelength as the resulting interference pattern. Typically undulators are tunable by adjusting the gap through which the electrons are passing, thus, allowing an adjustment of the X-ray beam energy. Each of beamlines consists of optical and experimental hutches, being heavily shielded, and control cabins. Though the undulator is a part of the beamline it is placed in the storage ring upstream the optics hutch. In the optical hutch beam parameters such as energy, and primary beam size can be adjusted.

2.4.2 ID13 generic description

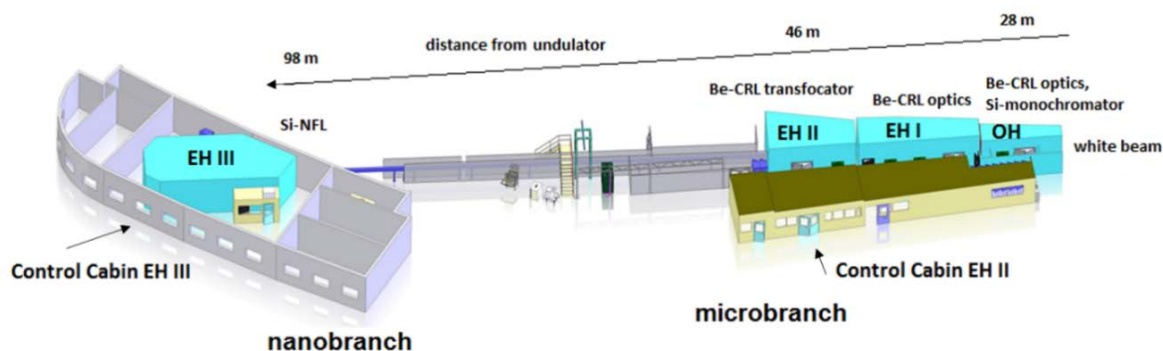


Figure 2.29 Schema of the ID13 beamline at the ESRF showing the sequence of experimental chambers starting on the right with the optics hutch at 28 m downstream from the source followed by the experimental hutches I, II, and III at 35, 46 and 98 m from the source respectively.

ID13, also called “The Microfocus Beamline”, is open for the users since September 1994. The beamline consists of two endstations: a microbranch and a nanobranch operating in time-sharing mode (Figure 2.29). The beamline is dedicated to micro- and nanobeam diffraction and scattering experiments with high-spatial-resolution. Scientific topics at ID13 are highly diverse. However, the beamline is specialized to tune the experimental environment for soft condensed matter research including the analysis of bio-materials and polymers. Offering a variety of sample environments and wide possibilities to use different in-situ setups along with the high brilliance and small beam size makes this beamline unique but also flexible for a wide range of applications.

X-ray source at ID13

The primary X-ray source of ID13 is an 18 mm period in-vacuum undulator optimized for 12.5 keV energy with a minimal gap of 6 mm. The available energy range for the U18 is comparably narrow: 12.5-20 keV. A second fully-tunable in-air undulator with 35 mm period can be operated within an energy range from 5 to more than 25 keV however at lower brilliance.

Optics Hutch (OH)

The first optical system downstream the frontend of the beamline are the primary high power slits allowing selecting a subsection of the undulator beam to partially adjust the beam intensity and source size. Further along the X-ray beam path a set of parabolic compound refractive Be-lenses with 200 μm radius of curvature in the apex can be introduced in the beam path serving as condenser optics by collecting photons and focusing them onto the micro and nano-focusing optics. Downstream these lenses, a liquid N_2 -cooled Si(111) channel-cut monochromator is used to select the desired beam energy with an energy band pass $\Delta E/E$ of 10^{-4} , respectively.

Microbranch (EH2)

Scanning micro-beam experiments are performed in the micro-hutch (EH2) of the beamline. The X-ray micro beam in EH2 is focused by a second set of parabolic beryllium-based compound refractive lenses (CRL-lenses) with 50 μm radius of curvature in the apex. Since the beamline operates in time sharing mode with alternating micro- and nano-diffraction experiments the Be-lenses are arranged in a "transfocator", a vacuum vessel with actuators, allowing removing the Be-compound lenses from the flight path of the X-rays situated at 44 m downstream the source. The transfocator contains 3 compartments filled with 8, 16 and 32 lenses that can be freely combined to adjust the focal distance of the optics and thus the achievable beam size and beam divergence. A typical beam size used in scanning experiments is in a range of 1.5 x 3 microns but can be enlarged using the defocus in special cases when larger beam sizes are needed. For the in-situ experiments reported in this manuscript a beam size of up to 14 μm was used. The photon flux is more than 100 times higher when compared to the nano-focusing lenses at EH3 and is about 2.7×10^{12} ph/s in a $1.5 \times 3 \mu\text{m}^2$ focal spot @ 13 keV in a full current mode.

Nanobranch (EH3)

Scanning nano-beam experiments are performed in the nano-hutch (EH3) of ID13 beamline situated 98 m downstream the source. The main difference of the nano hutch is that it is optimized for high stability in terms of temperature and vibration to allow high resolution measurements. Three different types of optics devices can be utilized in a nano-focus hutch: Si-based compound refractive lenses (nano-focusing lenses, NFL) used for most of the nano-focusing experiments due to their good long term stability and performance; Fresnel zone plate optics which are used for experiments requiring low X-ray energies or large-working distance and multilayer-Laue-lenses with high efficiency and small focal spot size down to sub 40 nm. The typical beam size for the experiments in EH3 is in a range of 80-200 nm. The small beam size is obtained at the expense of primary beam intensity delivering a typical flux of 1.5×10^{10} ph/s @ 15 keV.

XRD Detectors

The Microfocus Beamline ID13 is equipped with a hybrid photon counting pixel array detector Eiger X 4M (Dectris Ltd)⁸³. Hybrid-Photon-Counting technology means direct conversion of X-ray photons into an electrical charge which is detected and processed. In every sensor pixel component of the detector X-ray photons are absorbed, then electron-hole pairs are generated resulting in a charge proportional to the X-ray energy. As a discriminating detector, it generates a digital pulse signal only if the charge pulse exceeds a certain energy threshold. This leads to the absence of dark current effects or readout noise i.e. zero photons result in zero counts resulting in a very high sensitivity. The relatively small pixel size in case of the Eiger detector of $75 \times 75 \mu\text{m}^2$ (which is roughly equivalent to the width of the point spread function) is providing a relatively high spatial resolution.

The beamline is also equipped with a Frelon26A integrating detector, two X-ray fluorescence detectors (Vortex-EM silicon drift X-ray detectors) and two photon counting Maxipix detectors. However, the latter are not used within the frame of the reported project and therefore not explained in more detail.

For the present research it was extremely important to use sensitive, fast detector with high frame rate in order to perform fast time-resolved measurements. In burst mode, The Eiger 4M was able to operate at 750 kHz frame rate (1.34 ms/frame) with 10 μs dead time. The detector is placed downstream the sample on the motorized detector support and can be positioned in

three dimensions, vertically, laterally, and longitudinally in order to select the desired scattering range for the particular experiment.

Raster scanning at ID13

Raster-scanning is a non-continuous form of scan operated with a scanning stage (Micos, Germany) at the microbranch. The translation stages can move the sample in three directions (x, y, z) with a minimum step size of 100 nm vertically, and 500 nm laterally. The translation stage stops at each point and X-ray diffraction pattern collected. With this type of scanning mesh-scans with high resolution are possible.

2.4.3 BM26 beamline

Slow heating measurements of PEEK were performed at BM26, ESRF. BM26 is mostly devoted to soft condensed matter research. The X-Ray source of BM26 is a bending magnet, the photon energy of the X-ray beam used in our experiments was 12.4 keV. The set up allowed simultaneous measurements of WAXS with a Pilatus 300k-W detector and SAXS with Pilatus 1M detector. Time resolution at BM26 can be reduced to a few msec/frame, however, in order to collect reasonable scattering intensity, the duration of one frame had to be increased in the case of PEEK to several seconds. The usual beam size of several millimeters can be tuned down to a spot with dimensions of about 300 x 300 μm^2 . The beamline is equipped with a Linkam DSC hot stage operating within the temperature range from -195°C to 600°C with the scanning rates up to 100 K/min which is suitable for slow heating measurements of sample in-situ with SAXS/WAXS analysis.

3 Polyetheretherketone state of art and open questions

This chapter gives a short review of the current state of research in the field of the main object studied in this project, polyetheretherketone (PEEK). In particular, we review physical parameters, the crystalline structure and thermal behavior. The main models proposed in the literature for the explanation of the double-melting phenomenon will be discussed including recent studies employing fast scanning calorimetry.

3.1 PEEK a high-performance polymer

PEEK belongs to a large family of high-performance thermoplastic polymers called polyetherketones (PEKs), consisting of an aromatic backbone comprising ketone and ether groups in the chemical structure.

The high performance of PEEK explains its typical applications in industry: stability at high temperatures (the operational temperature of PEEK is up to 200 °C), high chemical resistance (PEEK is insoluble in most organic solvents and completely soluble at room temperature only in concentrated sulfuric acid and in a trifluoro-methanesulfonic (triflic) acid⁸⁴); PEEK also possesses very good mechanical properties, which can be comparable to the mechanical properties of metals. The PEEK molecule is relatively stiff because of the presence of the benzene rings along the main chain which also contributes to its high thermal stability.

Another significant property of polyaryletherketone polymers is their biocompatibility. PEKs are extensively employed as bio-compatible materials for orthopedic, trauma and spinal implants. PEEK became one of the leading high-performance thermoplastic candidate for replacing metal implant components in the late 1990s.⁸⁵

3.2 Physical parameters and crystalline structure

The PEEK repeat unit consists of an aromatic backbone with ketone and ether groups (Figure 3.1) where the chain unit adopts planar zig-zag conformation with the bond angle of 125°⁸⁶.

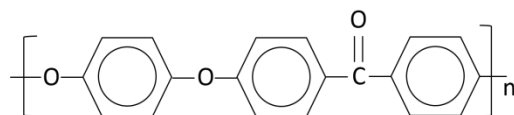


Figure 3.1 Repeat unit of PEEK

The polymer is linear with little or no branching. It is semicrystalline consisting of the amorphous and crystalline phases. The maximum crystallinity of PEEK is close to 40-45%.^{87,88} PEEK can be obtained either in the semicrystalline or in the amorphous state depending on the processing conditions.⁸⁹⁻⁹¹ Amorphous PEEK can be obtained using fast cooling from the melt, while the semicrystalline structure of PEEK can be generated by slow

heating or by isothermal crystallization at a temperature between the glass transition temperature and melting temperature or by slow heating of amorphous sample from the glassy state to a temperature above T_g .^{90,92} The cold crystallization exothermic process starts at 180 °C when the samples are heated at slow heating rates.⁹²

The crystal structure of PEEK is orthorhombic (Figure 3.2) containing two chains in the unit cell each with two-thirds of the repeat unit.⁹³ The space group of PEEK was reported to be $Pbcn$ ⁹⁴. The unit cell parameters are: $a = 7.75\text{-}7.83 \text{ \AA}$, $b = 5.86\text{-}5.94 \text{ \AA}$, $c = 9.86\text{-}10.00 \text{ \AA}$; they display a certain variation, depending on the crystallization conditions.^{86,93-95}

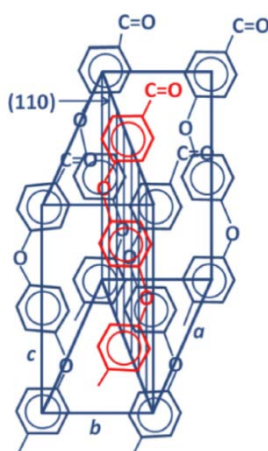


Figure 3.2 PEEK unit cell, adopted from⁹⁶

The dependence of PEEK unit cell parameters on the annealing temperature was studied by different research groups⁹⁷⁻⁹⁹; the results are summarized in Table 3.1. The two different approaches of sample preparation lead to completely different design of experiments.

*Blundell and Mello*⁹⁹ used PEEK crystallized at 325°C and examined the evolution of the crystalline structure by XRD measurements in a temperatures range from 19°C to 291 °. The lattice parameters decreased with decreasing temperature. However, the resulting crystal structures do not represent the "equilibrium lattice" at the measurement temperature, but reflects more the "frustrated" thermal contraction on cooling for the "equilibrium" lattice formed at 325°C.

In contrast, *Hay and Wakelyn*⁹⁸ used originally completely amorphous material subsequently cold crystallized and annealed at temperatures ranging from 184 to 323 °C. It was observed that with increasing crystallization temperature PEEK exhibited a decrease of the lattice

parameters. This was explained by the increased crystal perfection connected to denser lateral packing of the backbones. Variations in the torsional angle of the phenylene groups about the *c*-axis make such densification possible⁹⁷.

Table 3.1. PEEK unit cell parameters as a function of annealing temperature

T_a , °C	a, Å	b, Å	c, Å
Data by Wakelyn* ⁹⁸			
189	7.843	5.937	30.074
216	7.844	5.912	30.138
241	7.845	5.906	29.858
264	7.787	5.855	30.210
282	7.769	5.857	30.376
306	7.741	5.848	30.050
323	7.733	5.844	30.013
Data by Hay et al. ⁹⁷			
184	7.852	0.592	9.981
217	7.828	5.900	9.957
248	7.775	5.882	9.904
250	7.857	5.924	9.987
303	7.724	5.869	9.893
323	7.707	5.875	9.902
Data by Blundell and Mello ⁹⁹			
19	7.767	5.911	9.878
97	7.834	5.932	9.861
145	7.872	5.953	9.878
193	7.924	5.959	9.856
242	7.987	5.965	9.856
267	8.008	5.973	9.856
291	8.048	5.975	9.856

* c-parameter was calculated considering the lattice containing six aryl rings along c-axis in contrast to usual acceptance of the two aryl rings

The melting temperature was reported to be 335 °C^{86,95,99} and T_g is 143-145 °C.^{84,91,92} An equilibrium melting temperature of PEEK was estimated from SAXS by Blundell and Osborn⁹² by extrapolating the position of the low-temperature melting peak versus the reciprocal lamellar thickness (i.e. in the Gibbs-Tomson- coordinates) (Figure 3.3).

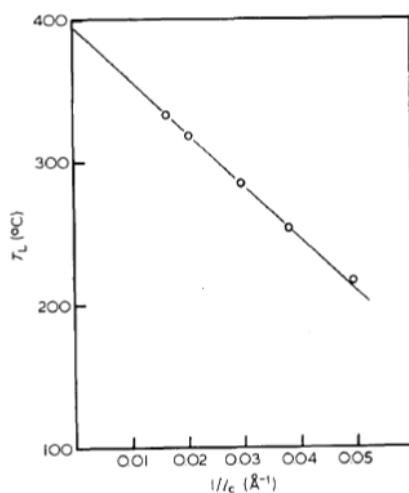


Figure 3.3 Plot of DSC low-temperature melting peak of PEEK sample as a function of the reciprocal of lamellar thickness, adapted from⁹²

Since the low-temperature melting peak was regarded as melting of the crystals initially formed during isothermal crystallization while the high-temperature melting peak was addressed as melting of recrystallized crystals and therefore assumed as not reflecting the initial state of the system. Only the positions of the low-temperature melting peak was used for estimation of the thermodynamic melting temperature of PEEK. When linearly extrapolating this dependence to infinitely thick lamellae, an estimation for T_m^{∞} of 395°C has been obtained.

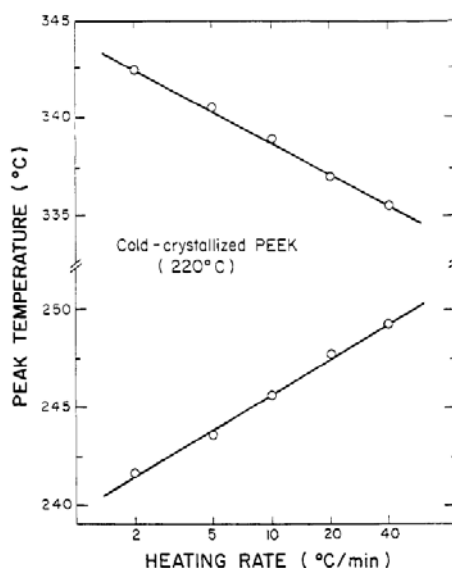


Figure 3.4 Two melting peaks positions as a function of heating rate, adapted from³⁹

Lee and Porter studied dependencies of the PEEK melting temperatures with respect to the heating rate and crystallization temperature using conventional DSC. They observed moving of both melting peaks not only with change of the crystallization temperature but also with the heating rate employed. They concluded that the low-temperature melting peak shifts to higher temperatures with increasing the heating rate while the high-temperature peak shifts downwards (cf.³⁹).

The Hoffman-Weeks plot for PEEK based on data collected by Lee and Porter is shown in Figure 3.5. The Intersection of the high-temperature melting peaks with the line $T_m = T_c$ gives the thermodynamic melting point T_m^0 .

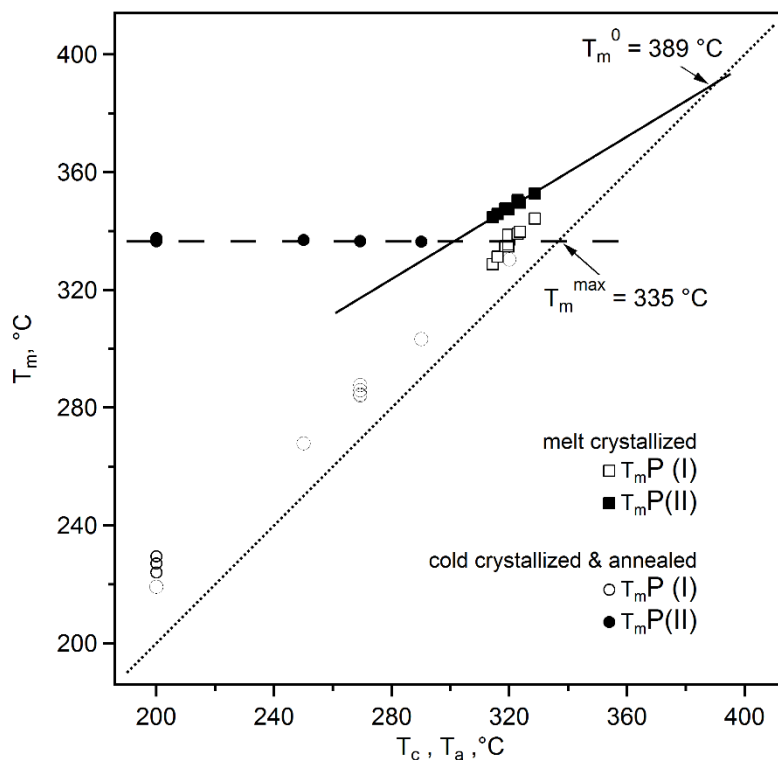


Figure 3.5 Hoffmann-Weeks plot for melt and cold crystallized PEEK. The melting peak positions are plotted with respect to crystallization or annealing temperatures. The open symbols correspond to the low-temperature melting peak, while the solid symbols correspond to the higher-temperature melting peak. Round symbols and square symbols stand for the cold and melt crystallized samples, respectively.³⁹

3.3 The complex thermal behavior of PEEK

Multiple-melting behavior of semi-rigid chain polymers including poly(ethylene terephthalate) (PET), poly(phenylene sulfide) (PPS), poly(butylene terephthalate) PBT, poly(trimethylene terephthalate) PTT, poly(ethylene naphthalenate) (PEN), poly(ether ether ketone) PEEK and others is a subject of debate for more than 50 years and there is still no clear explanation of the nature of this phenomenon.

The double-melting behavior is observed for PEEK samples isothermally crystallized or cooled from the melt by classical DSC and fast calorimetry. The higher-temperature melting peak usually has an onset at 330-340 °C which is not strongly affected by the sample's thermal history¹⁰⁰, while the lower-temperature melting peak onset strongly depends on crystallization conditions and is located 10-15 K higher than the crystallization temperature for the case of isothermal crystallization⁹².

One of the simplest explanations of the double-melting behavior of PEEK would be the existence of two different polymorphs. However, no polymorphs in PEEK have ever been observed by X-ray diffraction.¹⁰¹ This is in contrast to the densification of the chains packing in the crystal, which was observed when annealing at increasing temperatures.^{92,98,100,102}

A considerable number of research papers was published on this question and several models were proposed to explain this behavior. In the following, the underlying ideas and emphasize the main differences shall be briefly described.

The model of "melting-recrystallization" was proposed by *Holdsworth* and *Turner-Jones*¹⁰³ in 1971 for the case of PET multiple melting and it later gained support in the related scientific community interpreting the high-temperature melting peak as the result of a continuous melting-recrystallization process of the originally formed crystals upon heating.^{40,39,88,100-111} *Lee* and *Porter*¹⁰² illustrated a possible process of recrystallization with schemes showing overlap in the sequence of endothermic and exothermic effects resulting in two endotherms on the calorimetry curve (as discussed in Chapter 2.1.10). Such an explanation of multiple-melting behavior is based on the fact that polymers crystallize in metastable states for which the melting point is lower than that pertinent to perfectly stable crystals. It is possible to reduce the free energy of such a system by increasing the lamellar thickness. This can be achieved by melting the material and recrystallizing it at new

conditions at a higher temperature. The kinetics of such recrystallization largely depends on the mobility of the system and a certain amount of time required for the process to occur. The time of recrystallization should be much shorter than the time of crystallization from the amorphous state, since in the former case the nuclei are already present in the system. According to the model, at the slowest heating rates the system will be subject to 100% reorganization, while at the fastest rate the recrystallization process will be completely suppressed. In general, the double melting peak is indicative of partial transformation as was observed in a case of polyethylene.¹¹² The main argument for this model is a dependence of melting endotherms on the scanning rate³⁹. Another evidence for this model is continuous perfection of the crystals with increasing temperature observed by a number of researches¹⁰³⁻¹⁰⁴. *Blundell and Osborn*⁹² pointed out the very similar thermal behavior of PET and PEEK and measured the increase of lamellar thickness for both polymers with SAXS. The enhanced crystal perfection was also observed by WAXS.^{98,100} However, no gain in crystal perfection was observed by keeping the sample at a constant temperature in the case of PET.^{103,107} The SAXS analysis showed a decrease of the long period of PET with the annealing time.^{103,104,113,114} This finding indicates that originally formed crystallites cannot be reorganized during annealing in contrast to some flexible polymers like polyethylene¹¹². Here the difference in the ability for recrystallization between flexible-chain and semi-rigid chain polymers can be traced. Obviously, because of its chain flexibility and mobility in the crystalline phase under certain conditions poly(ethylene) can easily adapt to changing conditions.

Another argument for the model of “melting-recrystallization” was put forward by *Hughes and Sheldon*¹¹⁵ based on the observation that the apparent area under the melting peak is larger than that under the crystallization peak. Based on this finding they concluded that the crystallization process continued after the first endothermal event. However, this argument cannot stand the criticisms based on simple thermodynamic considerations that enthalpy of crystallization should be smaller than enthalpy of melting because of the dependence enthalpy value from the temperature.

*H. G. Kim and R. E. Robertson*¹¹⁶ proposed an approach to estimate the rate of recrystallization by DSC and optical microscopy for the case of PBT. By means of DSC the authors established the half-time of recrystallization measuring the duration of exothermic recrystallization peak in the time domain at the isothermal conditions. With a setup

combining optical polarization microscopy with a Mettler heating stage, the brightness of the crystalline regions was recorded during isothermal conditions. Optical microscopy showed partial melting and recrystallization according to the applied temperature program. The DSC curve also reflected the changes exhibiting broad low-intensity exothermic peaks in the beginning of the isothermal part of the program and sharp endothermic peaks in the regions of partial melting (Figure 3.6).

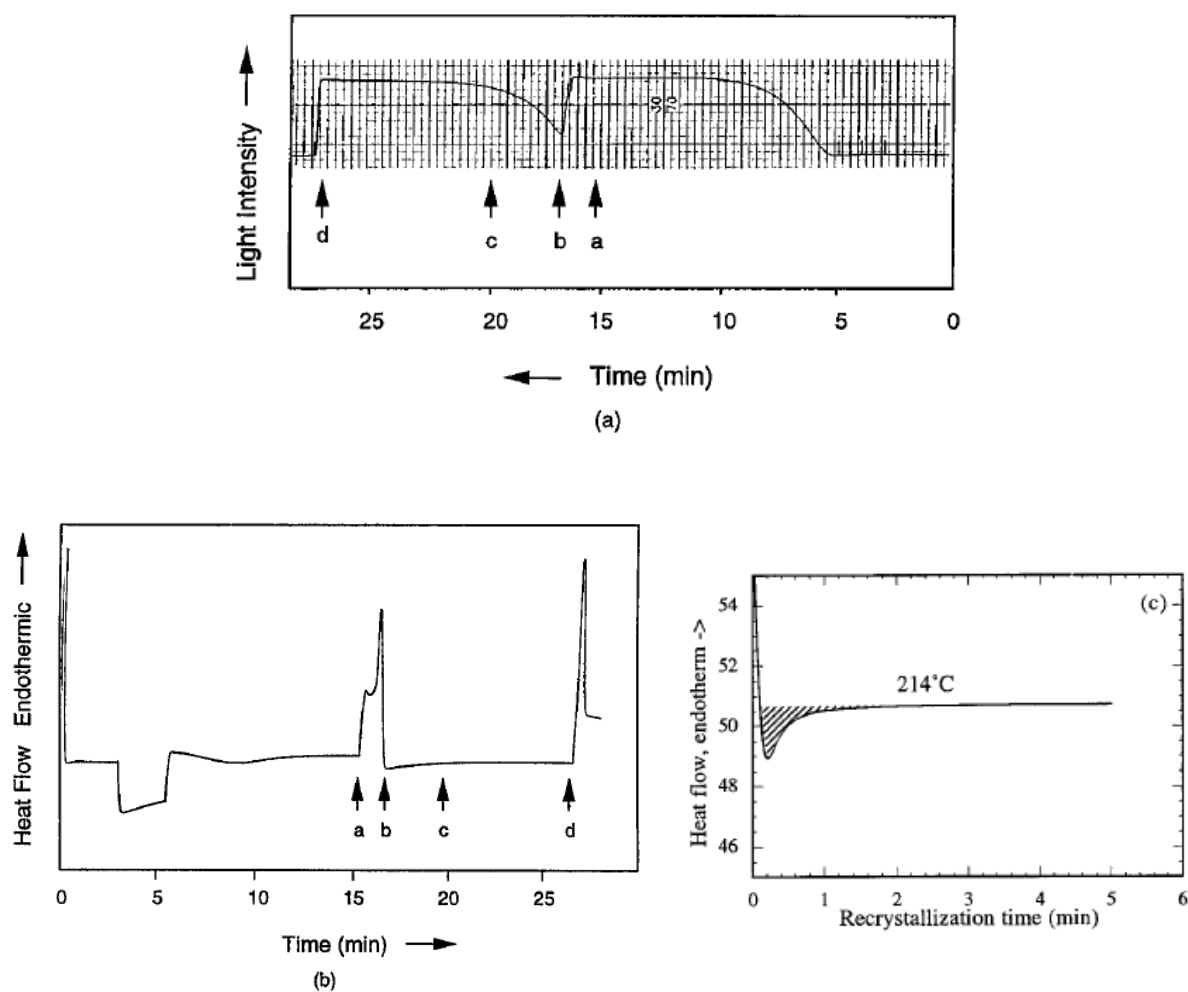


Figure 3.6 (a) Polarized light intensity and (b) the corresponding DSC curve for PBT, using the complex temperature profile and (c) estimation of the recrystallization time, from *Kim and Robertson*¹¹⁶. Partial melting is observed as decrease of light intensity at figure (a) and corresponding endothermic peaks at figure (b)

The recrystallization was found to be up to two orders of magnitude faster than crystallization from the melt at the same temperature and the rate of recrystallization decreased with increase of the crystallization temperature. According to this data, the recrystallization half-

time of PBT at 200-220 °C was roughly 20 s and increased to 8 min at 225 °C. The dependence of the heat of recrystallization at 218 °C with respect to the heating rate in the range of 1-40 K/min was also discussed in the publication.¹¹⁶ The heat of recrystallization increased with increasing heating rate. This observation was explained by the fact that the system had enough time to recrystallize during slow heating ramps whereas recrystallization was mostly suppressed during heating with 40 K/min. Such long recrystallization time is related to the rigidity of the polymer and this shows that semi-rigid chain polymers demand more time for recrystallization when compared to the case of poly(ethylene).

A second popular model explaining multiple-melting behavior addresses multiple melting peaks to the melting of different populations (or different elements of morphology) relevant to the sample history.^{89,90, 117-129.}

*Bassett et al.*¹¹⁷, in support of this model, considered that melting-recrystallization during the DSC scan cannot explain the origin of the two melting peaks of PEEK. They observed no fundamental difference in the melting peak intensities in their experiments of scanning isothermally crystallized at 310 °C PEEK sample at heating rates of 1.25, 5, 20, and 80 K/min. The peak broadening with increasing heating rate was assigned to the instrumental function of the DSC device and was compared with a bismuth standard. The thermal lag of the system was also corrected using a standard sample. *Bassett* also conducted experiments of incomplete crystallization in order to observe which melting point correspond to the first formed lamellae. He scanned PEEK samples, varying the time of isothermal crystallization at 310° from the melt at a rate of 16 K/min, and observed that only the high-temperature melting peak appeared after 6 minutes of crystallization, meaning that the crystallites which form first are those melting at higher temperatures (Figure 3.7). These results may contradict the “melting-recrystallization” model. Similar results were also obtained by other researchers^{124,127,128} but one can argue that in all the mentioned cases heating was performed at relatively low heating rates of 10 - 16 K/min and the recrystallization process could have taken place during such scans.

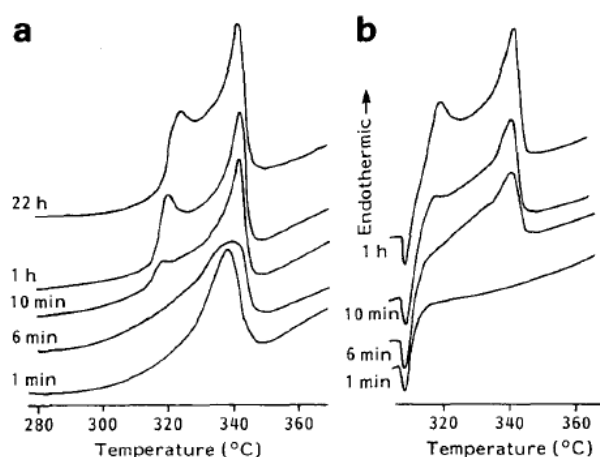


Figure 3.7 DSC curves of PEEK scanned with 16 K/min after crystallization from the melt for different times. (a) Cooled to 200°C after crystallization and rescanned; (b) scanned directly from the crystallization temperature, from *Bassett et al.*¹¹⁷

It is also worth mentioning that PEEK crystallized by cooling from the melt and from the amorphous state has different shapes of the DSC curves⁹⁰. After isothermal crystallization the high-temperature melting peak is comparably sharp and the low-temperature melting peak can be observed at a temperature 10-15 K higher than the crystallization temperature. In contrast, upon slow heating from the amorphous state only one broad melting peak is observed with an onset at 310 °C (peak maximum at 335°C) which is significantly lower than the usual value of the high-temperature melting peak.

Using imaging, researchers were trying to find evidence for the two different morphological components giving rise to two melting endotherms, e.g. by electron microscopy^{90,93,117,122,123,125} and optical polarized microscopy^{92,93,120}. Two individual populations of crystals with a bimodal distribution of the lamellar thickness were proposed for PEEK. Depending on the location where thinner and thicker lamellae coexist in a spherulite, there are two variants of this model. The dual lamellar stack model¹²¹ assumes that thick and thin lamellae are present in separate stacks and the lamellar insertion model assumes that thin lamellae are inserted between thicker lamellae of the same stack. The dual lamellar stack model was formulated, based on microscopic observations¹²⁵. However, it is difficult to make any strong conclusions about morphology based on the solely imaging analysis. The PEEK spherulites can be relatively small (20-40 μm in size¹²⁰) and it is difficult to distinguish clearly two different types of lamellae^{117,125,130,96}. According to the second

model, the primary crystals form stable and thicker lamellae melting at high temperature. The secondary crystallization of thin and less stable lamellae between the primary thicker lamellae results in a lower melting endotherm. This model was corroborated by the results obtained from time-resolved SAXS using correlation function analysis.^{104,131-133} However, several researchers found also evidence for the dual lamellar stack model by employing the SAXS method.^{121,127}

*Blundell*¹⁰⁰ aimed at studying the PEEK structure and morphology as it is being heated in the course of a DSC scan. However, because of the impossibility of performing time-resolved SAXS/WAXS measurements in these conditions, he designed his experiment in a special way. PEEK samples were isothermally crystallized at 210°C for 30 min, then quenched to room temperature and annealed for 2 min at various temperatures in the range of 210-335 °C. The annealing time was chosen to be sufficient to obtain thermal equilibrium but also short enough to represent transient conditions during the DSC scan with a heating rate of 20 K/min. In the case of shortly annealed samples, the long periods obtained from SAXS curves increased with increasing the annealing temperature. Crystal perfection observed as sharpening of diffraction peaks obtained by WAXS analysis was also enhanced. Crystallinity was estimated by integrating the diffraction intensity above and below the fitted profile. The authors claimed that the increase in crystallinity and long period with increasing annealing temperature was caused by changing the periodicity of lamellar stacking. The low-temperature melting peak was attributed to melting of the originally formed crystals becoming unstable at a temperature above the crystallization temperature followed by recrystallization of the molten material.

The increase of the PEEK long period with T_c was also observed by *Kruger* and *Zachmann*¹⁰⁴ in a stepwise crystallization from the melt using simultaneous SAXS/WAXS analysis. It was demonstrated that the total crystallinity of the samples crystallized at lower temperatures was lower compared to those crystallized at higher temperatures. This can be explained by the limited ability of PEEK to crystallize at lower temperatures caused by a reduced chain mobility and reduced kinetics of crystallization.

The first derivative of the crystallinity index estimated from WAXS data resembled the DSC trace with decreasing crystallinity at the temperatures corresponding to endothermic peaks (Figure 3.8). This result was explained by melting of different populations of crystals with

different degrees of crystal perfection rather than by the enthalpy relaxation. The authors mentioned that the additional melting peaks are caused by melting of thin crystals rather than complete lamellar stacks.

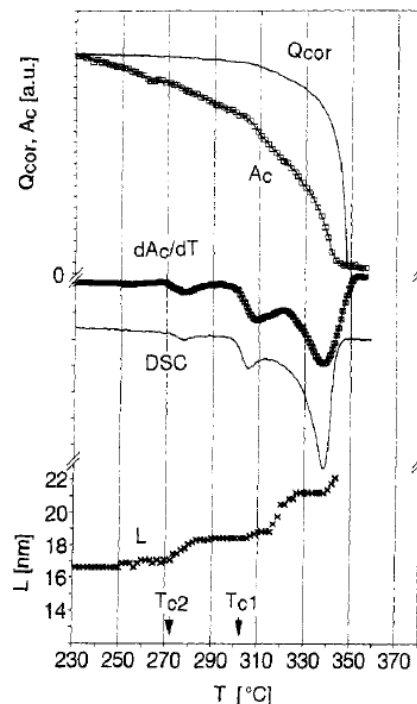


Figure 3.8 Corrected SAXS power Q_{cor} , integral intensity of the crystal reflections A_c and its differentiated form dA_c/dT , and long period L as a function of temperature during heating with 5 °C/min and the corresponding DSC curve of the PEEK sample, from Kruger and Zachmann¹⁰⁴. The sample was annealed at the two temperatures shown with the arrows.

Considering that in the amorphous regions between the already existing lamellae there is only enough space for formation of comparatively thin lamellae not stable at higher temperatures, the authors speculated¹⁰⁴ that two lamellar populations of different thicknesses can grow during isothermal crystallization, and no recrystallization occurs if only the population with thinner lamellae is melted. However, that would imply that two distinct crystal thicknesses have to be observable for every isothermal crystallization temperature. Furthermore, this argument is in contradiction with the initial experiment, since, if both crystal populations are formed during isothermal crystallization, no space would be available for crystals growing at lower temperatures. The only argument one can put forward from this is to speculate that the thinner inter-lamellar crystals are formed during cooling to room temperature after the crystallization rather than during crystallization. However, when crystallizing at low temperatures close to T_g no additional crystals should form in-between the lamellae and no

double melting should be observable. This is in contradiction with the experimental data shown in this work where a clear double melting of PEEK crystallized at temperatures 20 °C above T_g can be observed, as shown in chapter 5.1. The authors argued that when crystallized at relatively low crystallization temperatures the double melting behavior can be explained by partial melting and recrystallization. However, this should strongly depend on the heating rate, as will be shown further in the manuscript.

Based on the analysis of morphological parameters of lamellae during heating of PEEK samples from the amorphous state and after isothermal crystallization *Fougnies et al.*¹³⁴ came to uncommon conclusions when providing different reasons for the existence of the double-melting behavior of PEEK crystallized at 340 °C and at lower crystallization temperatures. In the case of crystallization at 340 °C, the authors proposed formation of two crystal populations of lamellae in approximately equal amounts giving rise to two independent melting endotherms. The authors assigned the lower temperature endotherm to melting of poorly crystalline lamellae formed during the cooling phase which can only reorganize to a small extent on heating because of the constrained environment.

An interesting concept of “triple melting” was described by *Medellin et al.*¹³⁵ in their study of melting behavior of several semi-rigid chain polymers (PEEK, PEN and PET) by characterization with SAXS, WAXS, DSC and polarized optical microscopy (POM). In the course of POM experiments, the authors traced the transmitted light intensity as a measure of crystallinity using a heating rate of 10 K/min. It was observed that melting proceeds in a three-step manner: partial melting of the last-formed secondary crystallized lamellae in the thick regions of the spherulites during the first melting endotherm followed by melting of a larger amount of secondary structures at the intermediate temperature close to the final melting endotherm. The last step of the process was comprised by regeneration of the spherulites followed by their final melting at the third endotherm. In the case of PEEK, the authors suggested that a hypothetical temperature of 10 °C below the final melting point is a second melting endotherm invisible by conventional DSC measurements. The SAXS data showed a slight recrystallization after the first melting endotherm since the average lamellae thickness increased along with increasing long period. The large increase of the long period was noted to be 10 °C below the final melting point. Regeneration of the spherulites before the final melting was also applied to the cases of PET and PEN. The idea of “triple melting”

was also supported by *Sauer and Kampert*^{136,137} in their studies of PEEK characterized by temperature modulated DSC analysis.

Ivanov et al.^{111,138,139} stressed that the connection between crystalline and amorphous phases in the case of semi-rigid chain polymers is much higher than compared to flexible-chain polymers. More energy is needed for semi-rigid chain polymers to form adjacent re-entry folds at the crystalline surface compared to flexible polymers. The majority of the amorphous regions in the semicrystalline structures become perturbed upon crystallization and results in inability of the chain to form regular folds with adjacent re-entry. Amorphous and crystalline phase in semi-rigid chain polymers are tightly interconnected via the chain flux crossing the crystal-amorphous interface which reduces the mobility of the inter-lamellar chains. In addition, chain rigidity, steric restrictions (i.e. bulky side groups) and size of amorphous inter-lamellar regions of semi-rigid chain polymers affect the thermodynamic properties of such materials. All this can explain the high glass transition temperature and a relatively smaller variation of the heat capacity across the glass transition region. In the case of PEEK, the authors observed¹⁰⁹ a decreasing glass transition temperature along with the corresponding increase of the long period upon annealing by a combination of ex-situ AFM, X-ray diffraction and DMTA. This was explained by progressive relaxation of constraints imposed on the crystals by the neighboring amorphous regions.

Ivanov et al. suggested that the interaction between crystalline and amorphous phases in semi-rigid chain polymers and thus, the influence of amorphous phase on the crystalline phase, are underestimated in literature. They introduced a “confinement-induced sequential melting model” for semi-rigid chain polymers based on SAXS and AFM analysis of PTT samples. According to this model^{111,139} melting of semi-rigid chain polymers can be looked at as merging of amorphous regions adjacent to the same crystal, and the process is largely dominated by melting of individual or isolated crystals. In other words, melting of semi-rigid chain polymer is not a random process, but crystals grown in the thinnest gaps melt first which was concluded by analysis of thickness distributions of crystalline and amorphous regions extracted from fits of SAXS curves using a paracrystalline stack model. Growth of infilling lamellae was accompanied by a densification of the lamellae core, which resulted in emerging stress exerted on the growing crystal by the amorphous phase. During heating and subsequent partial melting of these infilling lamellae the stresses imposed on the crystals

release, which stabilizes the rest of the crystals and increases the corresponding melting point (Figure 3.9).

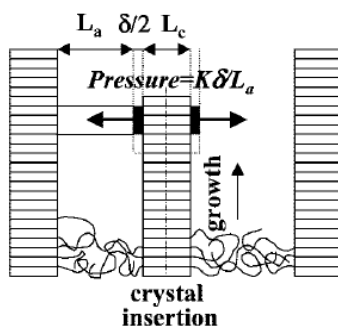


Figure 3.9 The schema showing the origin of negative pressure exerted on a lamellar crystal growing within the scaffold of the dominant lamellae, from *Ivanov et al*¹³⁹.

With the development of fast scanning calorimetry, a new wave of studies on the multiple-melting behavior of semi-rigid chain polymers appeared. Because of the controlled heating and cooling rates up to 10^4 K/s this technique allows performing studies of the double-melting behavior without the influence of reorganization processes during heating. The study of PEEK crystallization kinetics by Flash DSC has been recently reported³⁸ using heating rates up to 2000 K/s. It was concluded that the double-melting behavior of PEEK is caused by reorganization during the heating step. For the crystallization temperatures higher than 260 °C only a single melting peak was observed which was explained by melting of the crystals formed during the isothermal step. As the crystallization temperature increases the recrystallization window gets smaller and the recrystallization kinetics slows down, preventing the formation of more perfect crystals in the course of heating.

Another study of the PEEK double-melting behavior with fast scanning methods was reported by *Jin* and co-workers⁹⁶ based on experiments made with standard DSC, Flash DSC, optical microscopy, Atomic Force Microscopy (AFM) and SAXS which to a large extent led to the same conclusions as the previously described study of *Tardif et al.*³⁸ The authors prepared a large number of PEEK samples with different thermal histories and investigated them by heating at different heating rates in the range of 10 K/min to 2000 K/s. The rate of cooling was observed to be critical for additional crystallization during cooling. Thus, a sample isothermally crystallized at 315 °C and then cooled at 10 K/min resulted in three melting peaks when heating at 2000 K/s. Another sample crystallized in the same way but

quenched at 2000 K/s generated only two melting endotherms. The fully amorphous samples also crystallize during cooling from the melt at 10 K/min, which results in a broad melting peak at 300-320 °C (a similar result was observed in a study by *Cebe* and *Hong*⁹⁰). The authors observed only one broad melting peak in the calorimetry curves when the sample isothermally crystallized at one of the temperatures in the range between 240 and 354°C and then heated at 2000 K/s. They assigned this peak to the melting of the initially formed crystals. They believed that the observation of the double-melting behavior was only a result of slow heating/cooling capability of standard DSC analysis. In fact, one can argue that the temperature range of this observed broad peak covers the region of both melting peaks and it cannot be easily found out which crystals melt there. Thus, based on observation of the two peaks merging with increasing the heating rate their conclusion on the melting-recrystallization nature of the double-melting behavior is questionable.

Another study of PEEK double-melting behavior using fast scanning calorimetry was recently made by *Furushima* et al.¹. Isothermally crystallized PEEK samples were studied by fast-scanning chip calorimetry over a wide range of heating rates from 500 to 60,000 K/s. A fast cooling rate (5000 and 50000 K/s) was used to prevent crystallization on cooling. The authors explained the PEEK double-melting behavior by melting of two crystal populations with distinct melting kinetics. Two different sets of melting endotherms (named peak I and peak II, peak II and peak III) were observed in the calorimetry curves, depending on the applied heating rates. Peaks II and III were observed at a heating rate from 500 to 10000 K/s while Peak I appears as an additional endothermic shoulder at heating rates higher than 20000 K/s in the case of the sample isothermally crystallized at 230 °C (Figure 3.10). In fact, it is hard to make a clear distinction between the two sets of melting peaks and small changes in peaks positions could have possibly been caused by the data treatment. However, in the absence of any other methods of analysis, no further evidence for the existence of “two crystal populations” or any explanations of structural or morphological differences between the two suggested types of crystals were provided by the authors.

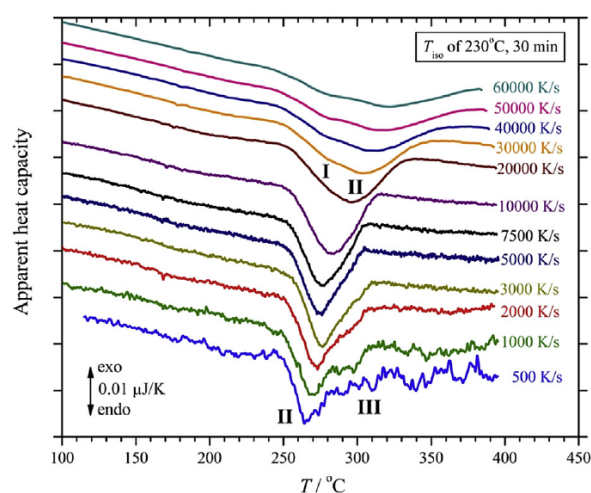


Figure 3.10 Nanocalorimetry curves of PEEK sample crystallized at 230 °C scanned with the heating rates from 500 K/s to 60000 K/s, from *Furushima et al.*¹. Different types of melting endotherms are marked by the authors with the numbers I, II and III.

A combination of micro-focused SAXS with in-situ fast chip calorimetry for investigation of the multiple-melting behavior of semi-rigid chain polymer was for the first time performed by *Melnikov et al.*^{140,141} Samples of poly(trimethylene terephthalate) were isothermally crystallized from the melt and then heated up to different temperatures with in-situ nano-focus SAXS^{140,141} and micro-focus WAXS^{142,143} analyses. By combining micro-focused X-ray diffraction with fast chip calorimetry the critical heating rate for recrystallization of PTT samples crystallized at different temperatures was found and the model of “different crystal populations” as an origin of multiple-melting behavior was critically revised.^{143,144}

It was shown that when heated above the crystallization temperature well-oriented small-angle scattering patterns consist of two symmetrical areas of high intensity were transformed into streaky patterns, which was explained by a loss of long range order in the packaging of PTT crystals. The model of “negative stress” proposed by *Ivanov et al.* and described above was well applied to this case and explained the multiple-melting behavior of PTT as a complex process involving melting of crystals squeezed between thin amorphous gaps and stabilization of the rest of the crystals by negative stress. SAXS data showed agreement with this model when a part of the crystal population was selectively molten in the course of fast heating.

Several open questions, however, are still present in the discussion about the double-melting behavior of semi-rigid chain polymers and PEEK in particular.

The question of whether the high melting crystals of PEEK (340°C) exist before the heating scan or result from a recrystallization process is still open. With standard DSC techniques it was impossible to quench samples after the first moments of crystallization in such a way to prevent further crystallization during cooling. Nowadays, it becomes possible with invention of fast calorimetry devices but still no structural investigations of the early stage crystals of PEEK were made.

The recrystallization process is obviously taking place to larger or lower extent in the course of heating of different classes of polymers, but the exact mechanism of the recrystallization is still unknown even for the case of the most studied polymer – polyethylene. For the case of PEEK, in addition to unknown mechanism, we cannot be sure about the temperature range of the recrystallization. Does recrystallization start just above the low-temperature endotherm or only at a certain temperature when the chains have more energy for re-arrangement?

The recrystallization rate needs to be estimated by means of the techniques complementary to DSC and Flash DSC analysis. Taking into account the chain rigidity of PEEK and its reduced mobility compared to flexible-chain polymers the question of how fast the recrystallization can happen and to what extent it can result in the double-melting phenomenon is still open. Different data for the critical heating rates of PEEK is reported by authors who use fast calorimetry devices. Thus, *Lin Jin* et al.⁹⁶ found complete suppression of the recrystallization process of samples isothermally crystallized at 240 °C when heating at 2000 K/s whereas in the study by *Furushima* et al.¹ the critical heating rate for the same sample is found to be around 4000-5000 K/s.

If we consider the contribution from the melting-recrystallization to the double-melting phenomenon, only the low-temperature endotherm will be observed in the DSC curves above the critical heating rate, according to the scheme of *Lee* and *Porter*³⁹ (Chapter 2.3). The same conclusion was made by *Lin Jin* and co-workers⁹⁶ based on the observation of a broad merged melting peak during heating at 2000 K/s but, strictly speaking, we cannot attribute this merged peak to the melting of any particular type of crystals without appropriate structural information. The nature of the peaks merging with increasing heating rate is still not well understood.

All of the studies referenced above confirm the fact that the macroscopic properties of semicrystalline polymers result from their morphology and crystalline structure, which

depends on their thermal history and crystallization conditions. For this reason, the particularities of the thermal behavior cannot be studied separately from the structural features of the sample under investigation. The structural changes should be addressed at the moment of the event, which means that either time-resolved methods are required. An alternative approach is to "freeze" the system at the desired moment by quenching well below T_g . The difficulty of the second approach is that a metastable polymer system might undergo structural changes at low temperatures or during the quenching itself. Additionally, some of the methods of analysis can potentially destroy the system and change its state, e.g. radiation damage in high-brilliant X-ray experiments, material degradation in the course of electron microscopy^{93,145,146} or thermal degradation in air.^{118,147} On the other hand, in the case of semicrystalline polymers high heating rates are required for the thermal analysis experiments in order to prevent the system from possible recrystallization during heating and be able to investigate the initial state of the system. These restrictions force researchers to design their experiments more carefully by taking into account the capacity of their methods. In the case of PEEK, in order to bring further insights for understanding its multiple-melting behavior it should be helpful to combine fast heating with fast time-resolved structural methods such as SAXS and WAXS analysis.

4 A new approach: nanocalorimetry vs. time resolved micro-XRD

In the first part of this chapter, the specific details and features of the nanocalorimeter employed in this work are introduced including the description of the MEMS-based sensor applied in all the measurements. A newly developed calibration procedure, differing significantly from the previously used approach, is introduced and described. Furthermore, the thermal gradients present on the calorimetric sensor chips is shortly characterized in the context of the basic functional principle of the chip as a simple thermal analysis device without thermal feedback and power compensation facilities. Based on this fact the choice for using solely the onset of thermal transition instead of the peak values is discussed in detail. A method to apply a time lag correction for experiments using heating rates higher than 500 Kelvin per second is set forth, based on the determination of the time response of the sample-sensor system. Subsequently, two technically different approaches are described allowing to extend the temperature application range of the nanocalorimeter to well above the melting temperature of the main object of this study, polyetheretherketone (PEEK), being absolutely prerequisite for the successful realization of the whole project.

In the second part of the chapter, the integration of the calorimetric device into the micro- and nanobeam end station of the beamline is described in detail. Particular challenges and difficulties are described together with possible solutions. The specific setup chosen for the experiments is explained including illumination and collimation schemes, timing and synchronization of the different devices such as beam shutters, detectors, calorimeters, etc. After introducing the methodology applied for X-ray diffraction data analysis, we finally turn to a consideration of challenges arising from the use of highly intense X-ray beams in combination with micron-sized organic samples and short acquisition times on the example of preliminary experiments conducted on PEEK.

4.1 Custom developed Nanocalorimeter

Trying to combine two novel and unique methods designed for the analysis of minuscule samples is always a challenge. Even if commercial devices exist, they normally are designed for exclusive applications alone and do lack the possibility of more elaborate applications or combinations of several techniques of analysis. In case of chip calorimeters, one commercial device is on the market, the Flash DSC I, a prototype of a novel high temperature version of the device reaching temperatures up to 900 °C was recently introduced to the community. However, the measuring sensor is integrated inside the device, which does not allow for easy implementation into nanobeam setups with their special spatial constraints. One of the few exceptions to this claim is the group of *B. Goderis*, which reworked a prototype of the Flash DSC I¹⁴⁸ by adding an electrical breakout options and external sensor holders. However, within this work a custom nanocalorimetric accessory, which was developed in this group, was used. In this case the holder for the nanocalorimetric sensor is separated from the controller box by default, allowing to design it in a much smaller fashion and therefore extend combination capability with complementary techniques. Being based on the use of commercially available nanocalorimetric sensors (see section 4.1.2) the custom device combines the advantage of available sensor modules (no own development and extended competence in the field of MEMS production is required) with fully customizable control and readout capabilities. The fact that the device was developed within the group makes it possible to adjust parameters within the electronics and software in order to match occurring requirements within a short time, which was essential for the success of this work. The nanocalorimetric device consists of a custom made sensor holder and a controller box containing the readout electronics and a high performance data acquisition board. The device is controlled by a conventional WindowsTM computer and does not need additional electronics.

4.1.1 The MEMS-based calorimetric sensor

In the work presented here, commercial nanocalorimetry sensor chips were used, purchased from Xensor[®] Integration. The chips of the Xen 3939-series can be purchased in different configurations, varying in the size of the heated area and achievable maximum heating rates, and different mounting options. An image of the complete MEMS Dye of the calorimetry chip XEN-39392 is shown in Figure 4.1. The Dye consists of a silicon substrate of 300 μm thickness coated with a 1 μm thick amorphous SiN_x layer. The silicon substrate is removed

by wet etching techniques in an area of $900 \times 900 \mu\text{m}^2$ to allow for good thermal isolation and transparency. Two pairs of resistive heaters are placed in the middle of the window generating an actively heated area of $100 \times 100 \mu\text{m}^2$. In addition to the resistive heaters, six Si/AlSi thermocouples are connected in series with the cold junctions placed on the silicon substrate far away from the heated area. The electrical connection of the dye to the outer electrical circuitry is done by wire bonding and therefore fragile during handling and loading of the chip.

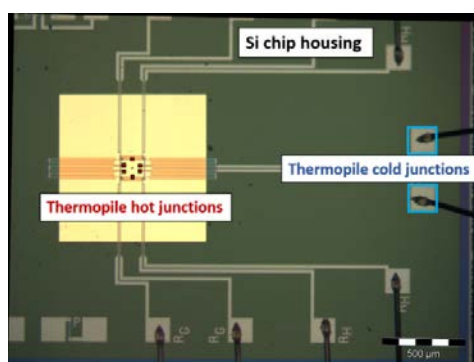


Figure 4.1 Nanocalorimetry chip

The heating of the sample region in the center of the membrane is realized by applying voltage to the resistive heaters. The location and placement of the two resistive film-heaters and the hot junctions of the six serially connected thermocouples are shown in Figure 4.2 in detail.

The outer heater, indicated in yellow, is used as the main heater throughout the experiments, while the inner heater, indicated in red is used to apply a small temperature modulation when used in AC mode (see section below). Six thermocouples are placed around the active area of the central part of the sample place. The geometry of the chip with a rectangular empty space in the middle of the membrane and a low-Z material of which the membrane is made, allows performing *in-situ* experiments with micro-focus X-ray diffraction in transmission geometry. The heaters and thermocouples are covered with a thin layer of a silicon dioxide to prevent electrical short circuits and extensive oxidation of the heaters from the environmental influences. Thus, it allows measuring not only inert solid materials but also gels, suspensions, and conductive liquids.

The material of the membrane, amorphous silicon nitride, has a low thermal capacity combined with a fairly low thermal conductivity. The comparably low thermal conductivity

is required, since otherwise the membrane would serve as a strong heat sink, limiting the application of the device drastically. However, this means that the heating happens dominantly through the surrounding atmosphere, which is in our case air.

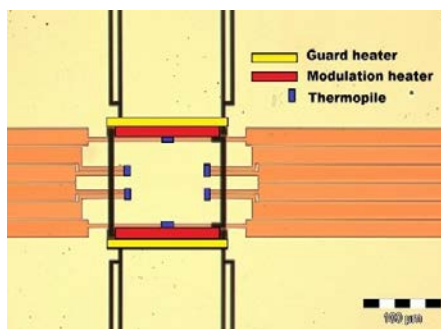


Figure 4.2 Working area of the nanocalorimetry chip

For this chip design the reference temperature is the temperature of the silicon base, which is in our case room temperature. Special chip holders were designed to couple the nanocalorimeter with optical microscopy, and also for simultaneous synchrotron X-ray diffraction (sample holders will be discussed in detail in Chapter 4.2.1).

4.1.2 Working modes of the Nanocalorimeter

Generally, the nanocalorimeter can operate in two distinct operation modes: AC mode and DC mode. In the AC mode a small temperature modulation with an amplitude of ca. 1 K is overlaid on top of a slow heating ramp or isotherm and is therefore comparable with conventional temperature modulated DSC measurements. The modulation frequency used in most experiments is of the order of 35 Hz. Applying on-time Fourier analysis of the temperature response of the sample on the temperature modulation program of the heater, the reversible and non-reversible components of the heat capacity can be obtained. The AC mode is used when slow heating experiments are required and allows detecting very subtle thermal events in nanogram sized samples. Applying a controlled thermal ramp with an overlaid temperature modulation is done easily by using two independent resistive heaters. While a heater with a small heating power is used to apply a constant temperature modulation the second heater is used to apply the underlying thermal program. This has the advantage that the modulation amplitude can be adjusted as the experiment proceeds, compensating for the change of the resistance, and thus of the power output. However, due to the very small

sample mass small heat flow phenomena cannot be recorded, due to the low sensitivity of the thermal sensor.

In contrast to the AC mode, the DC mode operates by applying short heating programs to the main resistive heater on the sensor chip, while the secondary heater is used as an additional thermal sensor. The maximum heating rates achievable with the device depend primarily on the type of the used sensor and its specific characteristics, e.g. electrical resistance, heated area, etc. and can reach up to $3 \cdot 10^4$ K/s for the chips used in this study. Due to the fact that the DC mode works in a burst mode fashion, no real-time feedback can be applied during the thermal program. This makes correct calibration of the resistive heaters a prerequisite for a successful conduction of fast heating experiments which is described in the next chapter in full detail.

4.1.3 Calibration of the calorimetric sensor

As mentioned before, the calibration of the nanocalorimetric sensor is a crucial step for each calorimetry measurement. For chip calorimetry the calibration establishes a direct correlation between the voltages measured at the thermocouples and the temperature of the sample. As an additional way of temperature verification, the temperature dependence of the resistance of the secondary or modulation heater is evaluated during the calibration process. In addition, and due to the fact that no electronic feedback is possible during fast heating in burst mode, a correlation of the heating power and the temperature reached by the resistive heaters has to be established.

Before starting the calibration procedure the sensor chips have to be annealed to avoid a drift of the resistance of the heaters at high temperatures. This is due to the fact, that the Al-Si alloy used as heater material undergoes reorganization at high temperatures, which leads to a slight reduction in electrical resistance and therefore in an increase in heating power with respect to the applied voltage. The annealing takes place at 180° C for at least 8 hours in a vacuum oven. Annealing at the maximum temperature used in the experiments later on would be better in terms of achieved equilibrium performance of the heater. However, the whole chip assembly contains a resin glue which can be degraded after long exposure to high temperature. In addition, the contacts are connected with standard electric solder to the ceramic base and cannot be heat-treated above the melting temperature of the used solder.

As far as the calibration procedure is concerned, standard thermal calibrant particles, e.g. chemically pure In, Sn and Zn were used. The micron-sized metal particles are placed in the middle of the active area of the chip (c.f. Figure 4.3) using an eyelash probe or a soft metal wire. The eyelash has the advantage that it has a sub $3\ \mu\text{m}$ sharp tip allowing for convenient and accurate placement of the calibrant particle. At this stage care has to be taken that the fragile membrane is not destroyed by piercing it with too high force with a rigid wire or needle.

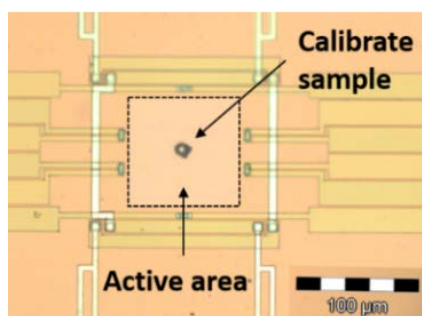


Figure 4.3 Nanocalorimetric chip with a Sn micro particle placed in the middle of the active area

After deposition of each calibrant, heating ramps from 0-9.5 V were applied to the main resistive heater to determine the positions of the onsets of the particular melting peaks. To allow the detection of melting events during heating the slow voltage ramp was overlaid with a small temperature modulation applied on the secondary heater with an amplitude of 0.1 mA and a frequency of 37.5 Hz. In order to avoid thermal lag effects and to reduce the thermal gradient across the active area, heating rates in the range from 6 - 16 K/s were chosen. The thermal gradients on the chip and the thermal lag will be discussed further in this section.

Calibration Software

For the analysis and calibration calculations a new program was developed in the Igor Pro platform from WaveMetrics[®]. The program allows to interactively display several calibration runs and to quickly combine the results and generate a calibration file. Since the heating curves are recorded in the AC mode the amplitude and phase of the thermal response of the calibration sample are visualized in the main window of the program (#1 in Figure 4.4) in red and blue, respectively. The rising amplitude of the response signal is due to the fact that the resistance of the modulation heater increases with temperature. This in combination with a

constant current source applied for the temperature modulation results in an increase in the modulation voltage, and thus, in an increase of the modulation power.

First, the relationship between the representation of the thermal event in the time domain serving for calibration, e.g. the onset of the melting peak of the calibration material, and the known and tabulated melting temperature, has to be established. The identification of melting events in temperature modulated nanocalorimetry is well described in the literature¹⁴⁹. However, the decrease of the amplitude response during the melting process of the metal can be generally attributed to the energy of the modulation being transferred to the partial melting of the metal particle and does not result in a further increase of the particle temperature as the melting sets in.

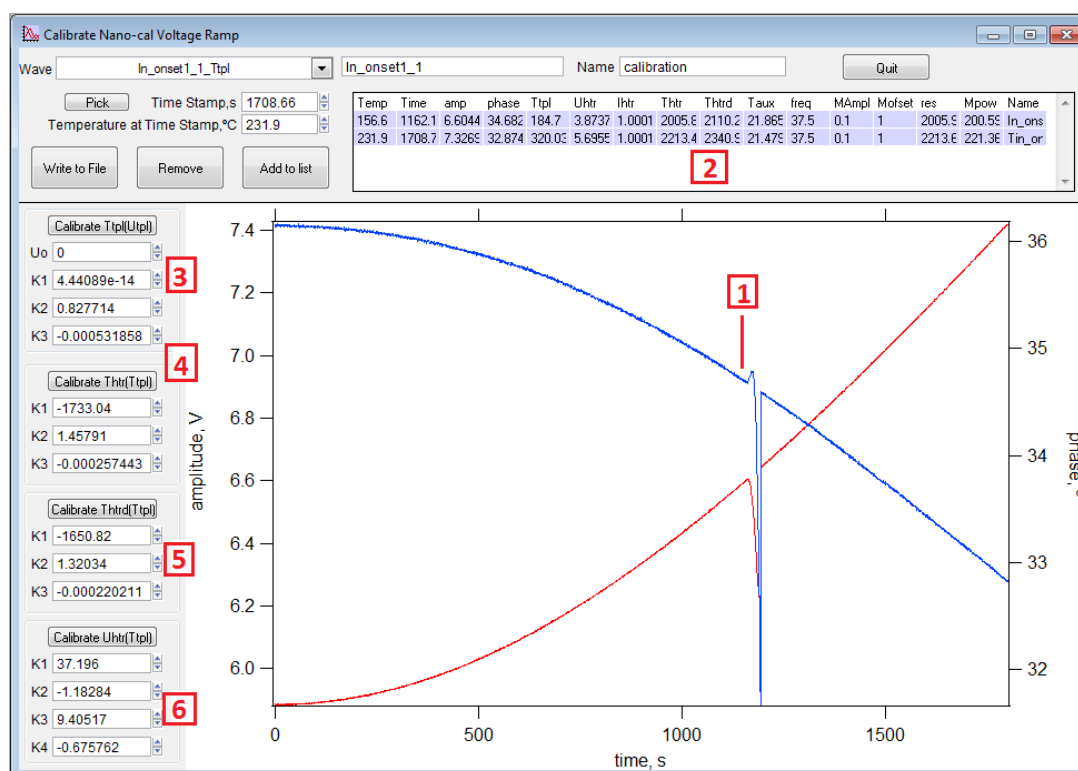


Figure 4.4 Main window of the calibration program. The amplitude and phase of the temperature response of the calibration sample are displayed in the main window [1] in red and blue, respectively. [2] The table summarizing the measured parameters at the time stamp used for calibration. Parameters correlating the voltage of the thermocouple with the temperature in the sample [3] and the resistance of the secondary heater with the sample temperature [4] and [5]. The parameters to establish a correlation of the applied heating voltage on the main heater with the reached sample temperature [6].

The exact time signature of the onset can be identified by linear fitting of baseline and slope in the amplitude curve, i.e. the red curve in in Figure 4.4. The parameters and values of the recorded measurements corresponding to the selected time signature, e.g. amplitude and

phase of sample temperature modulations, temperature of thermopile (T_{tpl}), voltage, current and temperature of guard heaters (U_{htr} , I_{htr} , T_{htr}), temperature of modulated heaters (T_{htrd}), external temperature (T_{aux}) are translated to the table of values (#2 in Figure 4.4, 2) for inspection purposes. In order to establish the correct calibration at least three data point are necessary. Since the starting point of the calibration run is assumed to be well defined, e.g. $U_{tpl} = 0$, this point can be used as a first node for the fit. This means, that at least two more calibration standards suitable for the desired temperature range have to be used in addition.

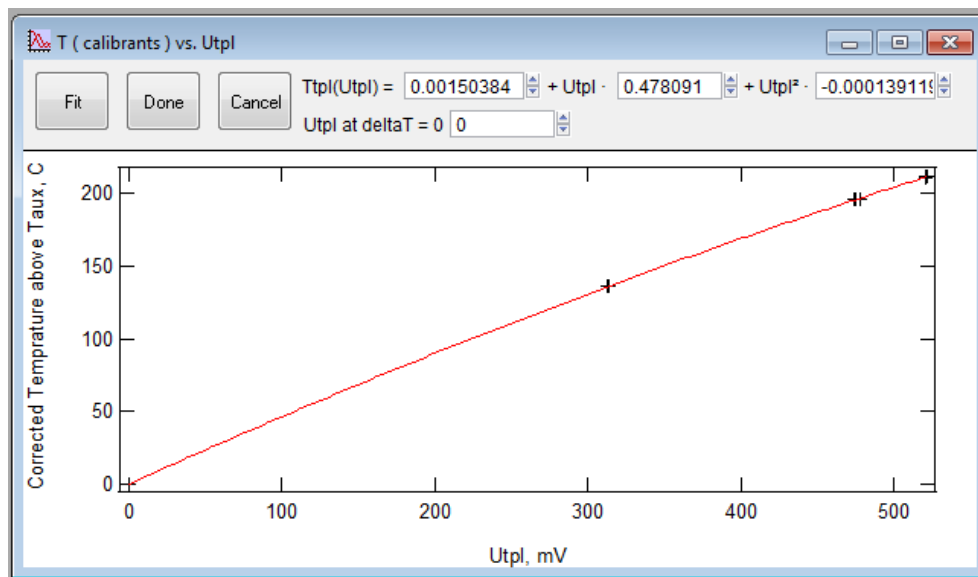


Figure 4.5 Fitting the thermopile voltage (U_{tpl}) as a function of the sample temperature (T_{tpl})

$$T_{tpl} = 0.00150 + 0.47809U_{tpl} - 0.00014U_{tpl}^2 \quad (\text{Eq. 4.1})$$

After creation of the table all necessary dependences can be established (Figure 4.4, 3-6). The calibration of the thermopiles, e.g. the dependence between the thermopile voltage (U_{tpl}) and thermopile temperature (T_{tpl}) needs to be determined foremost being the primary temperature correlation used in all further calibration steps. The T_{tp} vs. U_{tpl} relationship is fitted using a second order polynomial function (Figure 4.5). In this way, the temperature given by the thermocouples corresponds to the actual temperature of the sample, but not to the real temperature at the position of the actual thermocouples. This extrapolation of the temperature towards the sample position on the chip is determined by the geometry of the sensor chip and position of the thermocouples. The implications generated by this extrapolation will be discussed later in this section. The fitting parameter characteristic for a chip of the XEN-

39392 series are summarized in (Eq. 4.1). It can be seen that the sensitivity of the used serially connected thermopiles is of the order of 0.5 K/mV .¹⁵⁰

Using a simple heat-flux device without power compensation and differential sample setup a second temperature reference is required reflecting the baseline for the applied temperature program. In the device described here, the temperature measured by the secondary heater, placed in the direct vicinity of the main heater, is used to establish this reference temperature.

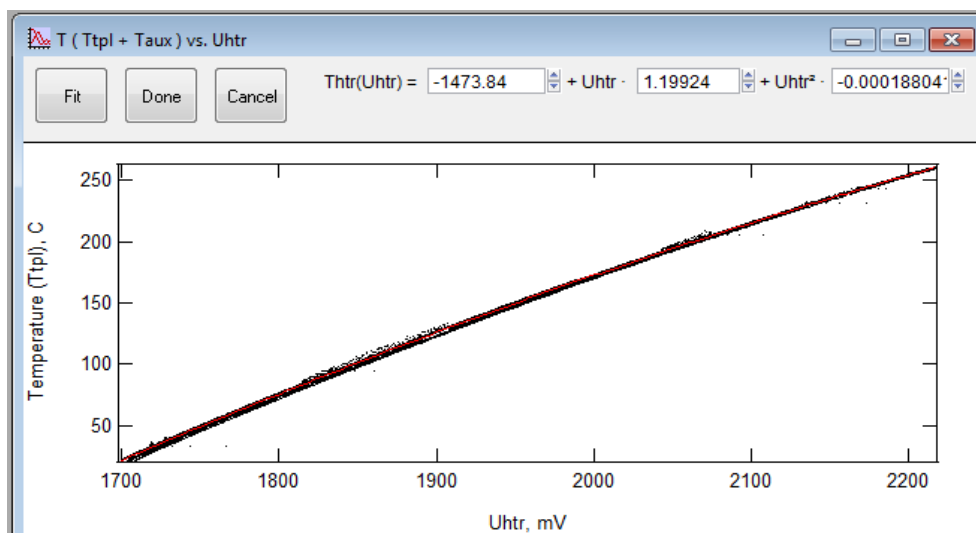


Figure 4.6 Fitting the temperature of the modulation heaters as a function of the measured resistance

$$T_{htr} = -1473.8 + 1.1992R_{htr} - 0.00019R_{htr}^2 \quad (\text{Eq. 4.2})$$

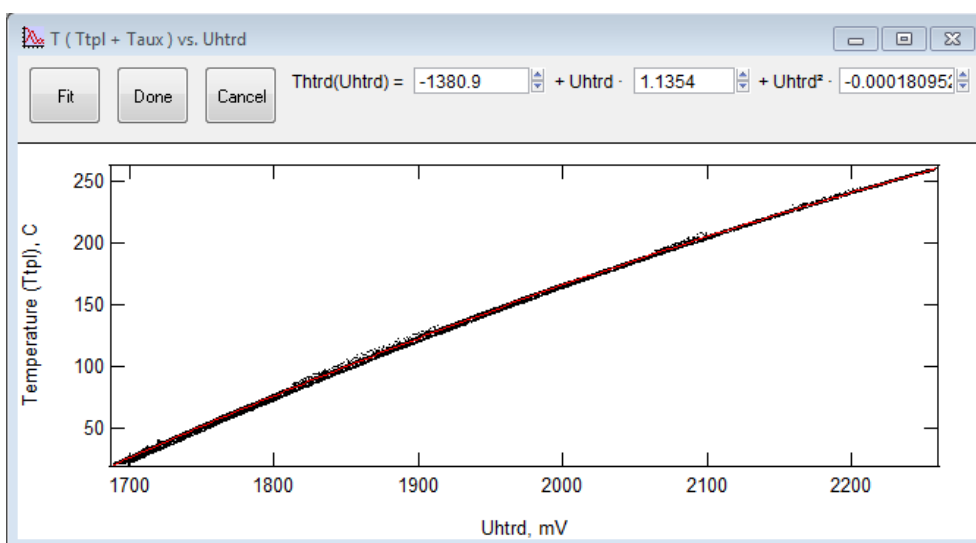


Figure 4.7 Fitting the dynamically derived temperature of the modulation heaters as a function of the measured resistance

$$T_{htrd} = -1380.9 + 1.1354R_{htrd} - 0.00019R_{htrd}^2 \quad \text{Eq. 4.3}$$

The temperature of the secondary heater can be calculated via the electrical resistance recorded at every moment in time by applying a small modulated bias current to the heater and measuring the voltage drop over the resistor. The dependence of the temperature, e.g. the temperature at the secondary heater, and the measured electrical resistance of the same heater is established in the next steps of the calibration when the curves are fitted with a second order polynomial function (Figure 4.6, Eq. 4.4). As seen from the exemplified fits, the second order polynomial function describes the measured values very well.

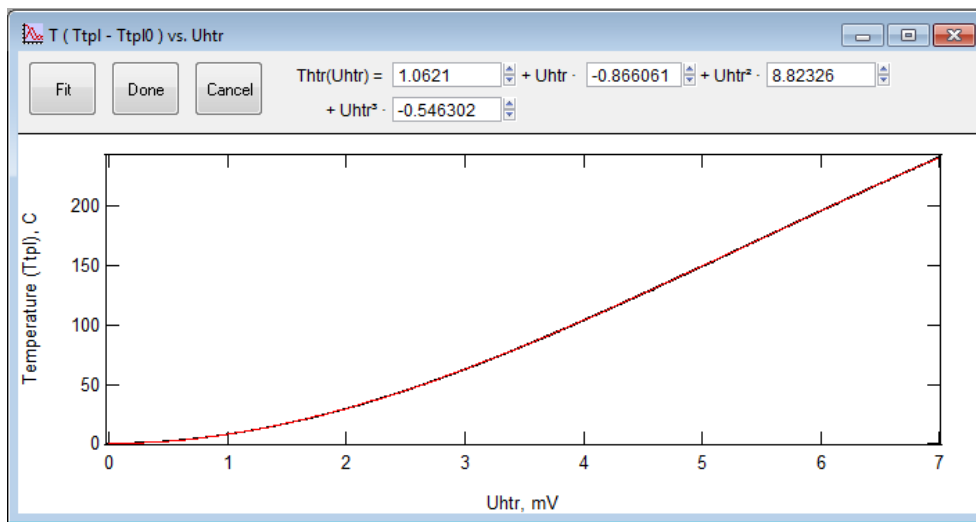


Figure 4.8 Fitting the temperature of the guard heaters as function of the applied voltage

$$T = 1.0521 - 0.86605U_{htr} + 8.8232U_{htr}^2 - 0.54630U_{htr}^3 \quad (\text{Eq. 4.4})$$

In a final step, the temperature of the heaters needs to be connected to the voltage applied to the heaters in order to perform heating to the desired temperature. The voltage applied to the heaters can be connected to the temperature of the heaters by a third order polynomial function (Figure 4.8). This step is critical since it defines the accuracy of the heating program to be applied during operation where no feedback corrections can be applied for possible variations and drifts in the electrical resistance of the main heater. This means that the applied heating power will vary when the thermal resistance changes with time of operation since the heating power scales reciprocally with the electrical resistance. Therefore, repetition of the last step of the calibration is advised from time to time in order to adjust the heating power vs. temperature relation between extended experimental periods. After performing the sensor

calibration all the calibration coefficients are transferred to the calibration file used by the Nanocalorimeter software or can be introduced manually to the calibration panel of the nanocalorimeter as shown in Figure 4.9.

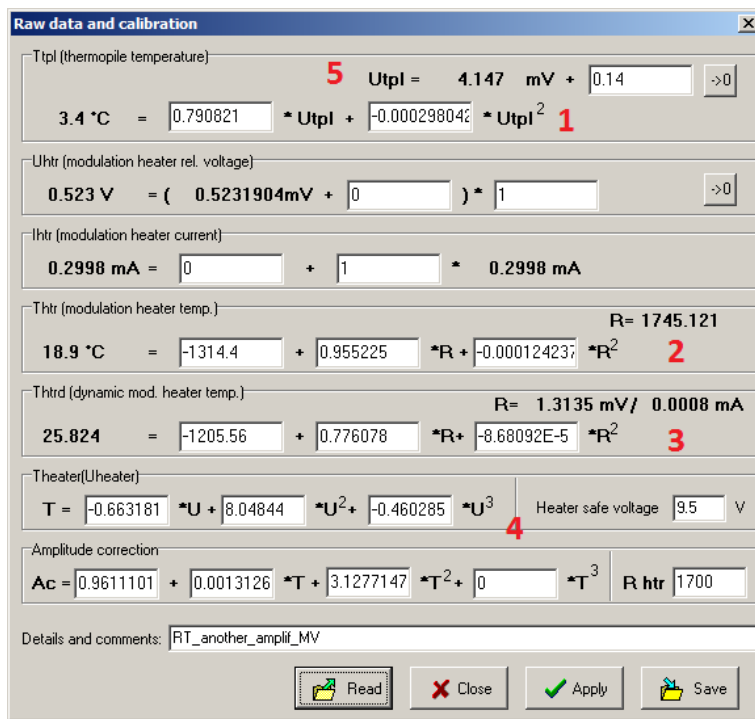


Figure 4.9 Calibration window of the Nanocalorimeter software

To verify the calibration an Indium particle was heated at 6 K/min in an AC mode (c.f. Figure 4.10). The melting peak onset of 156.58 °C is found to be in good agreement with the tabulated value from the literature of 156.6 °C.

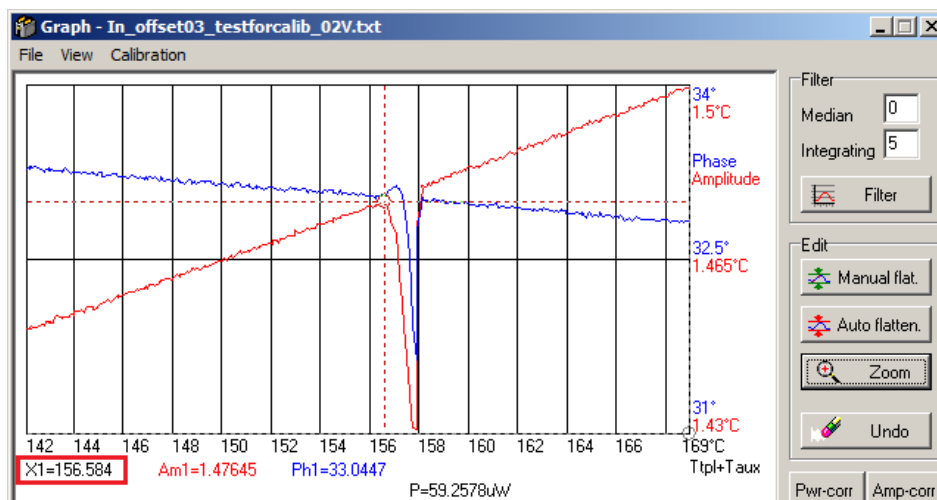


Figure 4.10 Checking the calibration with an In particle

4.1.4 Thermal gradients and the extrapolation of the sample temperature

A specific feature of the sensor chips used in this study is the temperature gradient (cf. Figure 4.11 a and b) they adopt when heated above the surrounding reference temperature.^{151,152} This is due to the particular design where two sets of parallel strip heaters are placed on the SiN-membrane at a distance larger than 100 μm as it can be seen in Figure 4.11, c. The temperature gradients shown in Figure 4.11, a and b, are measured using the apparent delay in the onset of the melting temperature of a small indium particle placed at different positions of the active area in-between the two sets of stripe heaters. The static and dynamic thermal gradients on the chip were determined for two different heating rates: 20 K/min (quasi-static) and 1000 K/s (dynamic). When heating at high rates, a dynamic gradient on the chip appears instead of the static one (Figure 4.11, b). The dynamic thermal gradient increases with increasing the heating rate and with lower heat conductivity of the surrounding atmosphere. The temperature gradient is one of the reasons leading to “smearing” of the heat flow curve when the sample is too large and therefore experiences a substantial temperature gradient. This effect increases with decreasing thermal conductivity of the sample.

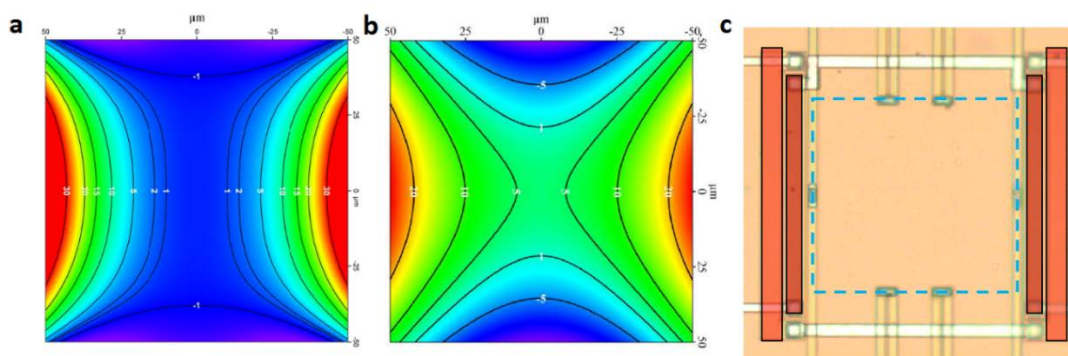


Figure 4.11 a - Temperature-gradient map measured on sensor XEN-392 using a heating rate of 20 K/min (a) and a heating rate of 1000 K/s (b). Figure adapted from.¹⁵² On panel c an empty chip is shown to remind the geometry of the heaters

Even though there is an almost homogenous temperature in the central part of the sample area this has some serious implications on the accuracy of the measured sample temperature considering the fact that the thermocouple hot junctions are put on the edge of a virtual square around the active area where the sample is typically placed. Sectioning a virtual line through the center of the active area the temperature distribution across the sensor can be visualized as shown in Figure 4.12, left.

Coming back to the way the thermopile sensors are calibrated one quickly realizes that we do not measure the actual temperature in the location of the calibration sample but merely extrapolate the thermocouple voltage measured at the moment the calibrant melts towards the sample position.

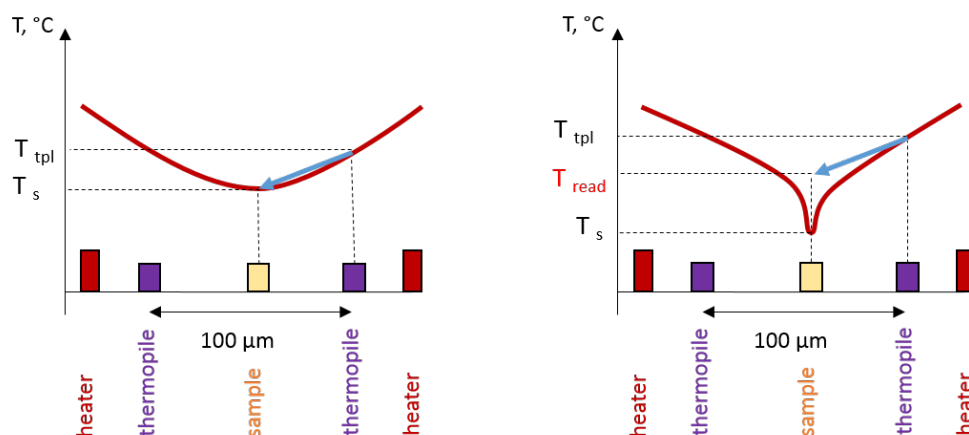


Figure 4.12 (left) Profile of the static thermal gradient on the chip in the case of absence of any thermal event in the sample. (right) Profile of the static thermal gradient on the chip in the case of an endothermic event in the sample

As long as there are no thermal transitions occurring on the sensor involving consumption or release of heat this approach works without problems. However, in the moment when an endothermic or exothermic event takes place, the sample will operate as a heat sink or a heat source and the profile of the thermal gradient will change, as exemplified for the case of a melting transition in Figure 4.12, right. In this case, the apparent sample temperature, as read and extrapolated from the thermopile position, T_{read} , differs significantly from the real temperature at the sample position. This has implications on the sample temperature estimation during first order phase transitions. In other words, the values provided for thermopile readout can only be reliable as long as there is no first order phase transition occurring in the sample. As a consequence, the onset of the thermal transition should be used as characteristic parameter since as soon as the onset is passed the deviation from the extrapolation becomes problematic. This is the main reason that the onset of the melting transitions is used throughout this study to describe the melting process.

4.1.5 Shape of peaks and time constants in nanocalorimetry

The nanocalorimeter used in the current work is clearly equivalent to a simple heat-flux device without power compensation or a differential sample setup. Therefore, an empty cell measurement, reflecting the baseline of the thermal program, has to be conducted to allow for the calculation of the temperature deviation from the temperature program occurring during thermal transitions taking place within the sample. This has to be done, preferably, before the actual experiment and, preferably, using the very same sensor. Care has to be taken that the empty cell measurements are conducted in the same conditions as the actual measurements to avoid shifting of the baseline and variation in the response behavior of the sensor chip.

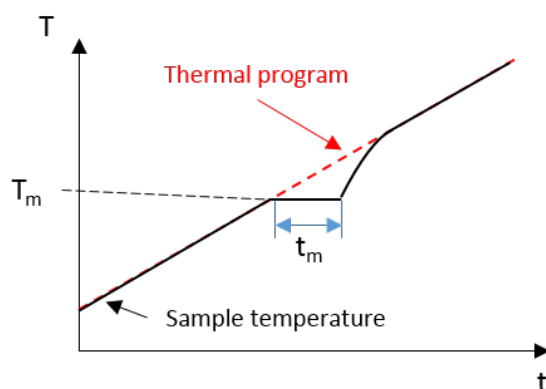


Figure 4.13 Schema showing the appearance of the time delay in nanocalorimetry after a thermal event in the sample

Figure 4.13 shows the theoretical heating program across a melting event as it is characteristic for metals or other low molecular substances when measured with a nanocalorimeter heat-flux device. The main feature is, that in the moment the melting sets in at T_m , the temperature of the sample does not increase further, but stays constant during time interval t_m until the melting of the sample is completed. During the melting process the temperature difference ΔT with respect to the temperature program baseline, or the empty cell reference, e.g. the dotted red line in Figure 4.13, increases linearly. Transforming the measurement from the time domain (cf. Figure 4.13) into the temperature domain by plotting ΔT vs. T_{ref} , (cf. Figure 4.14) it appears that the base line is not at zero, but at slightly negative values. This negative offset reflects the heating power necessary to heat the sample having a heat capacity different from zero. In addition, the melting line, being an iso-temperature line starting at T_m^{onset} , cf. Figure 4.14, reflects the heating rate in the form of its negative slope.

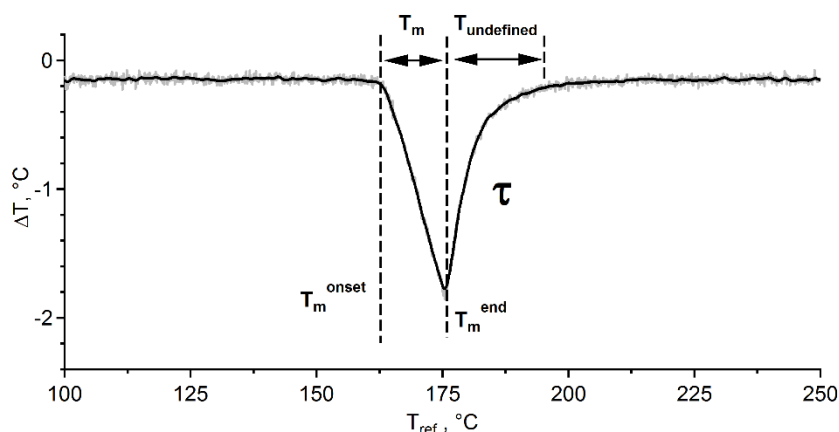


Figure 4.14 Schema showing the shape of a nanocalorimetry curve for the example of In melting

The moment when the maximum amplitude of ΔT is reached, e.g. at T_m^{end} , marks the completion of the melting transition rather than the temperature of maximum conversion as it is the case for classical DSC data. However, one has to keep in mind that the temperature at the end of the melting process, T_m^{end} , is equal to the temperature at the onset of the melting, T_m^{on} and not $T_{ref}(T_m^{end})$, as it appears from this plot. In addition, the apparent temperature at $T_{ref}(T_m^{end})$ does increase with the heating rate as it can be seen in Figure 4.15 where the same indium particle is heated with increasing heating rate. This stems from the fact that the thermal energy has to be brought into the specimen via the surrounding atmosphere. This process is defined by the thermal diffusion coefficient of the surrounding atmosphere and the thermal gradient. However, the thermal gradient as well as the diffusion coefficient do not change significantly with increasing heating rate, rendering the time used for this process quasi constant. Thus with increasing heating rate the apparent peak temperature $T_{ref}(T_m^{end})$ increases with increasing heating rate. Considering all these arguments, it does not make sense to use $T_{ref}(T_m^{end})$ to characterize melting, as it is done in several reports in the literature^{38,1}, but to use the actual onset of the melting transition, T_m^{on} , instead.

Another reason to do so is the fact that during the time at which the thermal transition takes place the temperature of the sample cannot be measured precisely for the reasons described in the section above.

As mentioned before, the measured sample temperature increases after the melting process is completed following an exponential curve until it catches up with the thermal program. The time constant τ of this recovery corresponds to the time response of the sensor characteristic for the particular sensor geometry and depends on the thermal gradient between the sample temperature and the external temperature around the chip as well as on the conductivity of the gas.

4.1.6 Thermal lag of the Nanocalorimeter

In the Nanocalorimeter, as in conventional DSC instruments, a thermal lag between the controlled furnace temperature and actual sample temperature can be observed. The thermal lag is caused by the time the heat needs to be transferred between the heater and the sample. In other words, the thermal lag is a temperature difference caused by the characteristic response time τ of the device and can be expressed as a function of heating rate β by:

$$\Delta T_{lag} = \tau\beta \quad (\text{Eq. 4.5})$$

In classical DSC devices the thermal lag is much smaller than the temperature increase within a given time and thus, the thermal lag can be neglected in most of the cases. However, when heating at increasingly high heating rates, situations can occur where the reciprocal heating rate becomes comparable to the response time of the thermal system.

If the thermal lag is not considered, the temperatures picked from the curves, e.g. onsets of melting peak, will ostensibly depend on the heating rate. This effect is nicely demonstrated in Figure 4.15 where the very same Indium particle is heated above its melting temperature with increasing heating rates. In the shown measurements, the onset of melting of the Indium particle ranges from 157 °C for a heating rate of 100 K/s to approximately 210 °C for a heating rate of $3 \cdot 10^5$ K/s. Plotting the melting temperature onset as a function of heating rate a linear correlation can be identified according to:

$$T_m^{on}(\beta) = T_m^{on}(0) + \tau\beta \quad (\text{Eq. 4.6})$$

Where β corresponds to the heating rate and $T_m^{on}(0)$ is the onset temperature extrapolated to a heating rate of 0 K/s.

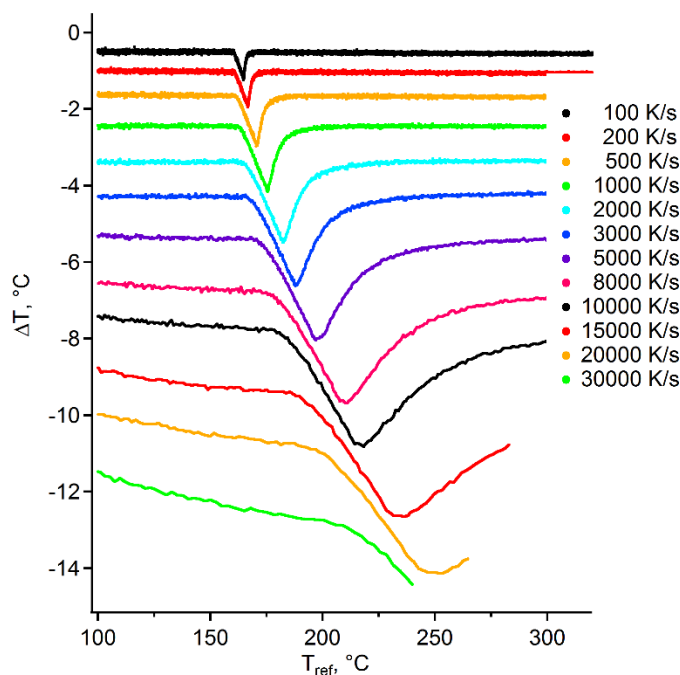


Figure 4.15 Nanocalorimetry curves of In melting measured at heating rates in the range of 100-50000 K/s

The slope of the linear fit corresponds to the response time of the sensor setup and values of $\tau = 1.75$ ms. In order to correct the nanocalorimetric curves, every curve has to be shifted in the temperature domain according to Eq. 4.5.

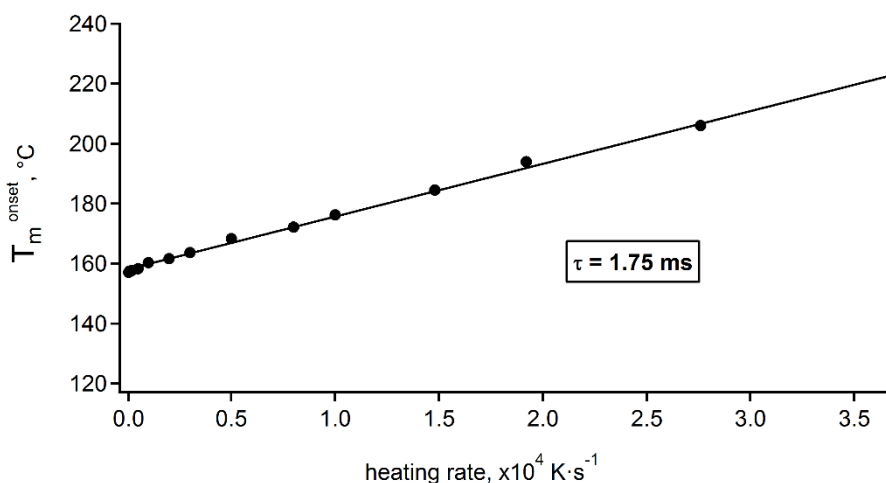


Figure 4.16 Melting temperature of In micro-particle measured at different heating rates for determination of the nanocalorimeter characteristic time

4.1.7 High-temperature version of the Nanocalorimeter

The working temperature range of the base version of the nanocalorimeter employing the commercial sensors XEN 39392 ranges from room temperature up to ~ 360 °C. This constraint in the operating range is caused by several instrumental restrictions. The first limiting factor is that the maximum voltage the controller can apply to the main heater is limited to 10V, rendering the resulting heating power too small to reach higher temperatures. Higher voltage cannot be applied and higher temperature cannot be reached without modification of the device. In addition, the supplier of the MEMS devices advises to not increase the voltage further, since it can trigger degradation processes in the heater leading to nonlinear response behavior and subsequently to failure and destruction of the device. However, one has to consider that due to the temperature gradients present across the active area of the sensor, as discussed in Section 4.1.4, the temperature of the heater is much higher than the target temperature in the center of the active area.

High temperatures of ca. 400 °C, needed for the current work, where the melting of PEEK is studied, require therefore an additional heat source being, both, compatible with the nanocalorimetric measurements themselves, but also with the constraints of the micro-focus setup of the beamline described in the following section. Two principal solutions were developed and successfully tested throughout this project. The first solution was the use of a commercial heating stage optimized for optical microscopy (Mettler Toledo FP82HT) as additional external heat source, while the second solution involved the use of the secondary heater to add an internal temperature offset.

1. Applying external heating

In order to use Mettler Toledo FP82HT as external heating source some modifications had to be made to the heating stage itself. First, an aluminum adapter holding the nanocalorimetric sensor in a position by avoiding contact of the bond wires of the MEMS-dye with the heating plates of the stage, had to be designed and fabricated. Furthermore a new connector for the electrical contacts had to be designed including a 3D printed housing to avoid exposure of the current-carrying leads (cf. Figure 4.17).

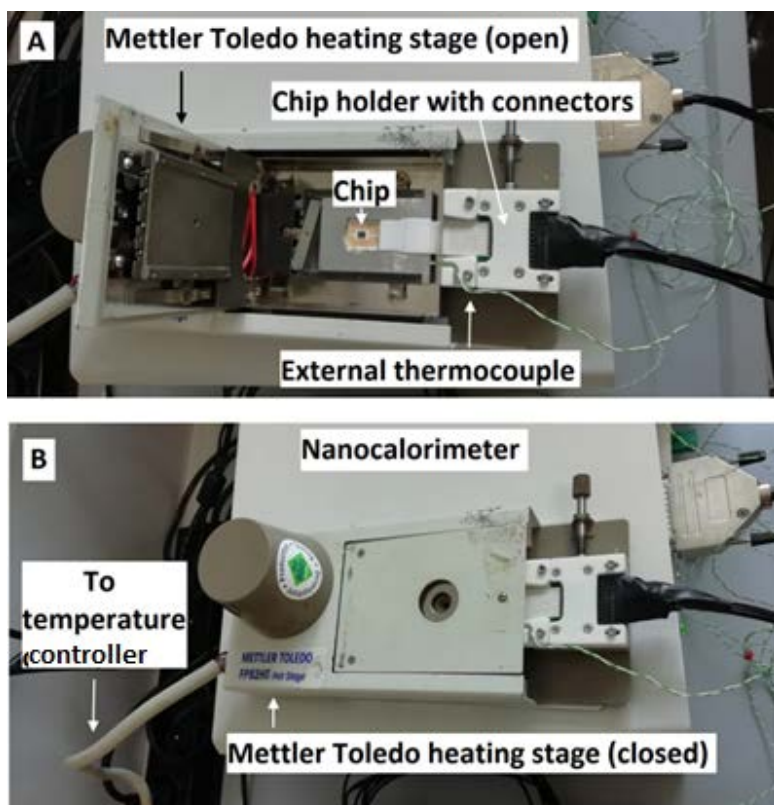


Figure 4.17 Nanocalorimeter chip with a chip holder designed for the Mettler heating stage

To reach 400 °C with the nanocalorimetric sensor the Mettler heating stage was set to 80 °C. This outer reference temperature was kept throughout the experiments. Using this configuration, the calorimeter was able to reach a maximum temperature of 430 °C as confirmed by using Zn ($T_m = 419.5$ °C) as a reference for temperature calibration.

Being an easy and quick solution for the offline nanocalorimetric measurements, the bulky device was not very well fitting with the particular constraints regarding the in-situ X-ray diffraction measurements. To fulfill the requirements with using an external heating source the device has to be as small as possible. With the heating stage from Mettler Toledo a combined experimental setup for the micro-beam end-station of the beamline was still feasible. However, additional care had to be taken when it came to sample changes involving adjustments of pinholes and flight-tube, etc. The particular challenges involved will be discussed in the next section of this chapter.

2. Using the modulation heater as an additional heat source

An alternative approach was based on the use of the nanocalorimeter modulation heater not as an additional thermal sensor but as a heating element during burst mode measurements. This allowed applying an internal temperature offset of 110 °C.

Reduced sensitivity of the thermocouple

One caveat of increasing the working range of the nanocalorimeter beyond 360 °C was the required change of the sensitivity of the internal thermocouple. This stems from the fact that in the standard configuration of the nanocalorimeter the amplification factor of the thermocouple signal was well matched to the accessible range of the analog-digital converter of the data acquisition electronics. In order to allow for a larger range of temperature to be recorded the amplification factor was reduced by a factor of 1.5.

4.1.8 Technical aspects of the sample preparation

All sample preparations were performed under optical microscope observation. The experimental setup for sample preparation is shown in Figure 4.18. For each measurement, a single grain of PEEK selected from a powder sample was placed in the center of the active area of the calorimetric chip manually using an eyelash. The sample was then melted to erase all previous thermal history. This also provided a good physical and thermal contact of the polymer drop with the support membrane. This is of importance to avoid movements of the object on the membrane since the chip will be placed in the upright position when mounted in the micro diffraction setup.



Figure 4.18 Process of sample preparation. Left - Nanocalorimetry chip with a chip holder is placed under the microscope and connected to the Nanocalorimeter in order to perform sample preparation, right – close view of the nanocalorimetry chip under the microscope.

After a short heat pulse of 1-2s to 410 °C, the sample was immediately quenched to a crystallization temperature and then subsequently crystallized for 30 min at different crystallization temperatures in the range from 190 to 300 °C. For the lowest crystallization temperature selected in this project, i.e. $T_c=170^\circ\text{C}$, the crystallization time was increased to 40 min to allow for a more complete crystallization.

Due to the thermal gradient across the active area of the chip, as extensively discussed in chapter 4.1.3, it is important to not place the polymer particle close to or on top of the heaters. In addition, the size of the particle should be chosen regarding the desired heating rates. When aiming at high heating rates the sample mass needs to be small in order to avoid excessive convection effects generated by the response time of the setup, but also by the thermal gradients. Aiming for experiments using X-ray diffraction larger sample volumes are desired to increase the amount of scattering volume and thus the overall recorded signal. However, this means that one has to sacrifice the ability to reach heating rates higher than 5000 K/s.

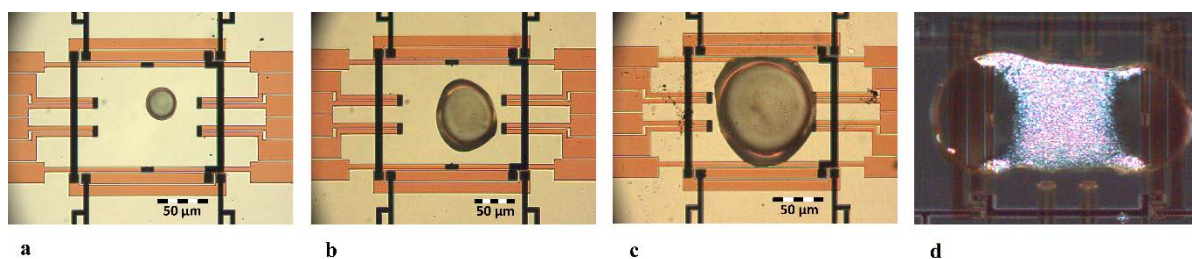


Figure 4.19 Images of PEEK samples of different sizes. Particles with the smallest size as on figure *a* are better for high heating rates, e.g. $10^3\text{-}10^4$ K/s). For the off-line nanocalorimetry measurements particle sizes as shown in figure *b* were used. For the micro-diffraction measurements particles with a size closed to the one on figure *c* were used. Figure *d* shows the process of crystallization, as imaged by optical polarized microscopy.

Different PEEK sample sizes were deposited on the active area of the chip used for the different types of experiments are shown in Figure 4.19 (a - d). Using similar sample sizes the off-line nanocalorimetry measurements and in-situ X-ray diffraction measurements will result in similar baseline behavior, thus increasing the comparability of the experiments conducted in the different environments. The latter was regarded as being more important than simply maximizing the achievable heating rate. As a result, all series of nanocalorimetry measurements were made using similar sample sizes. For micro-diffraction experiments it was impossible to reuse the sample once exposed to X-rays because of the radiation damage.

4.2 Nanocalorimetry combined with microfocus X-ray diffraction

The nanocalorimetry setup was designed to be compatible with the sample environment of both experimental hutches of ID13. However, the in-situ fast heating measurements were conducted entirely at the micro-branch of ID13. The reasons for that are manifold. First of all, the overall achievable X-ray flux is 2 orders of magnitude larger when using the Be-transfocator. The second reason is that, as stated before, it is advisable to match the size of the X-ray beam with the size of the specimen to maximize the scattering volume while minimizing the locally applied radiation dose leading to structural deterioration of the material caused by radiation damage. The main components of the used setup will be described in the following section.

4.2.1 Sample holders

Special chip holders for the nanocalorimetric sensors were designed to be compatible with the constraints of the ID13 microfocus setup. In order to reduce parasitic air scattering originated from the primary beam passing through the air on the upstream side of the sample the pinhole should be placed close to the sample in a distance of only a few millimeters (c.f. Figure 4.20). Therefore, the chip holder was designed to be not more than 2.5 mm in thickness while the calorimetric sensor is placed on the downstream side of the assembly.

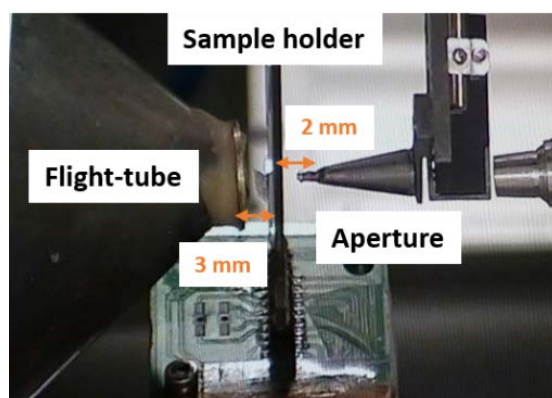
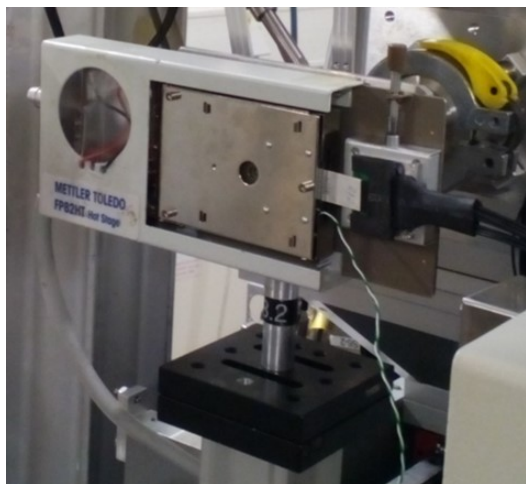


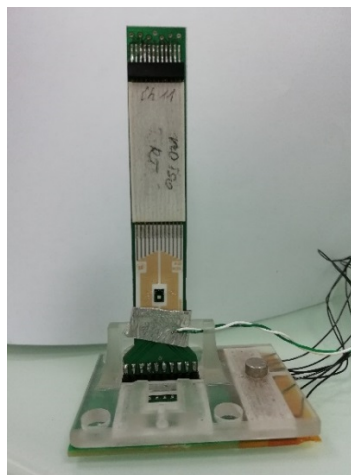
Figure 4.20 Close view of a setup in working state. Distances between the aperture and the sample stage and between the sample stage and the flight-tube are both around 2-3 mm.

Furthermore, no additional covers were added at the downstream side to allow to approach

with the helium flight tube as close as possible to the sample to further reduce air scattering background.



a. Chip holder with a nanocalorimetry chip in the Mettler heating stage for measurements in-situ with X-ray micro-diffraction using external heating



b. Chip holder with a nanocalorimetry chip for measurements in-situ with X-ray micro-/nano-diffraction



c. Chip holder with a nanocalorimetry chip with ceramic housing for measurements in-situ with X-ray micro-diffraction



d. Chip holder with a nanocalorimetry chip for sample manipulation under microscope

Figure 4.21 Sample holders used for nanocalorimetric measurements; a, b and c were used for combined in-situ experiments, while d was used for offline measurements.

Four different sample holder designs are summarized in Figure 4.21 (a-d). As discussed before, a Mettler heating stage was used in the early experiments as an external heater when combining nanocalorimetry with micro-diffraction (see Figure 4.21(a)).

The first issue with this particular setup is the fact that the final pinhole needs to be placed vicinity of maximum 4 mm upstream the sample. This required the design of a nozzle-shaped pinhole holder (cf. Figure 4.20) allowing to insert the pinhole into the heating stage. As a consequence, the temperature of the heating stage affected the lateral position of the pinhole by inducing thermal drift so that the pinhole had to be realigned continuously in between the measurements.

Secondly, the bulky stage had to be removed every time to allow the placement of a new sample. Firstly, the sample was brought close to the aperture in such a way that the nozzle of the pinhole was inserted into the Mettler heating stage. After this, the flight-tube was brought close to the heating stage in a way that an air gap of less than 1 mm remained. This was required since the entrance window of the flight-tube is only 5 mm in width limiting the maximum accessible diffraction cone. All the X-ray diffraction measurements recorded using this setup had a substantial background pattern reflecting the shape of the flight-tube entrance window. This showed that the air gap around the sample was still too big and the pinhole and flight tube should have been brought closer together. Extra patience and time had to be invested when working with this setup reducing the overall productivity during beamtime to about one measurement in 30 minutes of beamtime.

After revising the Nanocalorimeter for the high temperature modification using the secondary heater it became possible to perform experiments without external heating device and the standard chip holder developed earlier could be used. The simplest version is shown in Figure 4.21(b) and Figure 4.20. At a later stage of the project, another sample holder design was tested allowing to use an alternative sensor design. This chip holder, shown in Figure 4.21(c), was also designed to potentially allow measurements in a controlled atmosphere. This is required when extending the application of this method to more volatile samples or materials prone to oxidation. The holder shown in Figure 4.21(d) was used during sample preparation prior to the beamtime since it is designed to be compatible also with optical microscopy.

Two different types of chip designs were used throughout the project. The XEN 39392 with a paper isolated flat cable connector and XEN 39392 with a ceramic carrier. They have the

same sensor type and layout of the active area but differ in chip support and electrical connections.

4.2.2 The X-ray micro diffraction setup

The home-built nanocalorimeter can operate in DC and AC modes applying the required temperature programs to the heaters of nanocalorimetric sensors while recording fast temperature readout from the thermocouple. As described before, the sensor is physically separated from the controller box of the nanocalorimeter. This allows the implementation of the sensor into the constrained beamline environment and to perform simultaneous X-ray diffraction measurements in transmission geometry. The principal setup of the ID13 micro-diffraction end-station is depicted in Figure 4.22.

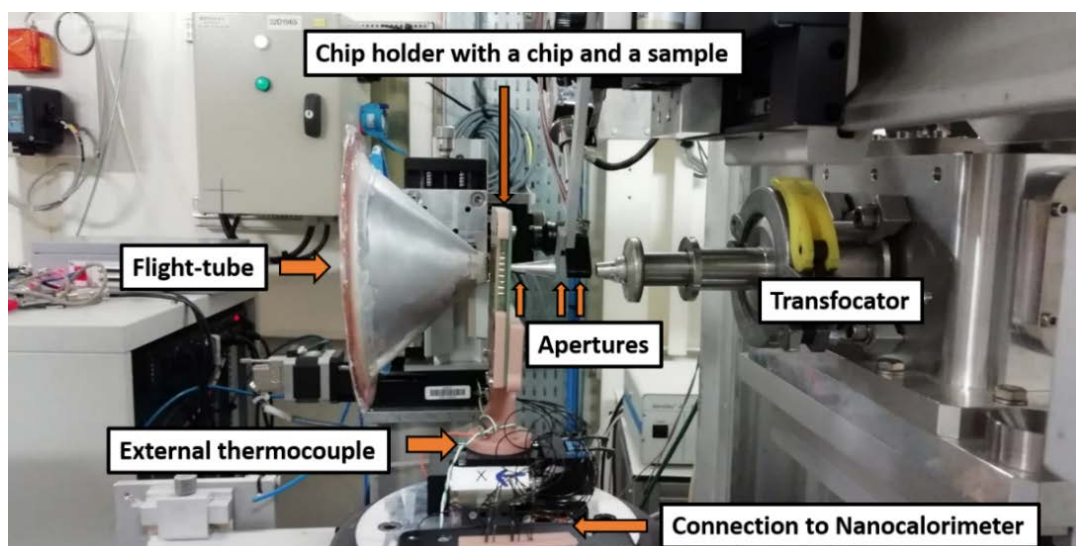


Figure 4.22 Side view for the setup combining in-situ fast chip calorimetry with X-ray microdiffraction in a ready-to-measure state at the microbranch of ID13, ESRF

The X-ray beam enters the sample space from the transfocator shown at the right side of the photo. The focal distance of the X-ray beam, as measured from the surface of the transfocator vacuum housing, is about 240 mm when an X-ray photon energy of 13keV is used. The steel nozzle leading to the apertures serves as additional screening to reduce background scattering. A set of three apertures is used as collimation scheme and will be discussed later in this section in detail.

The chip holder is placed on top of the main sample translation stages comprised of an X-Y-Z gantry allowing to align the sample in all three directions. In addition, an air bearing rotation stage (Micos UPR-170) equipped with two centering stages which are used in order to allow the exact angular alignment of the chip membrane for potential texture or single crystal measurements.

In Figure 4.23. A front view of the setup is shown in a state before the sample changing with the flight-tube retracted from the beam pass and the sample stage moved away from the aperture.

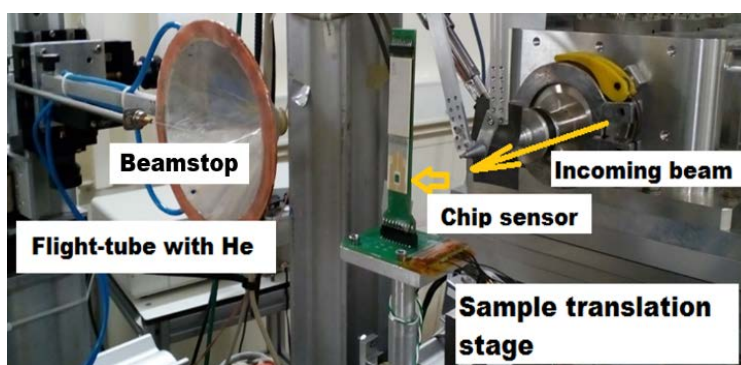


Figure 4.23 Front view for the setup of combined in-situ fast chip calorimetry with X-ray at the microbranch of ID13, ESRF

The final alignment of the sample prior to the X-ray measurements is performed with the help of a retractable on-axis optical microscope with long-distance objectives of 5x or 50x magnification. The focus of the microscope is calibrated to coincide with the X-ray focus. For more convenient operation sample position coordinates can be stored and restored in the

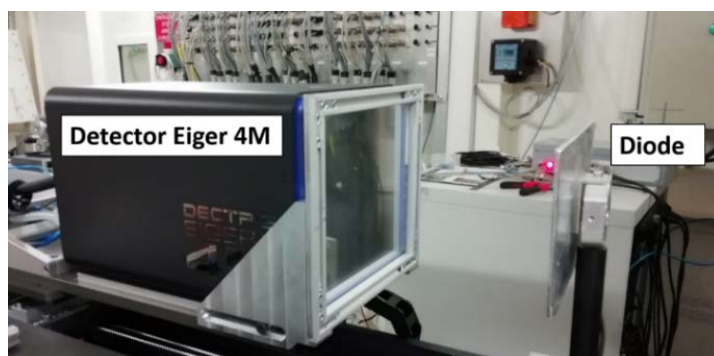


Figure 4.24 Eiger 4M detector used for the X-ray microdiffraction measurements in a position “out” protected from an accidental X-ray exposure with a lead screen. The photodiode was used to scan the direct beam and the beamstop position during beamline alignment.

beamline control software easily. The detector is placed downstream the sample on the motorized detector support and can be moved vertically and laterally in order to select the desired scattering range for the particular experiment (c.f. Figure 4.24).

In the case of using the Mettler heating stage as an external heater the setup became more bulky and the procedure of sample changing became more complicated and time-consuming as mentioned before, shown in Figure 4.25 and Figure 4.26.

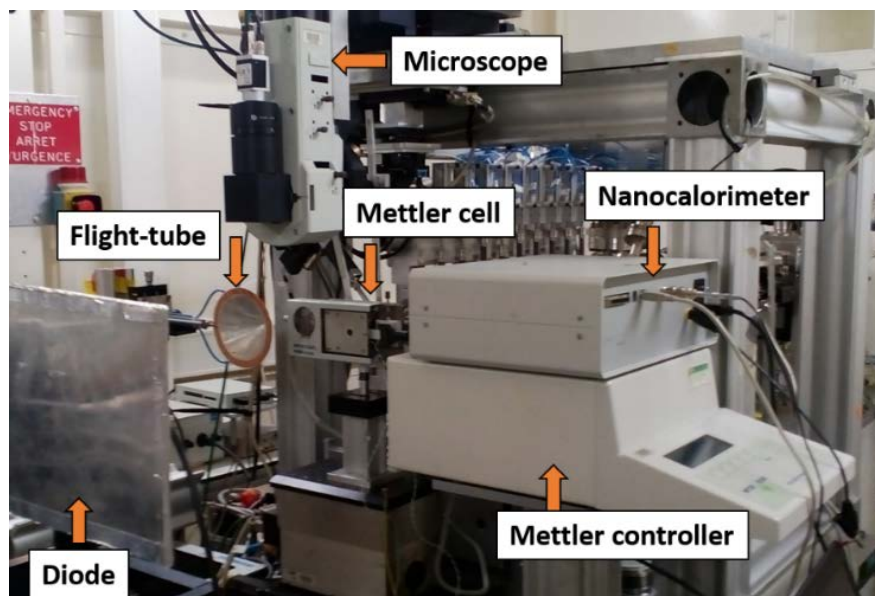


Figure 4.25 Overview of the setup combining in-situ fast chip calorimetry with X-ray micro-diffraction at the micro-branch of ID13, ESRF, using a Mettler heating stage as an external heater. The flight-tube with the beamstop is moved out when changing the sample.

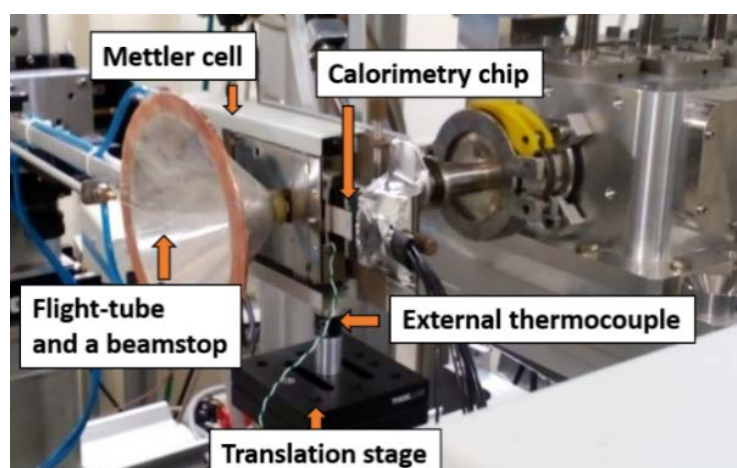


Figure 4.26 Side view for the setup combining in-situ fast chip calorimetry with X-ray micro-diffraction in a ready-to-measure state at the micro-branch of ID13, ESRF

The high flux at the micro-branch of ID13 with up to 2.7×10^{12} photons per second at 13 keV in combination with a micro-sized beam allowed to perform fast diffraction measurements of micron-sized polymer samples of PEEK during heating with heating rates up to 4000 K/s. In order to collect the scattering intensity from the maximum sample surface and possibly reduce radiation damage a diverged beam with the lateral size of 15 micron was used in the experiments (defocus operation). The illumination scheme used to achieve this beam size using the transfocator setup is explained in the following section.

In all conducted experiments the energy of the X-ray photons was set to 13 keV. 2D diffraction data were collected using the beamline's Eiger X 4M detector with millisecond acquisition times. The norm of the scattering vector s ($|s| = 2 \sin(\theta) / \lambda$, where θ is the Bragg angle and λ is a wavelength) was calibrated in the small and wide angle regions using several diffraction orders of silver behenate and corundum, respectively.

The Collimation scheme and adjustment of the beam size

Focusing of the X-ray beam down to a spot of $1.5 \times 3 \mu\text{m}^2$ is realized by the sets of beryllium compound refractive lenses of the transfocator. In order to efficiently collect the scattered intensity the transfocator was moved upstream. This allowed moving the beam focus upstream and placing the sample in the divergent part of the beam. Such adjustment of the beamsizes resulted in a beam footprint on the sample of about 15-20 μm along both directions. In order to clean the X-ray signal from parasitic scattering, a three-pinhole (“divergence slits”) collimation scheme was applied (Figure 4.27). The sample was placed several millimeters downstream the third pinhole. The parasitic scattering originating from interaction of beam “tails” with the first pinhole (S1) was stopped by a narrow aperture S2 and the last part of scattered intensity was removed by the third pinhole S3. It is worth mentioning that the pinholes neither cut the direct beam nor significantly change the beam profile and were used only for removing the parasitic scattering. The arrangement allows to obtain a very low background.

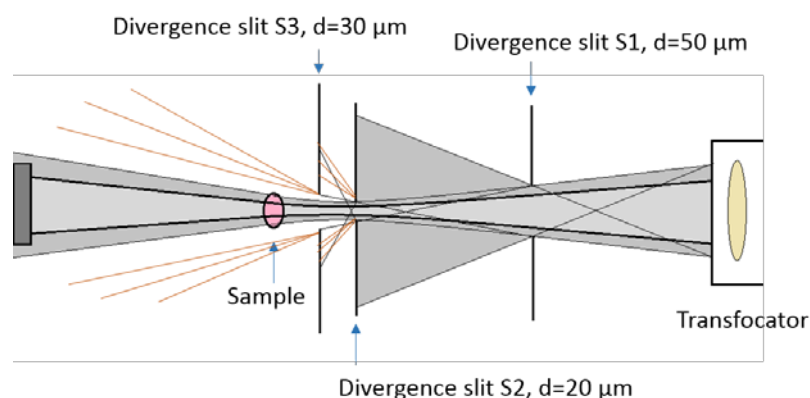


Figure 4.27 Collimation scheme. Orange lines schematically demonstrate diffracted intensity from the slits, the dark grey beam section indicates parasitic scattering, the bright grey area represents the usable part of the beam without any parasitic scattering

In order to avoid illuminating the detector with the direct beam a beamstop being a lead wire with a diameter of about 500 μm fixed at the end of a thin glass capillary was placed downstream the sample and at a distance of less than 200 μm downstream the exit window of the helium flight-tube made from a 4 μm thick polypropylene foil. The close position of the beamstop to the polypropylene foils is required to stop all scattered signal of the foil of the flight-tube exit window within a cone of 45 degrees half opening angle.

Synchronization and triggering

In order to synchronize the fast heating process during the in-situ nanocalorimetric measurements a trigger scheme based on TTL signals and a signal multiplexer (a NIM device called “OPIOM”, a generic internal development at the ESRF) was designed and implemented at the beamline. To solve this problem, several possibilities were considered. The first option would be to statically define the calorimeter as the master of the triggering scheme. However, in-between fast heating runs the sample needs to be aligned and the setup has to be checked interactively using diode and detector feedback, which requires to have the standard trigger scheme of the beamline active. The solution was to reprogram the OPIOM device dynamically using the beamline control software, "SPEC", in such a way, that the fast beam shutter and the detector acquisition was triggered by the P201 counter/timer device (a ESRF standard device) or the nanocalorimeter for standard alignment applications or fast heating experiments in burst mode, respectively. The block chart of the dynamically switchable trigger scheme is given in Figure 4.28.

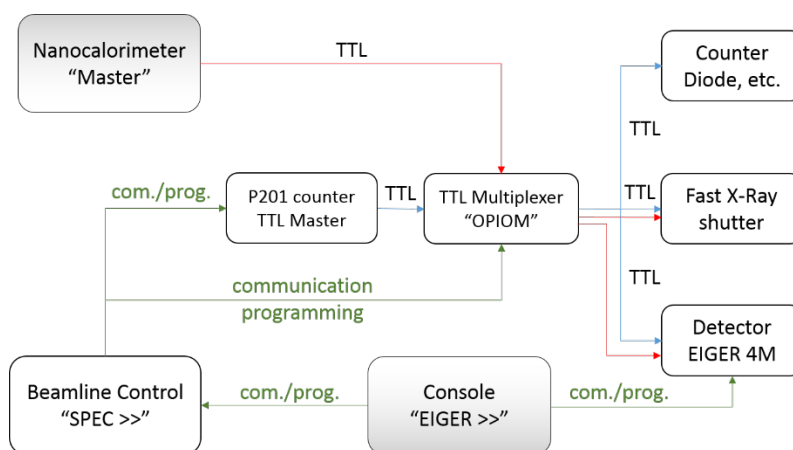


Figure 4.28 Block diagram describing the configuration of the triggering system

Due to problems and delays concerning the implementation of the Eiger 4M detector into the general beamline control software "SPEC" a specialized control program was developed by beamline staff. It allows to control the general beamline features and the Eiger 4M detector independently from SPEC from an additional "EIGER" console. This control program became standard at ID13 offering a higher flexibility for asynchronous operation and complex data acquisition procedures. The simplicity and high reliability of the scheme was due to the fact that the Eiger 4M detector was operated in "external trigger mode", which means that each acquisition of the pre-programmed detector was triggered by an external trigger pulse.

When the beamline operates in default mode as it is done for alignment scans and conventional raster scans, the Eiger 4M detector was programmed and armed from the EIGER console while simultaneously the SPEC console was instructed in remote mode to launch the scans together with the according trigger sequences via the P201 counter device (see green arrows in Figure 4.28). The TTL signal generated by the counter device was then multiplexed to serve all the equipment requiring timing, e.g. counter devices like diodes and ion chambers, the fast X-ray shutter and the detectors used as shown by the blue arrows.

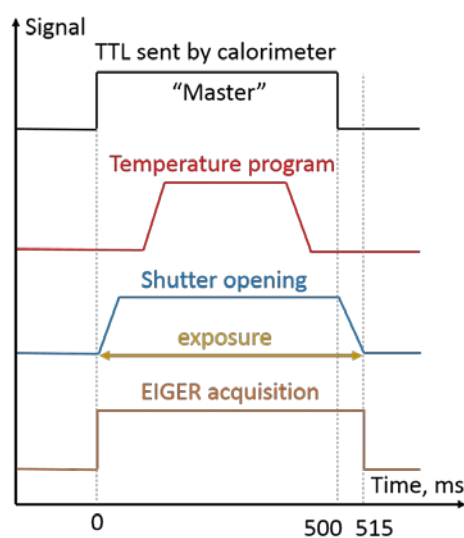


Figure 4.29 Scheme of experiment with usage of the triggering system

To launch a combined run in the burst mode the calorimeter and the detector has to be programmed with the according heating profile and the acquisition scheme, respectively. When the nanocalorimeter starts his temperature program a TTL signal is generated and sent to the multiplexer controlling the acquisition of the X-ray detector as well as the opening of the fast shutter (Figure 4.28) instead of the P201 time/counter device. The detector, armed by the EIGER control client prior to the launch, starts its pre-programmed acquisition scheme when the rising edge of the signal is detected. The number of frames the detector will collect is defined by the duration of the experiment and the counting time plus an additional readout time of $10\ \mu\text{s}$ for every frame. To ensure that all photons are counted during the exposure a 15 ms extra time is added to the experiment allowing collecting data while the shutter is closing. After the temperature program from the nanocalorimeter is finished the TTL signal drops to zero forcing the shutter to close.

It is advisable to design the temperature program in a way to ensure that the sample stays at the starting temperature in a first time period, e.g. 50 ms, in order to wait until the shutter is completely opened (c.f. Figure 4.29).

4.2.3 Analysis of two dimensional X-ray diffraction data

X-ray diffraction data were collected in a form of 2D images containing information on the distribution of the scattering intensity in a section of the reciprocal space. Since in this project the sample is considered to reflect an ideal powder distribution the 2D images were integrated over the azimuth using the py-FAI package developed by the ESRF^{153,154,155} to generate one dimensional diffraction curves. Further analysis, such as background correction and peak fitting, was done using home-built routines designed within the Igor Pro software package (Wavemetrics Ltd.)

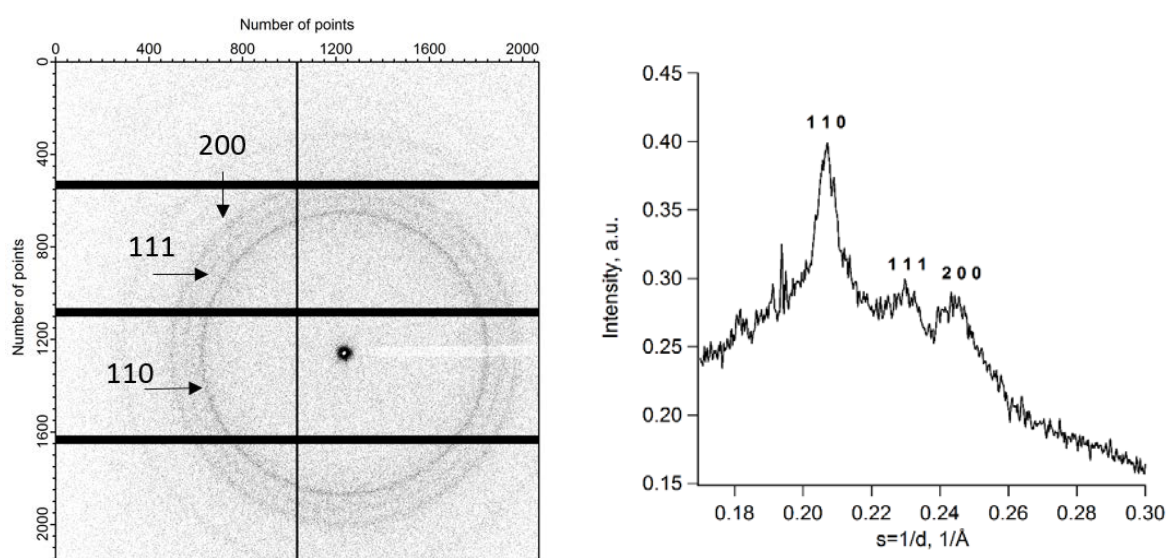


Figure 4.30 Raw image corresponding to 2D diffraction pattern of PEEK with the acquisition time of 2 ms (left), 1D-reduced diffraction pattern after azimuthal integration of one frame (right)

A typical powder pattern of PEEK, as recorded during a fast heating experiment, is shown in Figure 4.30 (left) using a gray scale color code. The three main diffraction peaks typical for a PEEK pattern are indicated. The black straight lines represent the gaps between the detector modules where no scattering intensity can be detected. These gaps have to be accounted for during the integration procedure by applying a mask file that contains information which pixels of the image contain information and which pixels have to be ignored. A typical 1D-reduced PEEK pattern is shown in Figure 4.30 (right). As can be seen, the signal to noise ratio is not very high which is due to the ultra-short counting times during the fast heating experiments. However, in most of the cases the required information on the crystal lattice parameters needed in the frame of this work could be safely extracted by applying proper fitting algorithms.

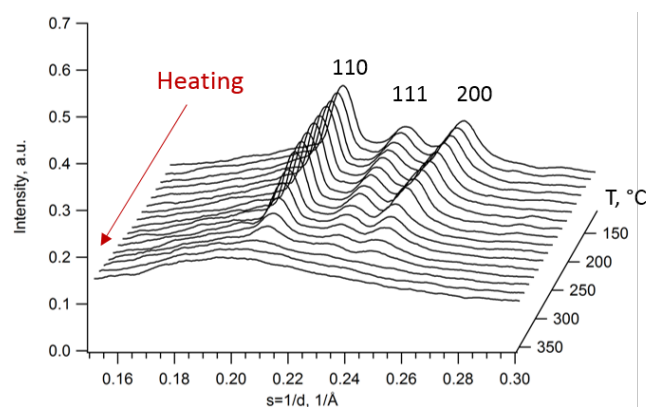


Figure 4.31 Composed waterfall plot of 1D-reduced diffracted patterns corresponding to one heating experiment

A sequence of several diffraction patterns as recorded during a fast heating experiment is shown in Figure 4.33 in the form of a waterfall plot. The time sequence for the displayed heating run is indicated by a red arrow. The melting event can be readily recognized just by visual inspection of the plot. The peak fitting algorithms used to analyze the melting process are discussed in the next section.

4.2.4 Peak fitting algorithms used for analysis of diffraction data

PEEK is known to crystallize in a semicrystalline structure which contains thin crystalline lamellae interlayered with slightly thicker amorphous gaps indicating a general crystallinity of less than 50%, a typical value for the group of semirigid chain polymers. As a result, both, crystalline reflections and a broad halo from amorphous phase appear in the X-ray diffraction pattern.

When analyzing an experimental dataset it appears difficult to directly separate the single contributions to the overall pattern, e.g. parasitic scattering, amorphous halo, crystal reflections, etc. The approach chosen for the analysis of the PEEK data is to model all the contributions with analytical functions and to subsequently fit the sum of all contributions simultaneously for every single diffraction curve.

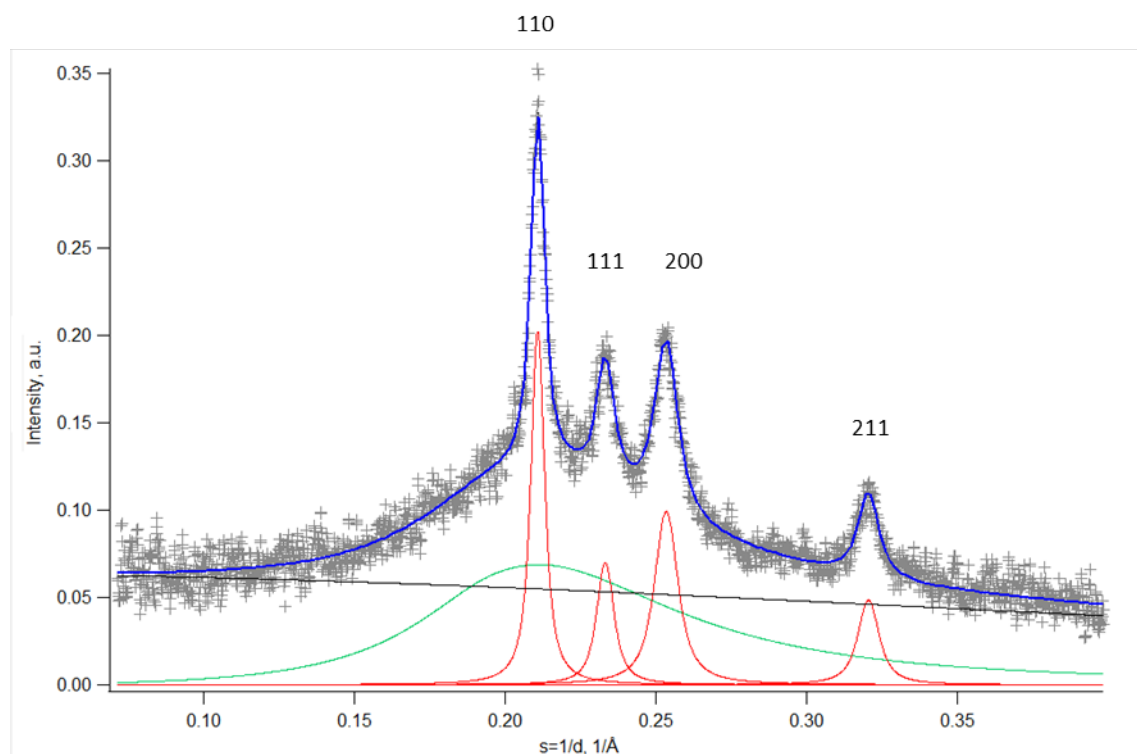


Figure 4.32 1D-reduced X-ray diffraction pattern fitted with a combination of a series of pseudo-Voigt functions to describe the crystallographic reflections (red), a broad pseudo-Voigt function centered at $s = 0 \text{ 1/Å}$ to account for the air scattering background (black) and two half wings of Pearson-VII functions splined at their maxima to describe the asymmetric amorphous halo (green). The sum of all the mentioned contributions is shown in blue reflecting the experimental data point (grey).

In a simple approach, the diffraction peaks experimentally recorded are, amongst others, a convolution of scattering from the crystal and the beam profile. Without having the possibility to apply a straightforward deconvolution of the different peak contributions, the pseudo-Voigt function was applied to describe the shapes of the diffraction peaks in the experiments. This also stems from the fact that the profile of the primary beam in the focal point is best described using a pseudo-Voigt function (see Figure 4.32 red curves).

For the description of the amorphous halo two half wings of Pearson VII type functions, connected at their maxima were used to account for the asymmetry of the halo. For the description of the remaining air scattering background a broad pseudo-Voigt distribution function was used centered around $1/d = 0$ (see Figure 4.32 black curves). The sum of all the contributions is shown in blue and nicely matches the experimental scattering pattern given in gray. From the parameters of the particular distribution functions the peak position and intensity as well as the peak width at half maximum could be derived. The peak intensity of a

particular crystallographic reflection is defined as the integral of the distribution function and corresponds to the area under the peak.

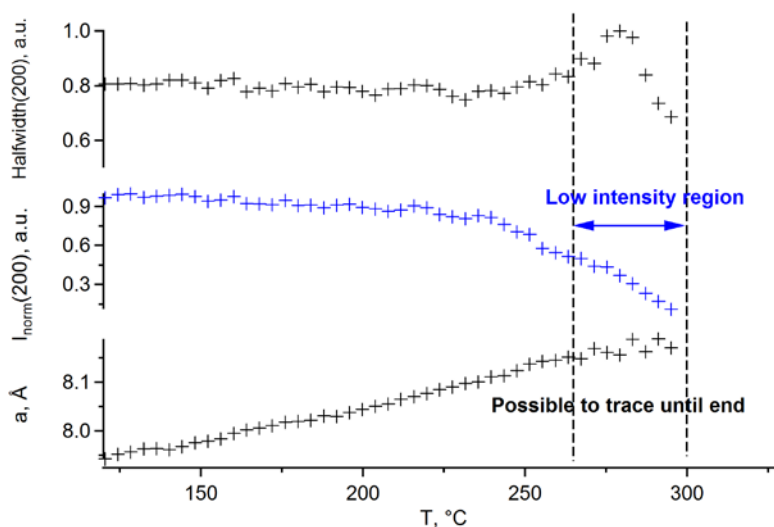


Figure 4.33 The a -parameter, full width at half maximum (FWHM) and peak intensity of 200 PEEK reflection peak plotted as a function of temperature. With the fitting procedure described above, it is possible to trace the peak positions until the end of heating even in the regions of low diffracted intensity

The two main parameters of the 200 of PEEK diffraction peak derived from the fit parameters for a heating sequence from 110 to 400 °C are shown in Figure 4.33. The main advantage of the fitting procedure described above is that it is possible to trace the diffraction peak positions until the end of heating even in the regions where, due to partial melting, the diffracted intensity becomes faint. The last part of the a -parameter curve evolving with temperature (in the temperature region just before the final melting) is crucial for the current research. This will be discussed in the section dedicated to the analysis of the results.

4.2.5 Challenges

Philosophy of time-resolved measurements

Time-resolved X-ray diffraction experiments can be successfully performed at synchrotron sources with time resolution less than several picoseconds. Employing the “pump-and-probe” technique, an ultra-short and intense laser pulse excites the sample and another pulse, i.e. optical pulse or X-ray synchrotron beam pulse, needs to obtain information about this excited state. This technique enables to study ultrafast phenomena in matter. By using suitable fast

detectors or by employing stroboscopic recording schemes, the temporal resolution of these experiments is only limited to the duration of the optical pulses.¹⁵⁶ Using the latter approach time resolution of up to 100 ps can be achieved at ID09, ESRF.¹⁵⁷ Therefore, a mechanical chopper system is employed to select single pulses coming from the synchrotron with a repetition rate matching that of the laser that induces the excitement of the material. Simultaneously, the sample under investigation, being kept in solution or suspension, ejected by a jet at the position where the two beams overlap. Thus for every pulse a new portion of the sample is available. Since the chopper does expose the sample only in a particular moment of interest of the sample response the "slow" integrating detector will only see photons at the desired moment. Thus the time resolution is not defined by the framerate of the detector, but by the timing of the chopper. Though, extremely high time resolutions are achievable using this technique, the application of this method is only possible for processes that are repetitive and reversible, or where at any moment a newly conditioned sample can be provided using fly-by methods such as liquid- and viscose jets or droplet generators.

Another approach was implemented by *Baeten et al.*¹⁴⁸ to combine fast scanning calorimetry with in-situ WAXD analysis to study isothermal crystallization of high-density polyethylene (HDPE) and polyamide 11 (PA11) as well as cooling and heating experiments performed in multiple identical runs. As nanocalorimetry sensors the MultiStar UFSI MEMS chip sensors from Mettler–Toledo were used by developing a small X-ray accessible holder for the standard Flash DSC1. Simultaneous WAXD analysis was performed using an X-ray beam of 160 x 170 μm^2 at BM26, ESRF. To achieve the temperature resolution of 2 K/frame during a heating scan with 200 K/s an acquisition times of 17 ms were used. To achieve good counting statistics the measurements were repeated up to 60 times allowing the sample to recrystallize prior to each heating run. Thus the total acquisition time was about 0.5 to 1 s for each temperature point.

Scattering intensity vs heating rate and radiation damage

Both approaches described above cannot be easily applicable in the study of fast structural transitions in PEEK by combination of nanocalorimetry with X-ray micro-diffraction utilizing the heating rates higher than 200-500 K/s because of the several restrictions discussed here and in the following sections.

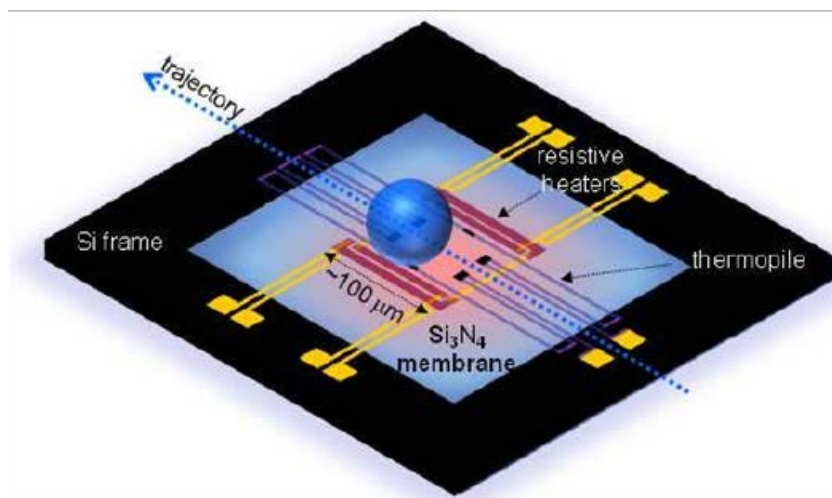


Figure 4.34 Graceffa et al.¹⁵⁸. Schema of nanocalorimetry chip with a ballistic droplet evolving close to the membrane being continuously heated along its trajectory across the heated zone.

Applying the stroboscopic approach with a constant delivery of new samples could potentially solve the conflict between the demanded high heating rates and radiation damage. The stroboscopic method in terms of multiple chips with new samples operating in a sequence cannot be realized in a given configuration of the nanocalorimeter because the current version of the nanocalorimeter can work in every moment of time with only one calorimetric chip. However, if the delivery of the samples would be implemented in the way of continuous supply of fresh material in series of microparticles propelled close to the membrane being continuously heated along as discussed by Graceffa et al.¹⁵⁸ and as shown in Figure 4.34, the stroboscopic approach could be possibly realized with the existing version of the nanocalorimeter.

Compromises: preparation, time resolution and beam damage

In the current work, it was necessary to load calorimetric chip with a new sample for each experiment. The reason that the sample cannot be reused in any further experiments is the fact that after the beam exposure for only 1 second the sample was severely damaged and did not recrystallize properly. In addition, the crystallization of the sample on the chip before each successive experiment would require at least 30-40 min, which would waste a substantial part of the available beamtime.

In the experiments, the acquisition time was chosen in a way to minimize the extent of radiation damage. Thus for each particular measurement the duration of acquisition was chosen as a compromise between maximization of the scattering intensity per 1 frame while minimizing the radiation damage imposed. In addition, the temperature resolution had to be chosen in a meaning full way that a reasonable temperature resolution was achieved. Thus, for experiments utilizing high heating rates, e.g. from 2000 to 5000 K/s, the minimum frame time of 1.34 ms offered by the Eiger 4M detector was resulting in a temperature resolution of 2.68 K/frame in the case of 2000 K/s and 6.7 K/frame in the case of 5000 K/s.

Since the conduction of one heating experiment consumed one calorimetric chip with one prepared sample the total number of samples which could be measured in a given beam time was limited. In addition, the sample preparation methodology for PEEK droplet preparation was done manually. Thus, the samples differed slightly in size, and thus, mass, as well as in placement on the chip. This explains that measurements are not fully coinciding, and questionable measurements had to be repeated with substantial effort in preparation time as well as in beamtime, being one of the main limiting factors.

Technical limits of the used Nanocalorimeter

One of the limitations for conducting systematic experiments when it came to slow heating rates was the fact that the Nanocalorimeter has a limit for the duration of a fast heating experiment of maximum 10 s. That means that a standard fast heating program (DC mode) using 50 ms of isotherms within the program, e.g. before the heating, at the highest temperature and after cooling, cannot utilize heating rates smaller than 35 K/s (cf. Figure 4.35) when working with PEEK.

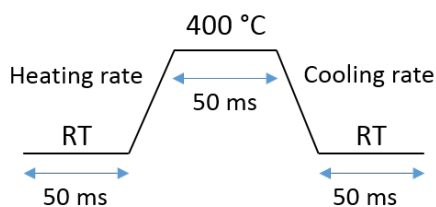


Figure 4.35 Standard thermal program for working in the fast mode of Nanocalorimeter

Accordingly, measurements using smaller heating rates had to be done in temperature modulation (AC mode). The main disadvantage, when using the AC mode, is that only the change of the heat capacity can be observed from the calorimetric curves. Moreover, the software of the calorimeter does not allow combining the isothermal crystallization of the sample with the subsequent heating run starting at the crystallization temperature without quenching the sample to room temperature. This is a technical issue, which will be changed in the next generations of the device. However, for the conduction of the project here it was limiting the possibility to explore the effect of short quenching to RT prior to the fast heating run.

Another complication stems from the way the higher temperatures were reached using the secondary heater to provide a temperature offset. The offset temperature is applied already at the very beginning of the leading isotherm meaning that the sample is annealed for 50 ms at 110 °C prior to the heating process. Even though, the T_g of PEEK is in the range of 140 °C to 150 °C it is difficult to exclude the impact on the heating and recrystallization per se, since it can result in some structural modifications in the polymer.

Radiation damage

Micro-diffraction measurements of PEEK samples were performed at ID13 with the setup described in detail above in the current Chapter. The radiation damage of PEEK samples was observed visually on the optical microscope images as dark spots propagating in the area of beam footprint after exposure of the sample during several seconds (Figure 4.36). The damaged spot is larger than the beam size which indicates on propagation of beam-induced damage in the sample.

Differences in PEEK thermal behavior were found when experimental data obtained at BM26 and ID13 were compared. As it is shown on Figure 4.37 (left), the a -parameter of PEEK lattice plotted as a function of temperature in the case of measurements performed at BM26 using a macroscopic PEEK sample and a millimeter-sized beam has a characteristic drop in the end of the heating, which is identified as the structural signature for the recrystallization of PEEK (see chapter 5.2.1). In contrast, when a comparable experiment is conducted at ID13 (slow heating and continuous exposure with the high flux density beam) the recrystallization event could not be observed. This can be explained by induced radiation damage mostly in the amorphous phase of the material, which impedes the recrystallizability of the polymer.

The exact nature of the radiation damage and its implications on the molecular structure are still in debate. However, radiation induced crosslinking and bond breaking of the polymer backbone are most probable candidates to explain the suppressed crystallizability.

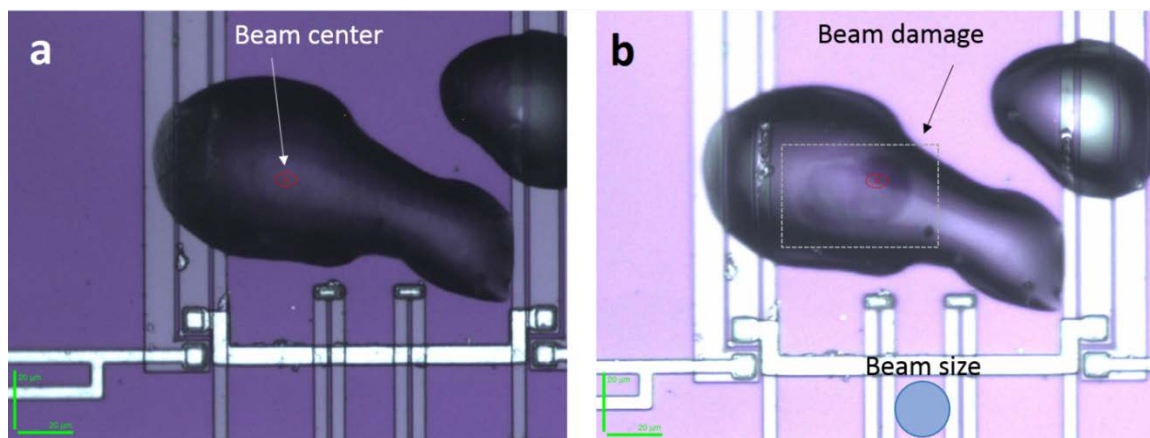


Figure 4.36 Optical microscopy images of a non-exposed PEEK sample (left) and the same PEEK sample after exposure with a flux of 2.7×10^{12} ph/s @ 13 keV for 740 ms (right). Dark spot indicates the damaged zone. The size of the beam is shown schematically with a blue circle.

In order to overcome the restrictions and be able to perform slow heating measurements at ID13, it was decided to switch on the X-ray beam only at the end of the heating with a hope to catch the last moments of the heating and not to damage the material before the interesting temperature region is reached. Such manual starting of exposure did not allow to apply the usual synchronization scheme. However, it was still possible to perform an experiment because of the slow heating and large time between frames. As a result the drop of the α -parameter was indeed observed during slow heating at ID13 as it was at BM26 (Figure 4.37, right).

The observations considering the larger effect of radiation on the amorphous phase of PEEK are in agreement with data obtained by *Sasuga* and *Hagiwara*¹⁵⁹. The authors studied the influence of ionizing radiation on PEEK samples and observed that PEEK preserves its crystalline structure upon radiation exposure at moderate levels (~ 50 MGy). The radiation-induced degradation process in PEEK which is supposedly crosslinking occurs near lamellar surfaces and results in reduction of the average crystal thickness of 15%.¹⁶⁰ In this respect, there is a difference between the semi-rigid chain and flexible-chain polymers. As studied by *Keller* et al.^{26,161} exposure of PE with ionizing radiation results in bond scission and

formation of crosslinks. All these effects lead to destruction of the crystalline structure of PE with an expended dose of 30 MGy.

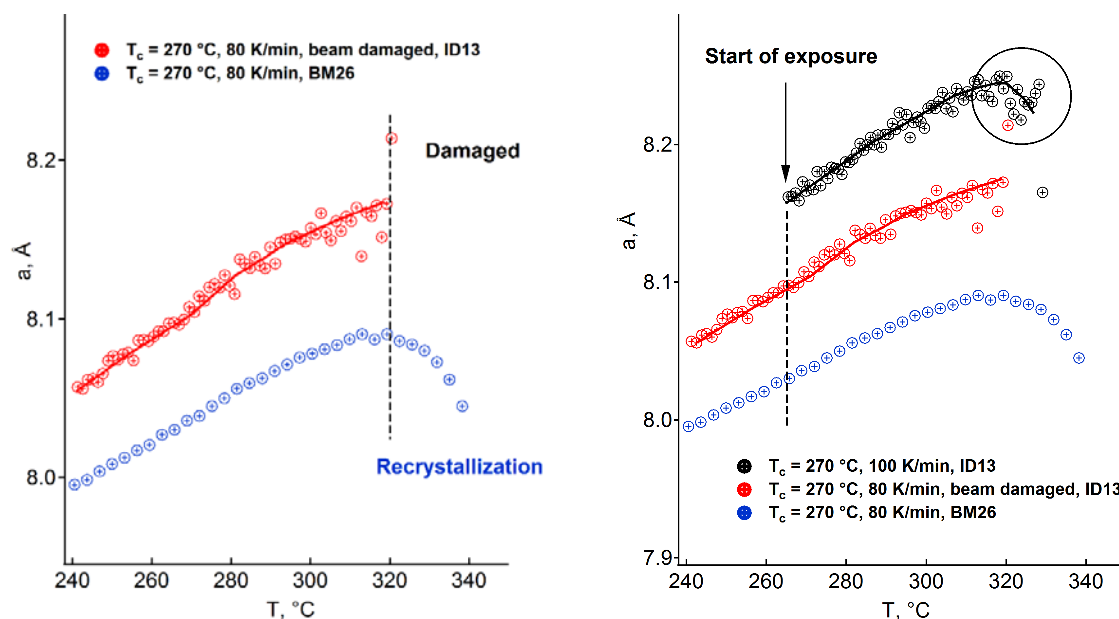


Figure 4.37 Left - a -parameters plotted as a function of temperature for the case of heating at a rate of 80 K/min during X-ray diffraction measurements with a millimeter-sized beam at BM26 (blue curve) and a micro-beam at ID13 (red curve). Both samples were exposed during of the whole heating ramp. The damaged sample (red curve) does not exhibit a drop of a -parameter before the final melting compared to the non-damaged sample (blue curve). Right - sample measured at ID13 was started to be exposed by X-ray beam only at 265 °C which led to appearance of the characteristic drop of a -parameter before the final melting. The curves are plotted with a vertical offset with respect to the blue curve for clarity.

However, there is a different situation for amorphous PEEK compared to crystallized samples. The glassy PEEK irradiated at 50 MGy as was shown by *Yoda*¹⁶⁰ is incapable of crystallization because of formation of defect structures which prevent the structure from molecular reorganization on heating. An important finding of *Vaughan* and *Stevens*^{145,146}, who studied radiation damage of PEEK samples with DSC analysis, was that irradiation mainly affects the amorphous regions reducing crystallization and recrystallization rates, which is assumed to be caused by crosslinks within the amorphous regions. The effect of irradiation of lamellae is much smaller than that of the amorphous regions. However, large radiation doses may result in crystallinity loss with little changes in morphology. This result can be explained by different chain mobility in the crystalline and amorphous regions because a certain molecular motion is required for chain scission and crosslinking. *Sasuga* and *Hagiwara*¹⁵⁹ also stressed a large impact of radiation damage on PEEK which brought about disintegration of tie molecules between crystalline and amorphous phases.

To conclude, the radiation mainly affects the amorphous regions of PEEK and tie molecules between crystalline and amorphous phases which reduces the ability of the material to recrystallize (or to crystallize). In the experiments shown on Figure 4.37, the ability of recrystallization was lost for samples exposed by micro-beam at ID13 during slow heating measurements. The crystalline structure was preserved until 320 °C but no drop of the α -parameter was observed before the final melting which was identified before as the signature of recrystallization. In further experiments, the X-ray beam was switched on only at ~265 °C which prevented the system from overexposure and allowed the material to recrystallize. As a result, a delayed exposure let us performing slow heating measurements at ID13 and concluding that no real difference in the thermal behavior between microscopic and macroscopic PEEK samples was observed.

5 Calorimetry vs X-ray micro-diffraction to address the recrystallization phenomenon in PEEK

In this chapter, the results on recrystallization of isothermally crystallized PEEK during heating, accessed by nanocalorimetry and its combination with millisecond time resolved X-ray micro-diffraction, are presented and discussed.

In a first approach, it will be shown what information and conclusions can be obtained from calorimetry and fast chip calorimetry alone. Furthermore, the limits of this single-technique-based approach will be demonstrated. In this context, some surprising findings on the critical heating rates and their implication on the interpretation of calorimetric data will be discussed in some detail.

In the second part, the results obtained with a combined in-situ approach providing real time information on the structural evolution during fast heating will be presented. It will be discussed in what respect these pieces of information are essential for a more fundamental understanding of the processes involved and what they can add to the picture.

By presenting the findings from a combined approach coupling fast chip calorimetry with millisecond time resolved X-ray micro-diffraction the structural signature of the recrystallization process in PEEK during heating will be discussed. The experiments using slow heating with in-situ WAXS analysis were used to cover a wider range of heating rates and to have a possibility to compare the structural transitions at high heating rates to those at rates more common for the classical DSC analysis. Based on this information the recrystallization diagram from PEEK will be established showing under what condition the recrystallization will take place during heating. This will allow understanding the thermal signature of PEEK in general and will help to comprehend contradictory results reported in the literature.

As a small outlook, an additional approach is presented to study the isothermal recrystallization of PEEK by jumping into the beginning of the final melting region of PEEK. The evolution of the lattice parameters is followed while the sample is recrystallizing. The time evolution of the lattice provides the characteristic time of the recrystallization process.

5.1 The double-melting of PEEK accessed by nanocalorimetry

In the first section of this chapter, the results obtained on the thermal behavior of PEEK solely by nanocalorimetry and conventional DSC will be presented and discussed. Generally, two different approaches will be addressed. The first one is focused on understanding the double melting behavior of PEEK. In this context, the evolution of the thermal transition temperatures will be studied as a function of the crystallization temperature and heating rates. Therefore, simple heating experiments were performed using the described home-built nanocalorimeter in the range of 50 to 5000 K/s. For the sake of completeness, standard DSC measurements were added to the dataset and correlated with the results from fast chip calorimetry.

In a second approach, the premise of a secondary inter-lamellar crystallization process, taking place time-wise delayed with respect to primary crystallization process, will be tested using an interrupted crystallization process followed by fast heating calorimetry. The main idea is that with this approach experimental conditions may be found where only the primary crystals are present and, thus, their melting signature can be identified.

5.1.1 Thermal programs and nanocalorimetric data analysis

In order to clearly understand the experimental results presented in this section, the experimental protocols of the two calorimetric approaches are summarized below.

Nanocalorimetry used for fast heating experiments of isothermally crystallized PEEK

The thermal program used for the isothermal crystallization is shown in Figure 5.1 (left). For the described experiments a Mettler Toledo FP82HT hot stage was used to provide a temperature offset. The temperature offset was set to $T_{\text{base}} = 80\text{ }^{\circ}\text{C}$ for two main reasons. The first reason is that an $80\text{ }^{\circ}\text{C}$ offset was sufficient to push the maximum reachable temperatures of the calorimeter to $400\text{ }^{\circ}\text{C}$, while it was about $60\text{ }^{\circ}\text{C}$ below the T_g of PEEK to ensure that no excessive annealing takes place between the crystallization of the material and the subsequent fast heating experiments.

After deposition of a micron-sized PEEK particle in the center of the active area of the sensor chip it was heated to $400\text{ }^{\circ}\text{C}$ to induce melting of the polymer and the formation of a stable

micro droplet in the center of the chip. The procedures for the accurate placement of the micro-droplet are described in Chapter 4.1.8. Before each individual nanocalorimetric measurement the sample was heated to 400 °C for 2 seconds to ensure complete removal of the previous thermal history. The samples were crystallized at different temperatures in the range between 170 and 300 °C for 30 minutes before the sample was cooled down to the environmental temperature T_{base} of 80 °C.

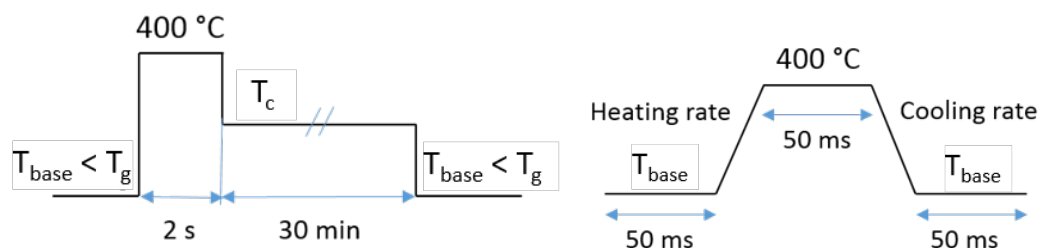


Figure 5.1 (left) thermal program used for sample crystallization; (right) thermal program used for nanocalorimetric measurements.

In the right part of Figure 5.1, the typical temperature program for a nanocalorimetric run is shown. The main features beside the heating and cooling segments are the 50 ms-long isotherms at the beginning and end of the experiment as well as the maximum temperature. These isotherms are added to allow the nanocalorimeter reaching the stable conditions before the next segment is started. Also, since this device is a simple heat-flux calorimeter, the loaded sample run will always lag behind the reference measurement conducted prior to the actual measurements using the very same chip. The added isotherm after the heating and cooling segments, therefore, allow the device reaching the set temperature.

Using the same chip as the reference, i.e. empty cell, the measurements in the same conditions allow precisely calculating the temperature offset between the loaded and reference measurement needed for the correct estimation of the melting peak onsets. The heating rates used with this experimental setup ranged from 50 to 5000 K/s. For the sake of simplicity, the cooling rate was chosen to be identical to the heating rate.

DSC measurements

DSC measurements were performed at IS2M, CNRS, Mulhouse, using a Mettler Toledo DSC1 at a power and temperature resolution of 0.04 μ W and 0.2 K, respectively. The device operates in a nitrogen atmosphere in the temperature range from -150 to 700 °C with a

maximum heating rate of 80 K/min. The samples which were previously isothermally crystallized using a Linkam heating stage, were weighed and placed in aluminum DSC crucibles to perform heating scans at heating rates ranging from 5 to 80 K/min. To ensure the comparability of the DSC data with the nanocalorimetric data, the onset temperatures of the melting peaks were used in the analysis.

PEEK sample

PEEK sample used in this work was a commercial powder specimen ICI 150P with $M_n=10300$ and $M_w = 26800$.

Interrupted crystallization of PEEK studied by nanocalorimetry

For the experiments applying interrupted crystallization the isothermal crystallization time was varied from 1 up to 5400 s (c.f. Figure 5.1 and Figure 5.2). It is important to note at this stage that in-between the interrupted crystallization and subsequent heating run the sample was quenched to the base temperature of 80 °C and held there for a short period of time on the order of several seconds. This quenching in-between the conditioning of the sample and heating is due to the inability of the nanocalorimeter to combine the slow heating mode with fast heating burst mode. The thermal program for these measurements is summarized below for clarity.

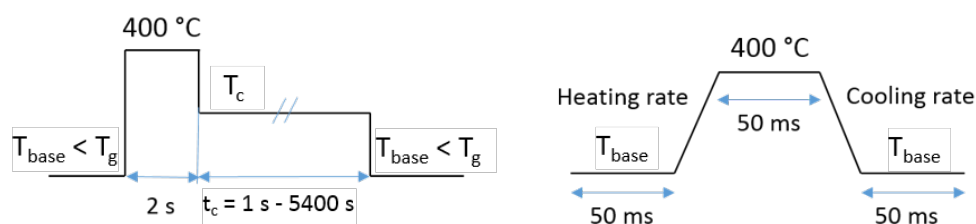


Figure 5.2 Thermal program for the experiment with interrupted crystallization

The thermal program contains two parts: melting of the micron-sized PEEK micro-droplets to erase the thermal history at 400°C followed by a quick jump to the isothermal crystallization temperature where the sample was crystallized for different times and subsequently quenched to the base temperature. The subsequent heating runs of the preconditioned sample followed the previously described protocols for fast heating measurements, cf. Figure 5.2 (right).

Selection of the onset temperatures from nanocalorimetric and calorimetric curves

For the reasons explained in chapter 4.1 in detail the onset temperatures of the melt transitions, T_m^{on} , are used as characteristic temperatures throughout this work rather than the "peak" temperatures. The onset of the melting transitions at T_m^{on} will be handled similarly to the traditional term "melting temperature" as described in section 4.1.5 (cf. Figure 4.14). This seems to be justified, since the melting line, being the slope following the melting peak onset, corresponds to an iso-temperature line in a nanocalorimetric experiment, while the peak value marks the end of the melting process rather than the point of the maximum conversion rate.

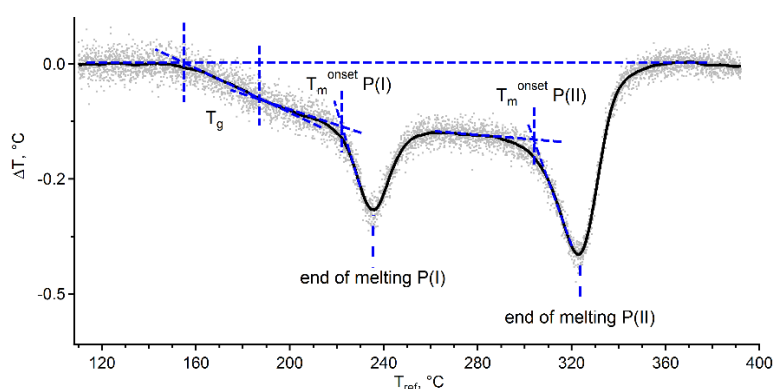


Figure 5.3 A characteristic nanocalorimetric curve. The deviation from the reference, or empty cell, temperature, ΔT , is plotted as function of the reference temperature T_{ref} .

In Figure 5.3 an example of a nanocalorimetric curve of PEEK is shown in black. The blue dashed lines added to the curve mark linear extrapolations to help identifying relevant temperatures from the curves. In order to identify the glass transition T_g region, linear baselines before and after the expected stepwise change are extrapolated. The intersection of the two base lines with a tangential extrapolation from the inflection point between the two extrapolated baselines in both directions mark the beginning and the end of the glass transition region. The onset temperature of the first melting peak is derived by the intersection of a linear extrapolation of the post T_g region baseline and the linear extrapolation of the iso-temperature line, the low temperature wing of the melting peak. The onset of the second melting temperature is done in a similar way. However, at high heating rates the two melting peaks start to merge making proper extrapolation towards the baseline of the measurement difficult. In order to be able to derive the second onset temperature, the local minimum (with respect to a negative ΔT) in-between the two melting peaks is used instead.

5.1.2 Slow DSC vs. fast chip calorimetry

In this section of the manuscript, the information on the double melting behavior of PEEK, gathered by DSC and fast chip calorimetry measurements is used to describe the evolution of the melting peaks behavior with respect to the crystallization behavior and the applied heating rates. The data are collected over the whole heating rate spectrum accessible by the used techniques covering over five orders of magnitude from below 0.1 K/s, e.g. 5 K/min, up to 5000 K/s. The collected datasets will be correlated with each other to derive a complete picture over the entire heating rate spectrum to allow drawing generalized conclusions.

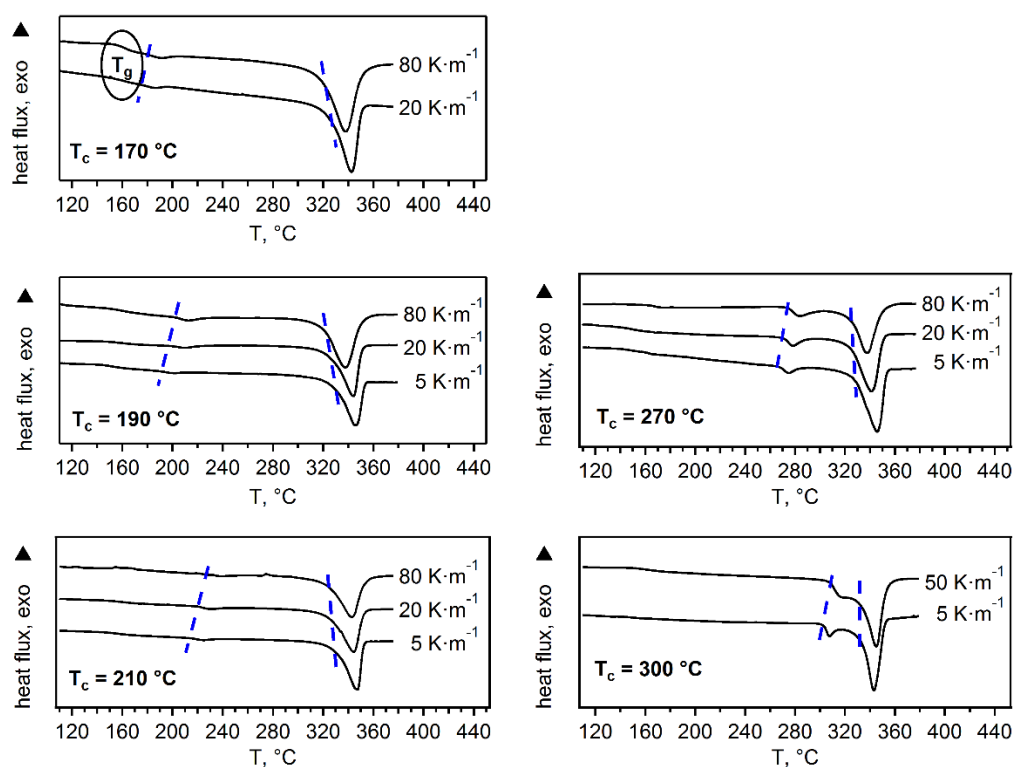
Conventional calorimetry measurements

Figure 5.4 DSC measurements conducted on milligram-sized samples of PEEK isothermally crystallized in the range from 170 to 300 °C. The applied heating rates are indicated on the graphs.

The onsets of the first and final melting peaks present in all the measured curves are summarized in Table 5.1 and Table 5.2, respectively. In agreement with the literature the onset of the first melting peak increases systematically with the crystallization temperature, while the onset of the final melting peak appears to be rather independent from T_c . In addition, the first melting temperature $T_mP(I)$ shows a slight increase with increasing heating

rate by about 20 °C from 5 to 80 K/s. Similar findings were reported as early as the 80s of the last century by *Lee* and *Porter*³⁹ for cold-crystallized PEEK using the peak value as characteristic temperature. In fact, their second finding that the final melting temperature decreases with increasing heating rate can be also identified from the curves shown here (cf. Figure 5.4). However, the effect is much less pronounced than in the referenced paper.

Fast chip calorimetric measurements

When it comes to fast chip calorimetry, the general picture looks very similar to the conventional DSC measurements at the first glance as can be seen from Figure 5.5, where the heating runs of PEEK, crystallized at the indicated temperatures, are shown for a heating rate of 500 K/s. At this point the reader is reminded that for the fast chip calorimetry measurements the local temperature difference between the sample and the empty cell measurements are plotted as a function of the empty cell reference temperature. Therefore, a negative ΔT , corresponds to a situation where an endothermic event, e.g. melting, takes place and the temperature lags behind the reference temperature. Also, it appears, that the first

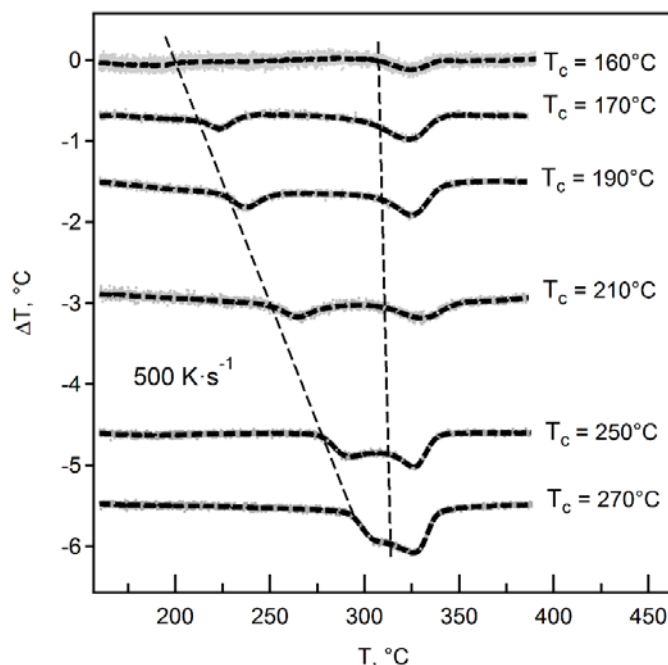


Figure 5.5 Nanocalorimetry curves of PEEK measured at 500 K/s after isothermal crystallization in the range from 160 to 270 °C. The curves are plotted with a vertical offset for clarity.

melting peak shifts to higher temperatures with increasing crystallization temperature as in the case for the slow heating experiments shown in Figure 5.4. Interestingly, and in contrast

to the first melting event, the second melting peak appears to be completely independent of the crystallization temperature.

In a first approach one could think that this could be due to the fact that the heating rate is still slow enough to allow the material to recrystallize in a continuous fashion, that the recrystallized crystals have all the identical thermodynamic stability and subsequently melt at the same temperature independently of the stability of the initially formed crystals. In order to check this premise, the effect of the heating rate has to be evaluated.

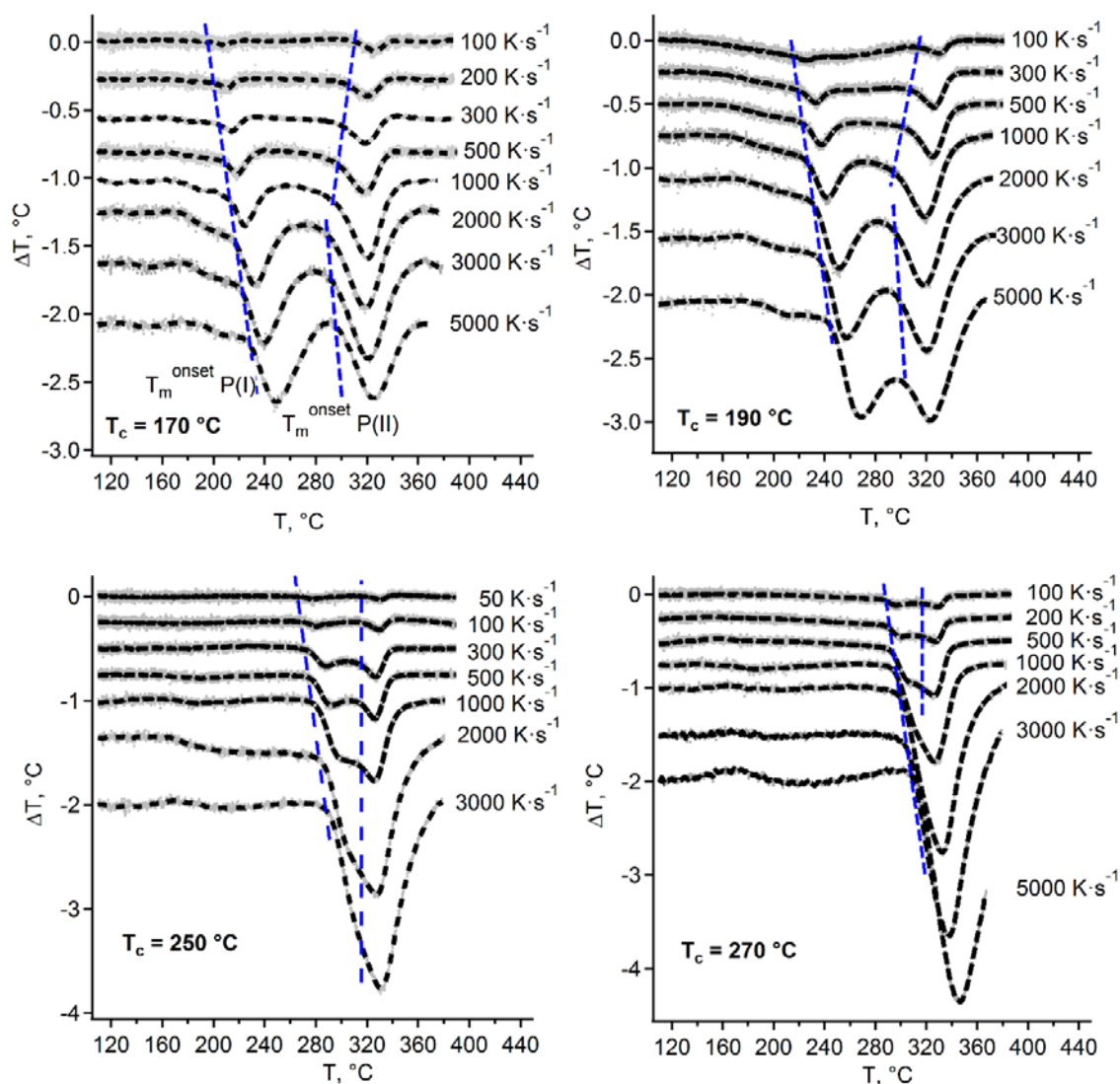


Figure 5.6 Nanocalorimetry curves for isothermally crystallized PEEK (170 °C - 270 °C) measured at heating rates from 50 to 5000 K/s before correction for the time lag. The isothermal crystallization temperatures and the applied heating rates are indicated on the graphs.

In Figure 5.6, a, complete dataset for the four different crystallization temperatures (i.e. 170 °C, 190 °C, 250 °C and 270 °C) heated with heating rates ranging from 50 K/s to 5000 K/s are presented. In order to get a better visual understanding of the positions of the particular onset temperatures for both peaks, blue lines are added to the graph. Following these lines, the picture becomes slightly less clear. The onset temperature for the first melting peak shows a clear dependence on the heating rate. This is somewhat puzzling, since one would not expect that the stability of the initially formed crystals depends on the heating rate so drastically that temperature drifts of up to 20 °C could manifest. In addition, it is suspicious that the slope of the increase appears to be identical for all crystallization temperatures, ranging for 170 °C, which is very close to the T_g , up to 270 °C, approaching slowly the higher end of the crystallization window. Moreover, the second melting peak shows a non-monotonic behavior for the two lower crystallization temperatures, i.e. 170 °C and 190 °C,

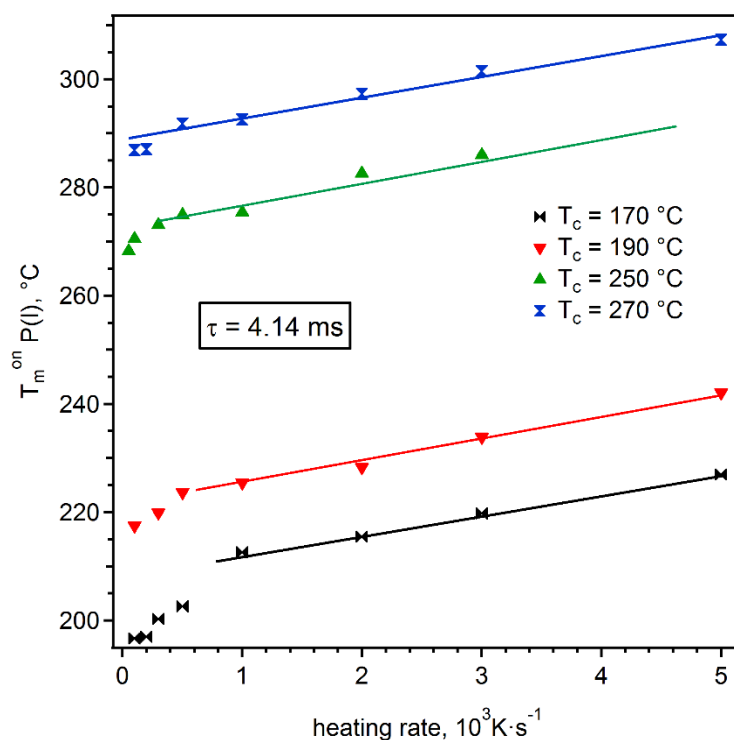


Figure 5.7 The low-temperature melting peak onset vs heating rate for PEEK samples crystallized at 170, 190, 250 and 270 °C.

where it first decreases with increasing heating rate and then starting from about 2000 K/s increases with increasing heating rate, while it shows no changes with heating rate for the higher crystallization temperatures, e.g. 250 °C and 270 °C. Trying to understand this

complicated behavior in detail the onsets of the first melting peak were plotted as function of the heating rate (c.f. Figure 5.7).

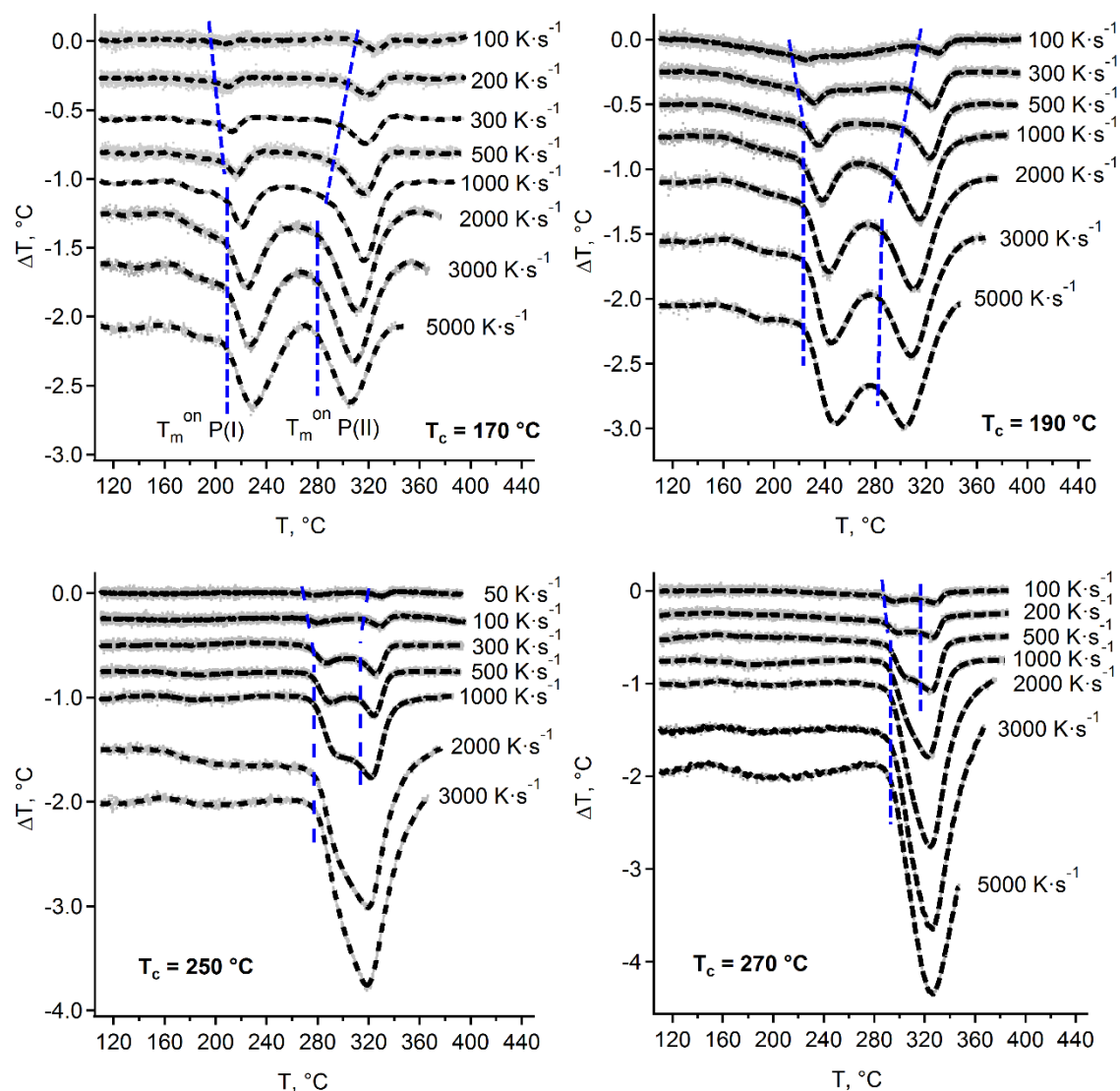


Figure 5.8 Nanocalorimetry curves for isothermally crystallized PEEK ($170\text{ °C} - 270\text{ °C}$) measured from 50 to 5000 K/s after correction for the time lag. The isothermal crystallization temperatures and the applied heating rates are indicated in the graphs.

From this figure it can be seen that, indeed, the temperature shift of the first melting peak onset shows the same slope for all crystallization temperatures for high heating rates. Comparing this to the behavior of the onset of the indium melting peak discussed in Chapter 4.1.6, it seems likely that this effect can be explained by the temperature-lag effect. This temperature-lag is originated by the time a thermal signal needs to be transmitted through the polymer and the surrounding atmosphere before it can reach the thermal sensor/thermocouple

placed at a certain distance from the actual sample position on the active area. This time-lag is characteristic for the particular chip design, but will be most probably affected by the thermal properties of the added sample. When loaded with a miniscule indium sample the time-lag of the sample chip system translates to a response time of 1.72 ms. Since the polymer sample has a higher heat capacity than the indium but a smaller thermal conductivity one could expect an increase in the time-lag effect and thus a larger response time of the sample-sensor system.

Fitting the linear part of the curve, i.e. heating rates higher than 1000 K/s, with a line we obtain the time constant of 4.14 ms for all datasets. Understanding that this time-lag translates to a temperature-lag of more than 4 °C for a heating rate of 1000 K/s it becomes clear, that the fast chip calorimetry measurements have to be corrected in order to draw reasonable conclusions from the data.

Since constant heating rates are assumed, the time-lag can be corrected by just shifting the nanocalorimetry curves to lower temperatures by a constant offset T_{cor} with:

$$T_{cor} = \tau \beta, \quad (\text{Eq. 5.1})$$

where β is the heating rate and τ corresponds to the time-lag or response time of the sample chip system. The corrected datasets are shown in Figure 5.8.

5.1.3 Hoffman-Weeks analysis of the first melting peak

The onset temperatures for the first melting peak for all heating rates used are summarized in Table 5.1 and are graphically visualized in Figure 5.9.

Table 5.1. Onset of the first melting peak $T_m^{on}(I)$ for the indicated isothermal crystallization temperatures and heating rates. Measurements below $50 \text{ K}\cdot\text{s}^{-1}$ are performed with Mettler Toledo DSC I, while the higher heating rates were assessed with the nanocalorimeter (FSC).

heating rate ($\text{K}\cdot\text{s}^{-1}$)	$T_m^{on}(I)$, ($^{\circ}\text{C}$)						
	170	190	210	250	270	300	
0.0833	-	195	214.5	-	273.5	302	
0.3333	DSC	176	200	219.5	-	276	-
0.8333		-	-	-	-	-	306.5
1.3333		180	206	223.5	-	282	-
50		-	-	-	267	-	-
100		195	214	(231)	269	285	-
200		199	-	-	-	287.5	-
300		201	220	(233)	273	-	-
500	FSC	206.5	222	(235)	275	292	-
1000		209	222.5	(242)	277	291.5	-
2000		209	224	(242)	278.5	293	-
3000		209	225	-	278.5	293	-
5000		209	224	-	-	292.5	-

- n.a. values could not be derived from the nanocalorimetric curves

- values in brackets are taken from *in-situ* measurements

Plotting the corrected onset temperatures versus heating rate, the deviation from the linear behavior of the onset can be appreciated not only for the low crystallization temperatures, i.e. 170 and 190 $^{\circ}\text{C}$, but also for the high crystallization temperatures. Interestingly, the critical heating rate at which the onset of the first melting peak starts to be affected by the heating rate is independent of the crystallization temperature. This critical heating rate affecting the onset temperature of the first melting transition will be termed $\beta_{crit,I}$. The exact nature of the critical heating rate and also what exactly happens in the polymer when heating at lower rates, constitutes the discussion point¹.

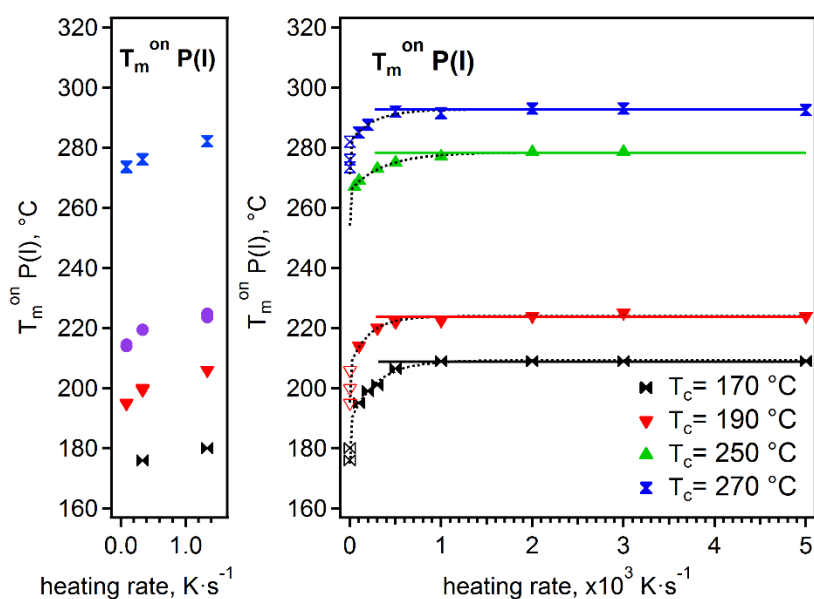


Figure 5.9 Onset of the first melting peak plotted as function of the heating rate over a range from 0.08333 K/s (5 K/min) to 5000 K/s (right). The crystallization temperatures are indicated in the graph. Zoom into the region of low heating rates (left). Data based on nanocalorimetric measurements are shown in filled symbols, while the data based on DSC measurements are shown with open symbols.

In the work previously conducted by Lee and Porter³⁹ a strong heating rate dependency of the first melting peak temperature within a heating rate range of 2 K/min up to 40 K/min was reported. However, at this stage no clear answers were given on what could cause this shift of the first melting peak.

Another interesting fact appears when correlating the results of this work with the findings reported in the past.³⁹ In the literature, the temperature evolution of the melting peaks with the crystallization temperature is commonly used to extrapolate the equilibrium melting temperature T_m^0 using the Hoffman-Weeks plot. In the work of Lee and Porter³⁹, for example, the equilibrium melting temperature was extrapolated to about 390 °C using the peak temperature of the second melting peak. However, when looking on annealed PEEK crystals cold-crystallized in the temperature range from 190 to 320 °C the extrapolated equilibrium melting temperature drops down to 335 °C. This strong deviation, can be explained by the fact that the second melting peak contains only very limited information on the initially formed crystals, but reflects much more the reorganization capability during heating. In other words, the crystals formed during reorganization are not directly correlated to the initial crystallization temperature, but dominant to the recrystallization temperature. In the literature

the extrapolated temperature at 335 °C is typically referred to as “PEEK crystal melting temperature”.⁸⁶ Since this is not known from calorimetry, the Hoffman-Weeks plot cannot be employed to the simple linear extrapolation. This finding is supported by more recent works using fast chip calorimetry showing that the critical heating rate suppressing reorganization is expected to be much higher.^{1,38} However, as it will be shown later in this chapter the authors¹ overestimate the critical heating rate by several orders of magnitude.

To summarize the data on the first melting transition and to shed light on the effects of the heating rate and crystallization temperature, the Hoffman-Weeks plot was generated based on the onset of the first melting peak for all measured heating rates and crystallization temperatures (c.f. Figure 5.10).

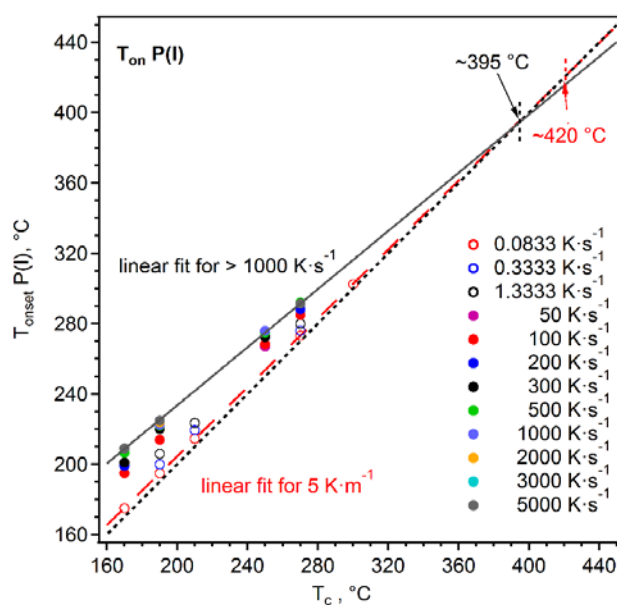


Figure 5.10 Hoffman-Weeks plot for the onset of the first melting transition in PEEK. The linear extrapolation of the equilibrium melting temperature is indicated for the slowest applied heating (red) rate and the fastest heating rate (black).

The first thing that appears is, that the shift of $T_m^{\text{on}}P(I)$ to higher temperatures is very consistent for all crystallization temperatures and allows a linear extrapolation of a temperature where T_m equals T_c as it is done in the literature for T_m^0 estimation.³⁹ However, as can be seen from the data shown in Figure 5.10, the exact value of extrapolation varies with the applied heating rate, but converges to a value 395 °C for heating rates above 1000 K/s, the critical heating rate found from Figure 5.9. However, this value has to be taken with care, since T_m^0 is extrapolated over more than 100 °C and a small imprecision in the

determination of the onset of the melting peak, which is always a point for debate in itself, can lead to strong variation in the extrapolated value.

Interestingly this value coincides with the equilibrium melting temperature estimated from the peak value of the second melting transition for crystallization temperatures higher than 300 °C using heating rates clearly below $\beta_{crit,I}$. This correlation could just be a coincidence. However, when looking on the data of Lee and Porter³⁹ on the isothermally cold-crystallized and annealed PEEK samples, the data shows a strong match with our data when only considering the slow heating rates. Thus, extrapolating the reported peak temperature of the first melting peak linearly to its intersection with the $T_m=T_c$ line, this critical temperature values to 425 °C and is very close to the temperature extrapolated in Figure 5.19 for data measured at 5 K/min. However, since reorganization processes, of whatever nature they may be, cannot be excluded at such low rates heating rates above $\beta_{crit,I}$ should be used for meaningful extrapolation.

5.1.4 Hoffman-Weeks analysis of the second melting peak

The onset temperatures for the second melting peak for all heating rates used in this experiment are summarized in Table 5.2 and on Figure 5.11 in the Hoffman-Weeks coordinates. At this point it is important to mention that values for the onset of the second melting peak have to be taken with scrutiny for crystallization temperatures bigger than 210 °C and heating rates larger than 500K/s. This is due to the convolution of the two melting peaks making it impossible to identify a proper baseline needed for the accurate estimation of the onset.

Using the detailed information on the second melting peak and its evolution with crystallization temperature and heating rate, correlations to the results shown in previous works^{39,1} can be performed. Thus the onsets of the second melting peak are added to the Hoffman-Weeks plot as shown in Figure 5.11. Looking at the $T_m^{on}P(II)$ for all the heating rates used in this study it appears that there is again a systematic and consistent variation of the melting temperature increase with increasing heating rates. For heating rates as low as 5 K/min a dependence on the heating rate can hardly be observed. This shows that such slow heating rates generate a situation when the material has enough time to fully reorganize, independently of the initial crystallization temperature. This is interesting as it marks the

lower limit of the reorganization allowing to extrapolate the maximum melting temperature the material can adopt for complete recrystallization. The temperature of 330 °C found in the reported experiments is in close agreement with results reported for cold-crystallized and annealed samples showing a maximum melting temperature of 335 °C.

Table 5.2. Onset of the final melting peak $T_m^{on}(II)$ for the indicated isothermal crystallization temperatures and heating rates. Measurements below 50 K·s⁻¹ were measured with Mettler Toledo DSC I, while the higher heating rates were measured using the nanocalorimeter (FSC).

heating rate (K·s ⁻¹)	$T_m^{on}(II)$ (°C)					
	170	190	210	250	270	300
0.0833	-	329	330	-	328.5	331.5
0.3333	DSC	326	324.5	325	-	324
0.8333		-	-	-	-	324.5
1.3333		317	318	320	-	323.5
50		-	-	314	318	-
100		305	312	-	316	317
200		299	-	-	-	314
300		295	309	-	314	-
500	FSC	290	302	-	312	313
1000		285	290	(293)	310	n.a.
2000		280	285	(293)	309*	n.a.
3000		278	284	-	309*	n.a.
5000		278	283	-	-	n.a.

* Values are estimated from a change of slope in the melting line
 - n.a. values could not be derived from the nanocalorimetric curves
 - values in brackets are taken from *in-situ* measurements

A linear extrapolation for higher heating rates is not possible since the shift of the second melting peak onset is not expected to be linearly correlated with the crystallization temperature. In order to shed light on these cross-correlations the onsets of the second melting peaks are plotted as function of the heating rate (c.f. Figure 5.12.) The presented data are based on fast chip calorimetric measurements for heating rates larger than 2 K/s, visualized with filled symbols, while the data based on DSC measurements are shown with open symbols. On the left side of the figure a zoom of the low heating rate region is shown to appreciate the evolution of the peak shift at heating rates below 2 K/s.

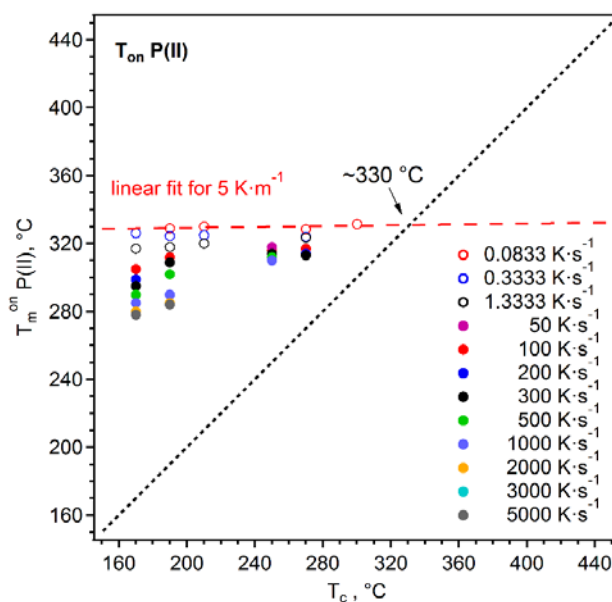


Figure 5.11 Hoffman-Weeks plot for the onset of the second melting transition in PEEK. The linear extrapolation to the iso-temperature line, e.g. $T_m = T_c$, is indicated for the slowest applied heating rate (red dashed line). The filled symbols represent data derived from fast chip calorimetry measurements, while the open symbols represent data obtained by conventional DSC.

The first point that attracts attention in this graphical representation of the data is that at heating rates as low as 20 K/min the second melting peak drifts already to lower temperatures. This shows that when heating at 20 K/min the recrystallization does not have enough time to complete, in contrast to the situation when heated with 5 K/min. The resulting decrease in the onset temperature of the final melting peak reflects the decreasing crystal stability with increasing heating rates.

It is also interesting that this is the case for all crystallization temperatures used throughout this study. However, at a heating rate of 80 K/min we can already see that the magnitude of the onset temperature decrease correlates with the crystallization temperature. The effect is the largest for low T_c . With further increase of the heating rate this effect continues until the depression of the second melting peak onset levels off. This dependence can be well described with a double exponential function indicating that more than one process takes place. The time constants for the two exponential terms are of different magnitudes, being on the order of 100 K/s for the fast decay contribution, while the other time constant is in the range of 100 to 1000 K/s¹. However, since it is not clear on what is the exact nature of the underlying mechanisms, the dashed lines should be considered to be simply a guide for the eye.

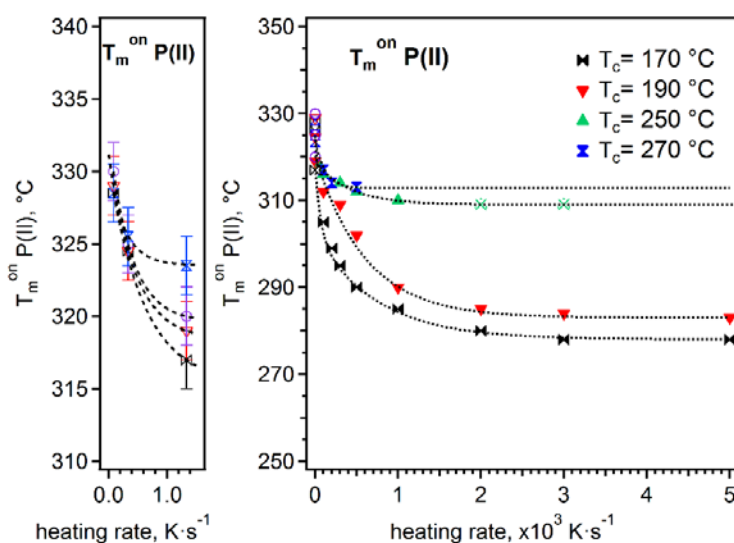


Figure 5.12 Onset of the second melting transition plotted as a function heating rate. The zoom presented on the left side is to appreciate the evolution in the region where low heating rates are applied using conventional DSC. The filled symbols represent data derived from fast chip calorimetry measurements, while the open symbols represent data derived from conventional DSC. The data visualized by a green cross are estimated from the change of slope in the melting line (c.f. .)

We speculate that this "leveling-off" of the peak corresponds to a critical situation where the reorganization process is largely suppressed. The fact that there is no exact critical heating rate above which the recrystallization does not occur appears logical since the driving force for the recrystallization should still exist at high heating rates. However, due to fast heating, the time to reorganize is scarce. The time constants for the double exponential fit are given in Table 5.3.

Table 5.3. Time constants for data shown in Figure 5.12 based on the double exponential decay.

$T_c, ^\circ\text{C}$	$\tau_1, \text{K/s}$	$\tau_2, \text{K/s}$
170	108	805
190	104	729
250	101	285
270	100	98

While τ_1 corresponds to the time constant describing the evolution of the $T_m^{\text{on}}P(II)$ at low heating rates τ_2 corresponds to the time constant describing the final melting point depression at higher heating rates. This time constant τ_2 seems to be most likely connected to the recrystallization and its suppression with increasing heating rate respectively. As the time constant τ for an exponential decay function marks the position of $1/e \approx 0.368$ remaining

parts, it makes sense to classify $2\tau \approx 0.13$ as a reasonable value for a critical threshold. This critical heating rate will be termed as $\beta_{crit,II}$ for the rest of the manuscript.

5.1.5 The double melting of PEEK

Recollecting that the first melting temperature onset showed a convergent behavior as well, it can be informative to correlate the corresponding melting temperatures for each crystallization temperature. The onset melting temperatures for the first and second melting peaks for an infinitely high heating rate are given in Table 5.4.

Table 5.4. $T_{m,inf}^{on}P(I)$ and $T_{m,inf}^{on}P(II)$ with respect to the crystallization temperature T_c .

T_c , °C	$T_{m,inf}^{on}P(I)$, °C	$T_{m,inf}^{on}P(II)$, °C
170	209.0	278.0
190	224.0	283.0
250	278.5	309.0
270	292.5	313.0
300	307.0	324.5

When plotting the second melting peak onset as function of the first melting peak onset it is possible to linearly extrapolate towards the $T_m=T_c$ line only for heating rates above the critical values (cf. Figure 5.13). Interestingly, the extrapolated temperature of 330 °C correlates very well with the maximum melting temperature derived from Figure 5.11.

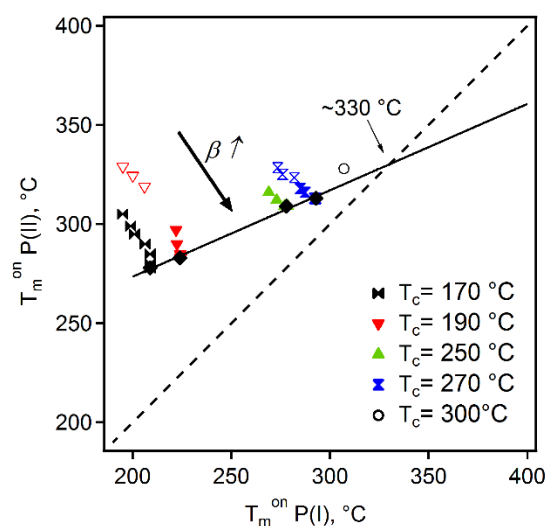


Figure 5.13 Onset of the second melting peak, $T_m^{on}P(II)$ plotted vs. the onset of the first melting peak $T_m^{on}P(I)$. The black rhombs correspond to heating rates above the critical heating temperature. The $T_m=T_c$ line is indicated by a dashed line. The black arrow indicates an increase in heating rate. The open symbols correspond to data derived from DSC while the filled symbols

represent data derived from nanocalorimetry measurements.

The linear progression through $T_{m,inf}^{on}P(II)$ vs. $T_{m,inf}^{on}P(I)$ indicates that the situation where the heating rate is clearly above the critical heating rates for both temperatures corresponds to a state where both melting peak onsets reflect the initial crystal stability. However, realizing that in addition to the first melting peak the second melting peak does correlate, or better say scales, to the initial crystal stability as well, several new questions about the underlying mechanisms are now open. At this moment one can only speculate on how the second melting peak is correlated to the initial crystal stability. However, it appears unlikely that such a strong correlation of the high and low melting peak temperatures is compatible with the existence of two, probably independent, crystal populations. Having excluded reorganization during heating and the unlikeliness of two independent crystal populations, another explanation for the double melting of PEEK has to be explored. When looking at the examples of other semi-rigid chain polymers exhibiting double melting behavior, e.g. polytrimethylene terephthalate (PTT), indications can be found in the literature correlating the existence of double melting endotherms to the stress-induced sacrificial melting of the most stressed, and, therefore, less stable, crystals, thus, stabilizing the neighboring crystals and shifting their melting to higher temperatures. The corresponding model based on the Hosemann paracrystallinity analysis was applied to explain the double melting of PTT by Ivanov et al.^{111,139,162} The basic idea of this model is that the secondary crystallization process can take place after the initial crystallization process, allowing further crystallization of the inter-lamellar amorphous phase by inserting additional lamellar crystals. Densification of the inter-lamellar gap results in the generation of stresses imposed on the neighboring crystals and depressing the melting temperature, accordingly.

5.1.6 Recrystallization diagram from calorimetry

In Figure 5.14 the recrystallization diagram for melt crystallized PEEK is displayed, based on the information presented so far. The diagram shows the data points gathered and discriminated into two groups according to whether the measurements for the indicated crystallization temperatures and applied heating rates are above or below the critical value of $2\tau_2$. The boundary line is estimated by the dashed line in Figure 5.14. In addition, the data points are color-coded representing the deviation of the actual onset of the second melting

endotherm from $T_{m,inf}^{on}P(II)$, or in other words, the difference of the second melting onset with respect to its value at infinite high heating rates (see the right column in Table 5.4).

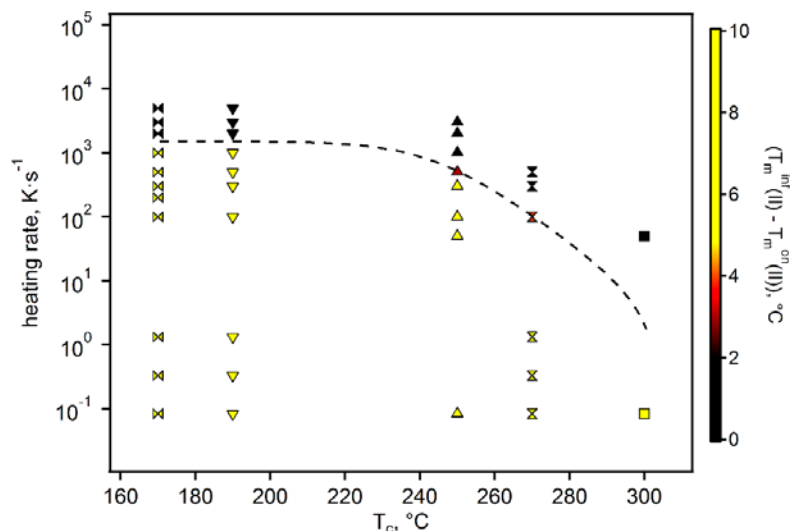


Figure 5.14 Recrystallization diagram based on calorimetric data. The color-code represents the relative shift of the second melting peak onset with respect to an estimated equilibrium melting peak onset derived from the plateau as indicated by the color-code (cf. the color-bar on the right). The dashed line represents the transition state, or critical heating rate, above which no recrystallization takes place)

It seems surprising that the critical heating rates are below 2000K/s for the studied range of crystallization temperatures since critical heating rates in the literature are predicted to be orders of magnitudes higher.¹ Nevertheless, at this moment these time constants have to be taken with scrutiny, and an alternative approach, to crosscheck their validity has to be employed. As discussed before, a valid check of the recrystallization premises can only come from the assessment of the structural change occurring in the polymer during recrystallization, as it will be shown in section 5.2 of this chapter.

5.1.7 Early stages of crystallization in PEEK

To further explore the idea of a two-stage crystallization model put forward in the previous section an experimental approach was designed where the material is given only a very short period of time to crystallize. If a secondary crystallization process taking place at timescales of seconds after the initial crystallization sets in, it can be expected that this approach should be able to sense the effect of the secondary crystals due to changes in the melting behavior.

Such experiments are not without precedent in the literature using fast chip calorimetry^{1,38} but also with conventional DSC.^{117,124,128,127}

In such interrupted crystallization experiments, PEEK was subjected to isothermal crystallization for different crystallization times and then quenched and subsequently scanned with the calorimetry technique. The results reported are partially contradictory. While in some instances both melting peaks were observed for very short isothermal crystallization times, t_c , in other cases only the high temperature melting could be observed for short t_c while the first melting peak develops only at longer t_c . The latter case would imply that in the first moment of crystallization only the high-temperature melting crystals are formed. Such evidence would support the idea of the existence of several crystal populations present in the material, while the first case would be still compatible with the model of “melting-recrystallization” where high-temperature melting crystals were assumed to be formed in the result of the melting-recrystallization process and did not exist after isothermal crystallization.

However, in most cases of the reported experiments, arbitrary heating rates of 1000 K/s and smaller were used even for low crystallization temperatures. Comparing this to the data shown in the last section of this manuscript, it appears that recrystallization of the material cannot be excluded in the case of a too low heating rate. This shows that a priori, a clear interpretation of the data is only possible when a reorganization or recrystallization can be excluded. A premise for that is to know the critical heating rates and its dependence on the crystallization temperature, which was established in the previous section of this chapter.

In Figure 5.15 data derived from the “interrupted crystallization experiments” are shown. Four crystallization temperatures at the lower end of the crystallization window were selected in order to have a maximum distance between two melting peaks making the observation of minuscule changes in the calorimetry curve more evident. For all shown experiments the same PEEK sample was used after repeated recrystallization of the material. The corresponding crystallization times are given in the legend of the graphs and range from 1 s to 5400 s. The curves are plotted with a vertical offset for better appreciation of the melting peak development.

On the displayed data in Figure 5.15, the rate of crystallization can be indirectly appreciated by following the magnitude of the stepwise slope change in the T_g region. Most clearly this

can be observed for the samples crystallized at low crystallization temperatures, i.e. 160 and 170 °C, as shown in Figure 5.15 A and B, respectively. With increasing crystallization temperature the moment when the first feature of any melting peak becomes visible shifts from 120 s for $T_c = 160$ °C down to 20 s for the sample crystallized at $T_c = 170$ °C and even to 2 s for $T_c = 190$ °C.

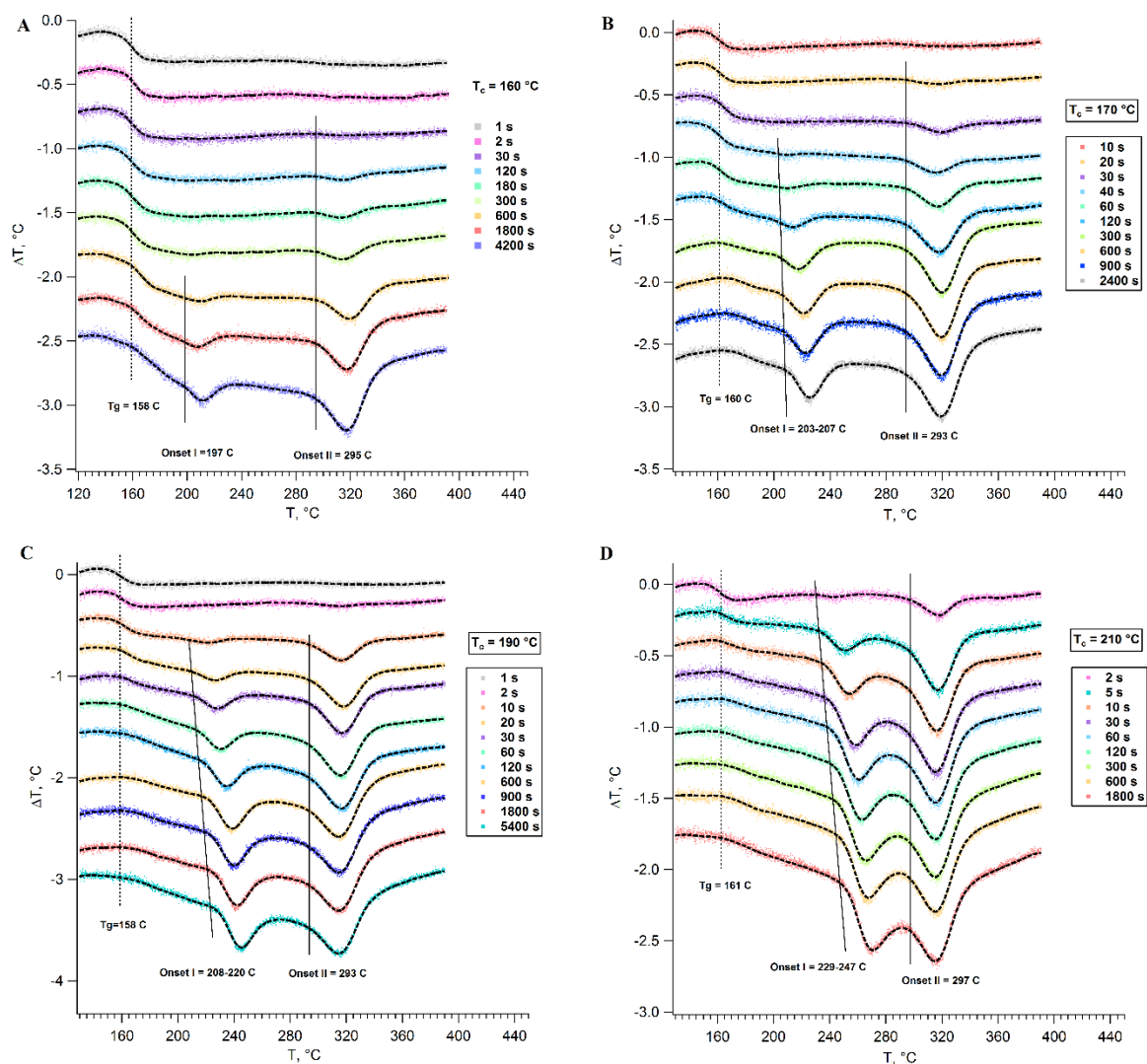


Figure 5.15 Nanocalorimetry curves of partially crystallized samples measured at 1000 K/s. The samples were crystallized at the following temperatures: A - 160°C, B - 170°C, C - 190°C, D - 210°C.

This clearly shows that with increasing crystallization temperature the rate of crystallization increases within the investigated crystallization temperature window. In the same way, as the melting peaks start to appear the magnitude of the step at T_g decreases, being a good measure for the amount of the crystalline fraction in the beginning of the melting experiment.

Following the development of this feature with increasing crystallization time is very informative because it can give information on crystallinity present during the initial stage of the heating experiment.

In contrast, the crystallites formed above T_g during heating will not affect the T_g step. Thus, taking the step at T_g into account allows discriminating the melting contribution of the initially formed crystals from the ones that form during heating from the nuclei generated during quenching to and below T_g , which would appear later in form of melting peaks in the heating curve.

Interestingly, for the low crystallization temperatures of 160 and 170 °C, it seems that the second melting peak appears at shorter crystallization times as compared to the first melting peak. For the highest crystallization temperature, i.e. 210 °C, the case seems to be different (cf. Figure 5.15 C and D). Here, the appearance of the second melting endotherm is always accompanied by an appearance of the first melting peak below 2 s crystallization time for a $T_c = 210$ °C. The reason for this change in behavior can be attributed to the heating rate used in these experiments.

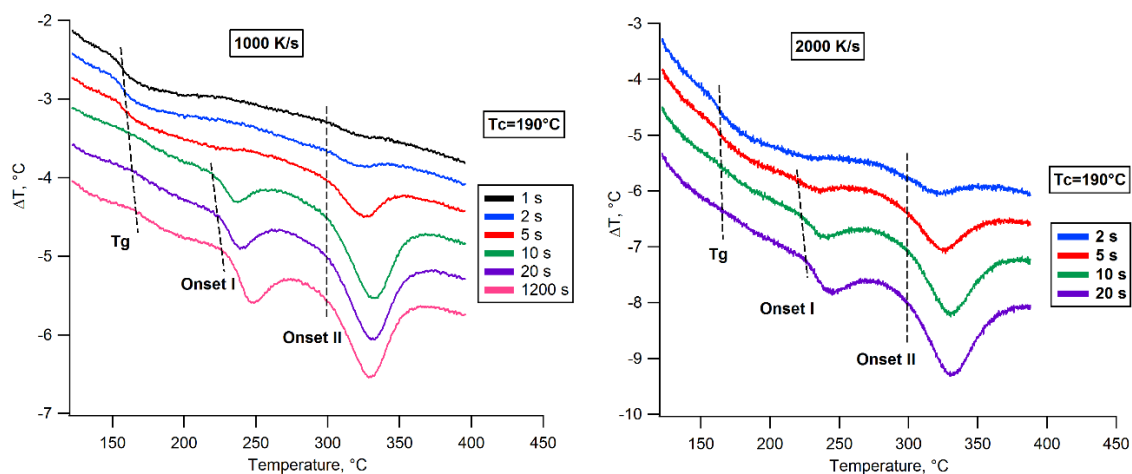


Figure 5.16 Nanocalorimetry curves of partially crystallized PEEK at $T_c = 190^\circ\text{C}$ using heating rates of 1000 and 2000 K/s, (a) and (b), respectively. The vertical offset of the curves is added for clarity.

In all the shown cases the heating was performed at a rate of 1000 K/s, which, as was discussed in the previous section of this chapter, is too low to fully suppress the recrystallization process of PEEK for samples crystallized below 190 °C. Therefore, the absence of the first melting peak can be explained by two processes of opposite enthalpic

nature taking place almost simultaneously, melting of the initially isothermally crystallized crystals and recrystallization of these crystals into a more stable crystal fraction.

In order to be able to draw correct conclusions from such experiments, one has to bypass the critical heating rates. An example of such dataset is shown in Figure 5.16 for PEEK samples crystallized at 190 °C and subsequently heated using heating rates of 1000 K/s and 2000 K/s respectively. One interesting effect that can be observed from these experiments is the shift of the first melting peak to slightly higher temperatures at sub- and super-critical heating rates. This shift of up to 20 °C for the case of $T_c = 160$ °C could be indicative of an annealing effect of the initially appearing crystals during isothermal crystallization.

Remembering that the critical heating rate is between 1000 and 2000 K/s for PEEK crystallized at $T_c = 190$ °C, the picture starts to become better understood. Using a heating rate of 1000 K/s the high-temperature melting peak can be observed already after 2 s of crystallization time while the low-temperature melting peak appears only after 5 s of crystallization. In contrast, the low-temperature melting peak and high-temperature melting peak appears together after 2 s of crystallization time when heated with a rate of 2000 K/s. A further increase in the used heating rate does not change the situation further: the low-temperature melting peak appears at the same time as the high-temperature melting peak. Being not able to find the experimental conditions where for super-critical heating rates the high-temperature melting peak is present while the low-temperature melting peak is absent brings us to the following three conclusions. Either, the secondary infilling crystallization does not occur under the investigated conditions, or if it does occur, this operates at different time scales. Either way, it would not have an effect on the double melting behavior observed under exact these conditions. In this case, it would be just impossible to resolve its effects using the techniques at hand.

5.2 The double-melting of PEEK by fast chip calorimetry and WAXS

Even though the main objective of this project was to combine fast chip calorimetry with millisecond time-resolved micro-diffraction to study the double melting behavior of PEEK one cannot neglect the melting behavior at very slow rates.

However, when heating at slow rates, it is not necessary to use microscopic samples, since the thermal inertia of the sample is no issue for the heating. On the contrary, a certain mass is required in order to record a thermal signal during heating as the amplitude to the thermal signal scales with the heating rate and the sample mass. Another reason against the use of the calorimeter chip for slow heating rates is due to the beam damage. The radiation damage of PEEK and its effect on the recrystallization process are discussed in great detail in Chapter 4.2.5. Therefore, it is not advisable to combine a slow heating experiment, which will run for a significant amount of time where the duration of a heating experiment is in the order of hours, with the high flux microbeam setup at the ID13, but to use conventional in-situ setups allowing for variable temperature measurements combined with small and wide angle X-ray scattering.

For the experiments reported here the SAXS-WAXS setup of the BM26 beamline was used. A milligram sized PEEK sample previously isothermally crystallized at 270 °C was heated with a heating rate of 5 K/min above its melting temperature using a Linkam DSC hot-stage compatible with the experimental setup of the BM26 SAXS-WAXS station. The photon energy of the X-ray beam was 12.4 keV. The footprint of the beam at the sample was 700 x 300 μm^2 (H x V). The 2D wide-angle diffraction patterns were recorded using a Pilatus 300k-W placed at a distance of approximately 20 cm from the sample at an angle of about 30°. The inclination of the detector was chosen because this configuration allows to simultaneously collect SAXS data. The geometry of the measurement was calibrated using several diffraction peaks of $\alpha\text{-Al}_2\text{O}_3$ and the pyFAI library¹⁵⁴ provided by the ESRF.

5.2.1 Structural Signature of PEEK during heating

The reduced 1D wide-angle diffraction patterns are shown in the form of a 2D representation in Figure 5.17 as a function of the modulus of the scattering vector s and the temperature of

the sample. The four main diffraction peaks are indicated in the graph. Unfortunately, the parasitic diffraction signal originated from the sample cell is in superposition with the 200 reflection of PEEK. However, using the fitting algorithms described earlier in Chapter 4.2.4 the diffraction pattern could be decomposed in the crystalline, amorphous contribution of the PEEK sample and the contribution coming from the setup, such as air scattering and contribution from the measuring cell.

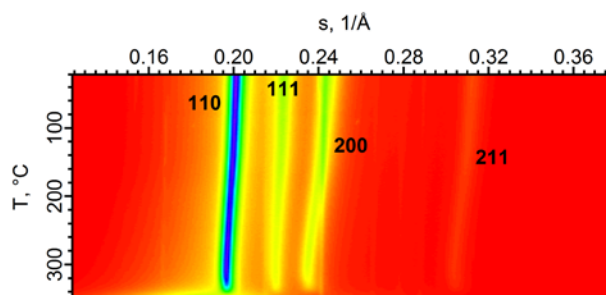


Figure 5.17 2D representation of 1D diffraction curves plotted as a function of the modulus of the scattering vector s and as a function of temperature. The PEEK sample isothermally crystallized at 270 °C was heated from RT to 360 °C using a heating rate of 5 K/min. The main four diffraction peaks are indicated in the graph. The color code range is (red - yellow -blue) to indicate increasing intensity.

As the first step after decomposition of the data, the lattice parameters of the PEEK sample as a function of temperature was fitted using the following equation:

$$d(hkl) = \frac{1}{\sqrt{\left(\frac{h}{a}\right)^2 + \left(\frac{k}{b}\right)^2 + \left(\frac{l}{c}\right)^2}} \quad (\text{Eq. 5.2})$$

In this equation h , k and l are the miller indices of the diffraction peaks while a , b and c represent the unit cell parameters. The formula was applied under the assumption that the unit cell of PEEK keeps its orthorhombic nature. As experimental data the d -spacings of the diffraction peaks shown in Figure 5.18 (right) as solid lines were used.

The unit cell parameters are plotted as a function of temperature for the heating run shown in Figure 5.17 are plotted in Figure 5.18 (left) as a function of the sample temperature. The fitted unit cell parameters were then used to recalculate the d -spacings of the diffraction peaks e.g. dashed lines in Figure 5.18 in order to appreciate the accuracy of the fit. The slight discrepancy to the experimental data, which is increasing with the diffraction angle, is caused by a small error introduced during the calibration procedure caused by a slight distance change when the calibration sample was measured. The reason for that is that the calibration

sample was too large to fit into the DSC cell introducing a small error in the sample detector distance of ca. 2 mm. This can be confirmed by the fact, that the lattice parameters displayed in the left part of the figure are slightly too large. However, this will not change the major conclusions drawn from this measurement, as we will focus on the discussion of relative changes during heating.

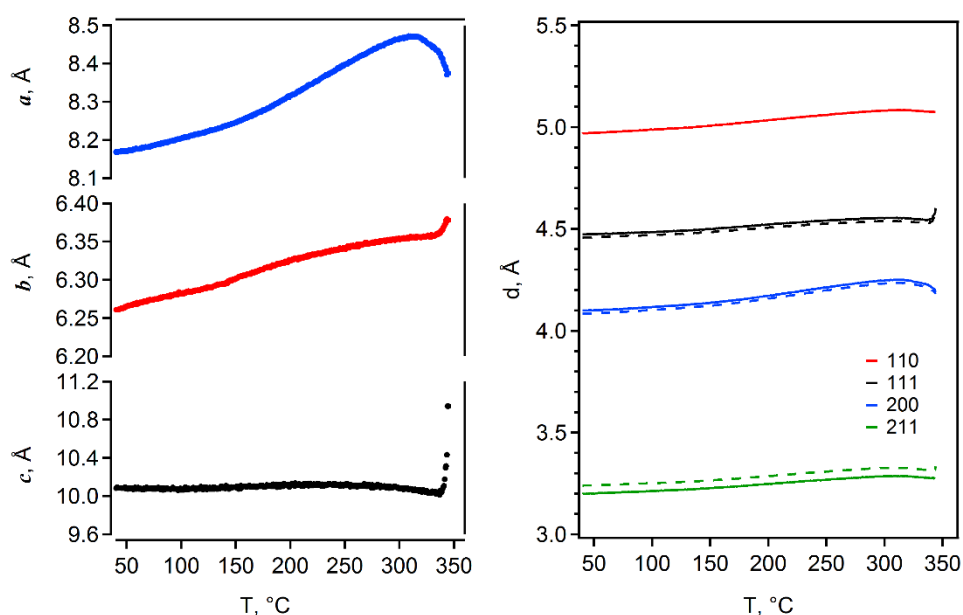


Figure 5.18 Lattice parameters as a function of temperature, recalculated from the diffraction peaks indicated in figure Figure 5.17, are shown in the left part. The experimental and calculated d-spacings of the main diffraction peaks are given in the panel on the right. The experimental data are represented by solid lines, while the recalculated data are represented with dashed lines.

All three unit cell parameters show a different evolution in the course of heating. While the c -parameter does not significantly evolve with temperature, both, a - and b -parameter show clear changes with increasing temperature. The increase of the b -parameter at the very last stages of the heating can be attributed to the final melting process of the crystalline phase. However, the a -parameter shows different behavior. In order to better appreciate the evolution the a - and c - lattice parameters are shown together with the evolution of the crystallinity and the DSC curve in Figure 5.19.

The evolution of the a -parameter with temperature consists of three main regions. At low temperatures below T_g only the thermal expansion of the PEEK lattice can be observed. Above T_g the thermal expansion increases until the onset of the second melting transition is reached as it can be seen from the DSC curve (red) and the change in the slope of the crystallinity index (green). The increase in the slope of the thermal expansion above T_g is due

to the higher flexibility in the amorphous inter-lamellar phase which is reducing the pressure on the lamellar crystals. As soon as the onset of the 2nd melting transition is reached the *a*-parameter shows a sudden decrease with increasing temperature until the final melting is reached.

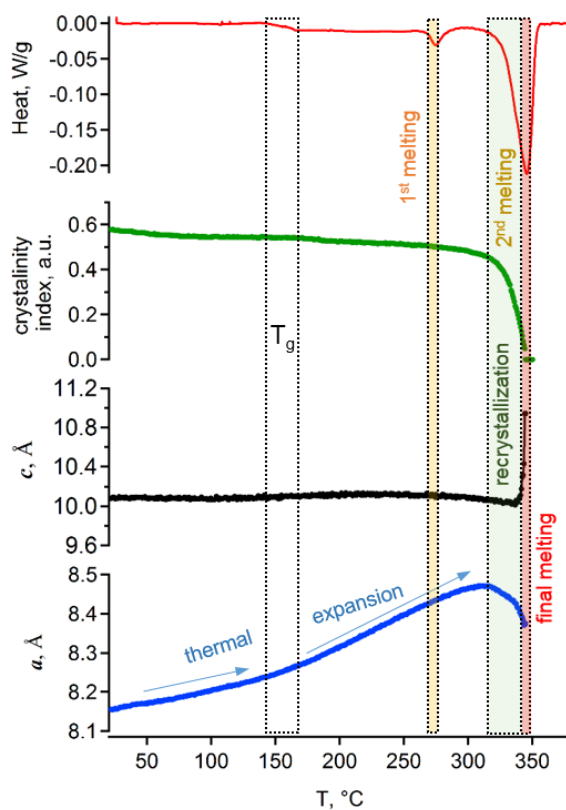


Figure 5.19 Evolution of *a*-parameter, area under 200 crystalline reflection and a DSC curve of a PEEK sample isothermally crystallized at 270 °C and scanned at 5 K/min.

The onset of the *a*-parameter decline coincides with the onset of the melting peak. Importantly, at that moment the *c*-parameter is not yet affected. This unusual behavior could be attributed to the onset of a recrystallization process allowing the lattice to adopt a better thermodynamic state by rearranging the atomic positions. This finding is supported by the fact that when PEEK is crystallized at increasing temperatures the "equilibrium" lattice parameters, specifically the *a*-parameter, decreases^{97,98} as it is shown later (chapter 5.2.2). However, in order to confirm that the reduction in the *a*-parameter indicates a recrystallization process comparative measurements at higher heating rates are required.

5.2.2 Recrystallization and critical heating rates in PEEK

Having a first idea on what the structural signature of the recrystallization in PEEK could be, it is necessary to test this premise by applying higher heating rates and recording the structural parameters simultaneously. To be able to achieve higher heating rates in X-ray diffraction experiments, the nanocalorimetric setup had to be made compatible with a high flux micro-beam setup. The technical developments and the challenges along the way of the integration of this setup into the ID13 micro-beam instrument are discussed in some detail in Chapter 4.2 together with issues of the sample preparation for the nanocalorimetric measurements. Therefore, only the most important experimental parameters are shortly summarized to the extent needed to comprehend the X-ray diffraction analysis of the portrayed experiments. For the ID13 measurements, an X-ray beam with a photon energy of 13 keV was used. The acquisition time for the X-ray recording was varied from 1.34 to 5 ms to find an optimal compromise between the scattering intensity and the temperature resolution affected by the applied heating rate. For all the experimental data are shown further on in this manuscript the nanocalorimeter was used.

In order to better appreciate the differences in the thermal behavior of PEEK when heated below and above the expected critical heating rate, two experiments are used as a showcase (cf. Figure 5.20). In the experiments, the heating rate of 100 K/s is the same in both cases, but the crystallization temperatures of 210 and 270 °C are chosen in a way that in the first case the heating rate should be safely below the critical value, while for the latter case the heating rate should be above it. In Figure 5.20, the evolution of the lattice a -parameter of the PEEK unit cell (black) is given together with the normalized peak intensity of the 200 reflection (blue). In addition, the nanocalorimetric signal is added (red) to be able to correlate the structural and thermal events.

When heating with sub-critical heating rate, as it is the case for PEEK isothermally crystallized at 210 °C heated at 100 K/s, the peak intensity (blue) shows a stepwise intensity drop coinciding with both main melting endotherms (red), cf. Figure 5.20 (top). While the first transition at about 230 °C is followed by a plateau like continuation, the onset temperature of the second melting event cannot be identified with reasonable precision from the calorimetric and intensity data, but can be estimated to be at 300 °C as it can be seen from the second stepwise decrease in the intensity curve. At the same time the a -parameter

changes its slope and starts to decrease in a similar way as seen for slow heating data of PEEK isothermally crystallized at 270 °C, cf. Figure 5.19.

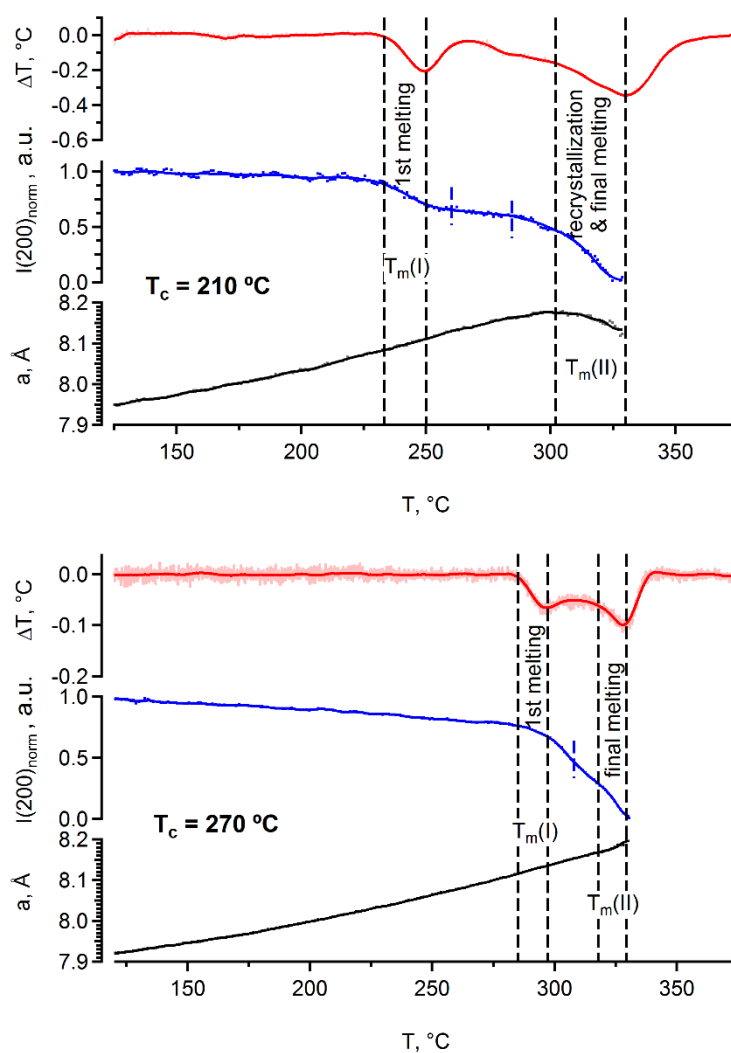


Figure 5.20 In-situ heating experiments of PEEK isothermally crystallized at 210 °C (top) and 270 °C (bottom) and subsequently heated using a heating rate of 100 K/s. The temperature evolution of the normalized 200 peak intensity (blue) is plotted together with the a -parameter of the unit cell (black). The signals from the nanocalorimeter (red), simultaneously recorded during the heating, are shown to correlate the structural changes with thermal events.

In contrast, the heating of the PEEK sample isothermally crystallized at 270 °C does not show a stepwise decrease of the peak intensity at the melting peaks, but shows a continuous transition from one melting peak into the other. This can be explained by a convolution effect caused by a slight overlapping of the two melting peaks. This slight overlap can be seen in the nanocalorimeter signal, i.e. the red curve in Figure 5.20 (bottom), where the baseline is not reached in-between both melting endotherms. However, the main difference between the

two cases, $T_c = 210\text{ }^\circ\text{C}$ and $T_c = 270\text{ }^\circ\text{C}$, is that for the latter no decrease of the lattice a -parameter can be observed during the second melting peak onset.

Thus, the structural signature of the recrystallization taking place in PEEK when heated with sub-critical heating rates is identified as a decrease of the lattice a -parameter at the moment the second melting peak sets on. By knowing the structural signature of the recrystallization in PEEK, it now becomes possible to screen a large parameter space of crystallization temperatures and heating rates and to rank them according to the evolution of the lattice a -parameter.

A set of in-situ nanocalorimetry experiments combined with millisecond time-resolved micro-diffraction were conducted on PEEK samples isothermally crystallized at four different crystallization temperatures, i.e. 190, 210, 270 and 300 $^\circ\text{C}$. The applied heating rates ranged from 50 up to 2000 K/s. In order to get the full understanding of the recrystallization process at the lower end of the heating rate spectrum measurements on milligram-sized samples were conducted at the BM26 and added to the dataset.

The lattice a -parameter derived from the fast and slow in-situ WAXS measurements for the four chosen crystallization temperatures are shown in Figure 5.21. The different heating rates are color coded and specified in the legend. Generally, all curves show a similar evolution of the a -parameter with temperature. At the initial stage the a -parameter increases due to the thermal expansion of the lattice. At T_g the slope of the thermal expansion increases further till the final melting sets in. However, with increasing crystallization temperature less and less of the a -parameter decrease is observed indicating a reduction in the extent of recrystallization.

One interesting feature that can be observed is the decrease of the initial lattice parameter, i.e. the one at 110 $^\circ\text{C}$, with increasing crystallization temperature. For example, the a -parameter of PEEK isothermally crystallized at 300 $^\circ\text{C}$ is 7.87 \AA at 110 $^\circ\text{C}$, while it is 7.93 \AA when crystallized at 190 $^\circ\text{C}$. This decrease in the lattice a -parameter value is a well-documented feature of PEEK extensively discussed in the literature^{97,98}.

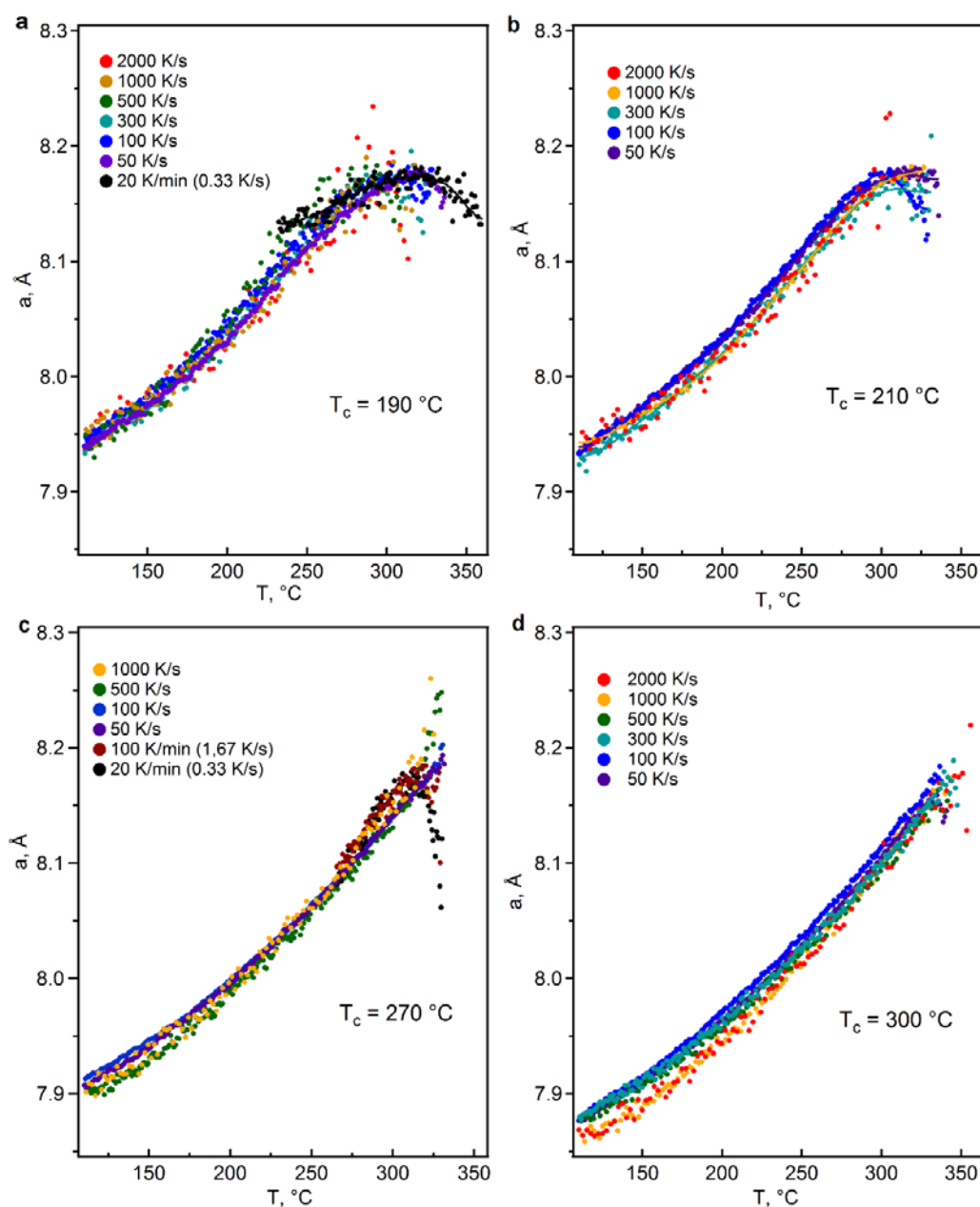


Figure 5.21 Evolution of the a -parameter as a function of temperature in the fast heating experiments, A - $T_c = 190\text{ °C}$, B - $T_c = 210\text{ °C}$, C - $T_c = 270\text{ °C}$, D - $T_c = 300\text{ °C}$.

Due to the fact that the low-temperature lattice parameters of PEEK decrease with increasing crystallization temperature one can conclude that the PEEK lattice wants to adopt smaller lattice parameters than compared to lattice parameters the sample reached by thermal expansion during heating. This particularity explains why PEEK shows recrystallization behavior in general. Simply speaking during the recrystallization process the system tries to reach a state with less free energy, which in this case represents crystals with a smaller a -parameter.

In order to better appreciate the evolution of the a -parameter as a function of temperature, the same curves from Figure 5.21 are replotted in Figure 5.22 with a vertical offset. Just by identifying the curves where the a -parameter curve does or does not show a decrease with the onset of the final melting peak, one can discriminate the curves in the two categories whether they show recrystallization upon heating or not.

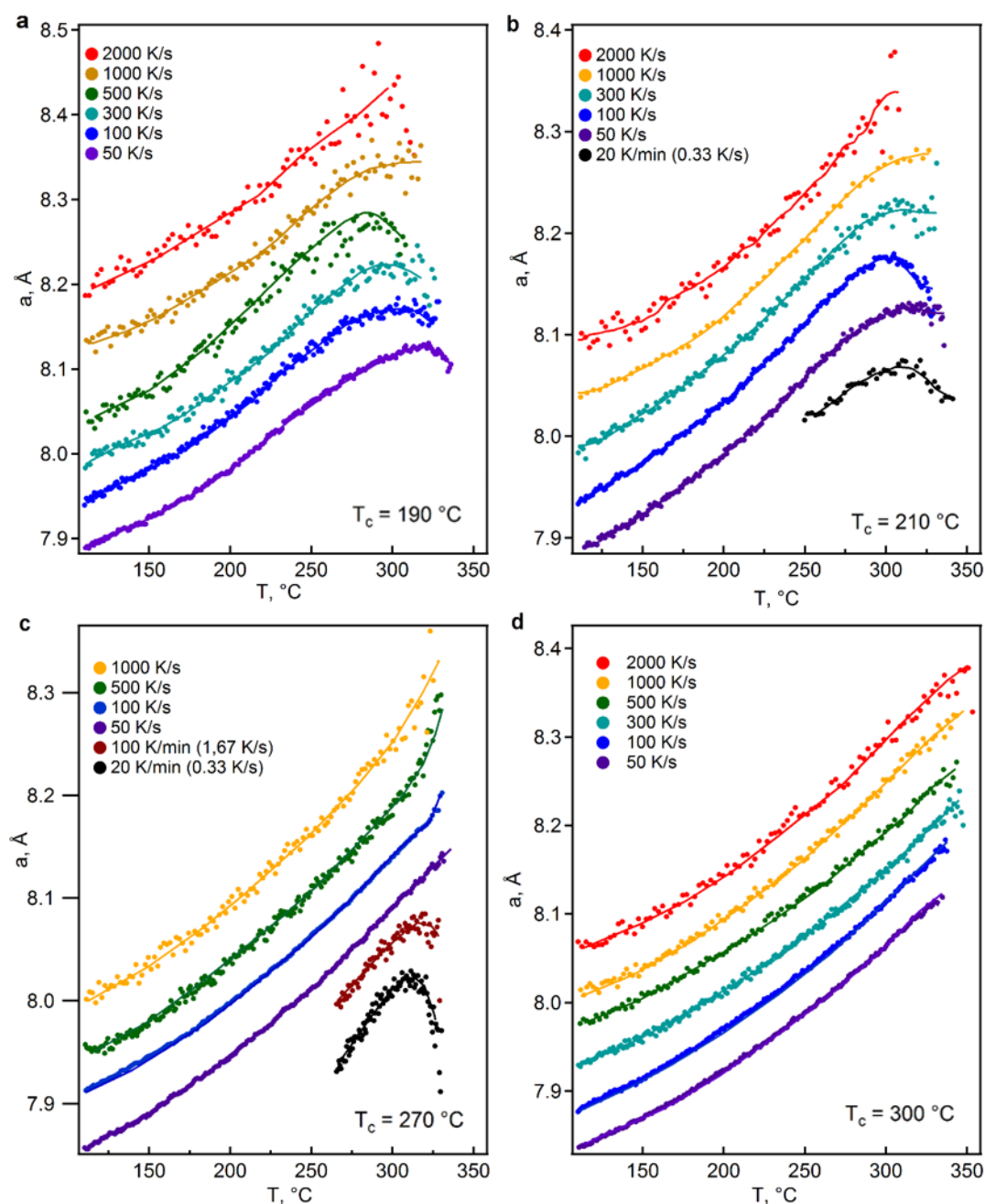


Figure 5.22. Evolution of the a -parameter as a function of temperature in the fast heating experiments, A - $T_c = 190^\circ\text{C}$, B - $T_c = 210^\circ\text{C}$, C - $T_c = 270^\circ\text{C}$, D - $T_c = 300^\circ\text{C}$. The heating rates are color coded as shown in the legends. The curves are plotted with a vertical offset for better appreciation of the a -parameter evolution with temperature.

Generally, a decrease of the recrystallization process extent can be observed with increasing heating rate, as well as with increasing crystallization temperature. It appears obvious that the temperature window in which the recrystallization takes place significantly shrinks with increasing crystallization temperature until it almost disappears in the case of samples crystallized at 300 °C. That means that samples crystallized at 300 °C initially form crystals close to maximum thermal stability and have, thus, a very low tendency to recrystallize.

The critical heating rate, $\beta_{crit, II}$, for the samples isothermally crystallized at low temperatures, i.e. 190 °C and 210 °C, is estimated to be between 1000 and 2000 K/s. For the samples isothermally crystallized at higher temperatures, i.e. 270 °C, the critical heating rate decreased to values below 50 K/s. For the samples crystallized at 300 °C no parameter combination showing recrystallization was found within the measurements conducted.

5.2.3 Recrystallization diagram from calorimetry and X-ray micro-diffraction

Using the information given in the previous section, the recrystallization diagram for PEEK can be constructed.

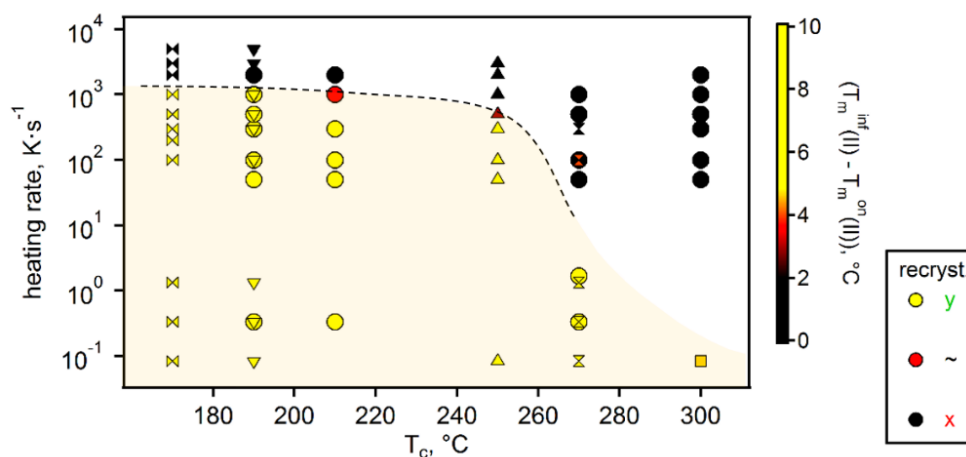


Figure 5.23 Recrystallization diagram for melt-crystallized PEEK. The circles represent data derived from WAXS analysis, while other symbols represent data derived from the nanocalorimetry data alone. The color of the symbols indicates whether recrystallization was observed under these conditions, i.e. crystallization temperature and heating rate. The black symbols indicate that no substantial recrystallization was observed, yellow symbols indicate that the material recrystallizes upon heating. The red color stands for the transient situation where partial recrystallization was observed.

Figure 5.23 shows the recrystallization diagram for melt-crystallized PEEK derived from the combination of the nanocalorimetric and X-ray data. The circles in the diagram represent data taken from the α -parameter analysis, while the other symbols represent data derived from the nanocalorimetry data alone (c.f. Figure 5.14). The color of the symbols indicates whether recrystallization was observed under the specified conditions, i.e. crystallization temperature and heating rate. While black symbols indicate that no substantial recrystallization was observed, yellow symbols indicate that the material recrystallizes upon heating. Red color of the symbols denotes the transient situation where partial recrystallization was observed.

6 Conclusions and Outlook

The main objective of this work was to optimize and further develop the recently introduced approach combining millisecond time-resolved X-ray micro-diffraction with in-situ fast chip calorimetry and apply it to studies of the multimodal melting behavior of a semirigid chain polymer, polyetheretherketone (PEEK), as a model system.

The results of the work are summarized in two main chapters of the manuscript. Chapter 4 deals with the technical developments and implementations undertaken to optimize and streamline in-situ fast chip calorimetry investigations with simultaneous recording of the structural response using millisecond time-resolved X-ray micro-diffraction, while Chapter 5 summarizes the results and conclusions on the PEEK double melting behavior.

In-situ fast chip calorimetry at the ID13 micro-diffraction setup

In the course of the work, technical challenges concerning the implementation of the setup allowing time-resolved X-ray micro-diffraction with fast chip calorimetry were met and discussed. In order to reach the melting temperature of PEEK the existing version of the nanocalorimeter had to be modified using two different approaches. The first one was the application of an external heating source to generate a constant temperature offset. For this, a commercial heating stage was used. This approach proved to be efficient for ex-situ measurements while problems appeared when trying to comply with special constraints of the ID13 micro-diffraction setup. Therefore, an alternative approach was developed using the internal MEMS heaters to create a constant temperature offset. In this context, a new calibration procedure was implemented to allow for more easy calibration of the employed nanocalorimetry sensors.

Adjustments of the setup and challenges encountered

For the implementation of the nanocalorimetric device into the micro-diffraction set up a series of measures were taken to maximize the signal-to-noise ratio in the micro-diffraction experiments. A pinhole collimation scheme using three TEM apertures of different sizes were applied together with the use of a helium-filled flight tube placed in close vicinity downstream the sample to reduce the parasitic air scattering. In addition, a new triggering scheme was developed to allow precise synchronization of the X-ray detector, beam shutters and nanocalorimeter device.

The problem of radiation damage of PEEK was encountered when utilizing the highly brilliant beam at ID13. The impact of the intense radiation on the crystalline and amorphous phases of PEEK was discussed. It was observed that radiation mainly affects the amorphous regions of PEEK which hinders the ability of the material to recrystallize. It was also shown that short high-flux pulses used in slow heating experiments still caused severe damage to the material. This can be explained by the generation of photoelectron induced radicals when the high intense X-ray beam interacts with organic material. These radicals will trigger chemical reactions in the material even when the X-ray exposure is over. In order to overcome this problem, an exposure scheme was used where the sample was illuminated only during the main structural transition on heating.

Chapter 6 Conclusions and Outlook

Using the optimized and newly implemented setup at ID13 a large number of measurements were performed to study the melting behavior of PEEK by varying the crystallization temperature and applied heating rates. To explore the thermal behavior of PEEK at small heating rates the measurements were conducted using standard DSC and variable temperature X-ray diffraction at the BM26 beamline of the ESRF.

The double melting behavior of PEEK

In the first part of the scientific discussion, interpretations based solely on calorimetric data are presented and the validity and limits of this approach are shown and discussed. In the second part, the results of the combined approach are presented and evaluated.

The double-melting of PEEK accessed by nanocalorimetry

The off-line nanocalorimetry measurements of PEEK were performed using several scanning rates (from 50 to 5000 K/s) and crystallization temperatures (from 170 to 270 °C). Regarding the nanocalorimetry measurements, the key parameters of the nanocalorimetry curves are compared such as onsets of melting peaks and peak temperatures. The technical parameters such as thermal lag and thermal gradients are critically analyzed in order to perform relevant data analysis. Slow DSC measurements with heating rates in the range of 5 to 80 K/min were performed to fill the space of heating rates towards low values and the results obtained by fast scanning calorimetry and by DSC analysis were discussed together.

The nanocalorimetry curves of PEEK are similar to those described in the literature. At first glance, it can be seen that the lower-temperature melting peak strongly depends on the crystallization temperature while the higher-temperature melting peak is largely independent. The linear dependence of the onset of the first melting peak with respect to heating rate was found for heating rates higher than 1000 K/s. In order to correct for this, a time-lag correction was applied to all fast heating runs.

Critical heating rate ($\beta_{crit,I}$)

When corrected values of the first melting peak onsets ($T_m^{on}P(I)$) were plotted versus heating rate it was found that the early part of the curve strongly deviated from the linear behavior. The critical heating rate ($\beta_{crit,I}$) at which the onset of the first melting peak started to be affected by the heating rate was found to be independent of the crystallization temperature and was estimated to be 1000 K/s. Based on this observation the suggestion was put forward that this can be related to the processes taking place in the amorphous phase or in the interfacial zone between the crystal and amorphous phases rather than in the crystalline phase.

Hoffman-Weeks analysis of the first melting peak

The Hoffman-Weeks plot was obtained by plotting $T_m^{on}P(I)$ as a function of crystallization temperature. This allowed evaluating the equilibrium melting temperature. Since $T_m^{on}P(I)$ was found to be dependent on the heating rate, different values of the equilibrium melting temperatures were found. Thus, from the data obtained by heating with the rates higher than $\beta_{crit,I}$ the equilibrium melting temperature was estimated to be 395 °C while taking the data from slow DSC measurements with 5K/min one obtains the value of 420 °C. The existence of this first critical heating rate, i.e. $\beta_{crit,I}$, in PEEK indicates that reorganization processes can occur below the first melting process sets in. However, the fact that this critical heating rate is independent of the crystallization temperature indicates that the reorganization processes do not take place in the crystal phase. Thus, the onset temperature of the first melting peak rather reflects the reorganization taking place below the first melting peak onset, rather than the stability of the initially isothermally formed crystals when heated at subcritical heating rates. This means that the heating rates higher than $\beta_{crit,I}$ should be utilized to extrapolate to the equilibrium melting temperature value.

Hoffman-Weeks analysis of the second melting peak and critical heating rate ($\beta_{crit,II}$)

Considering the onsets of the second melting peak ($T_m^{on}P(II)$) a systematic and consistent variation of the melting temperature with regard to heating rate was observed. However, the magnitude of the effect is different for low and high heating rates. For heating rates as low as 5 K/min a dependence of $T_m^{on}P(II)$ on the heating rate can hardly be observed. At heating rates starting from 20 K/min the second melting peak drifts to lower temperatures with increasing heating rate. This effect becomes less pronounced at higher heating rates. The observations can be explained by the fact that heating with very low heating rates (e.g. 5 K/min) allows the system to reorganize while with increasing of heating rate this reorganization is impeded by reducing the available time to finalize the reorganization process. Thus, $T_m^{on}P(II)$ appears at lower values reflecting the lower stability of the less and less recrystallized material. This downward shift of the second melting peak follows an exponential decay behavior with increasing heating rate converging to the final value of $T_m^{on}P(II)$. As a measure for the critical heating rate when the recrystallization process is significantly suppressed the double of the time constant of the exponential decay was chosen reflecting the situation where more than 85% of the reorganization is suppressed. It is also

worth to note that the magnitude of the onset temperature decrease correlates with the crystallization temperature.

When extrapolating $T_m^{on}P(II)$ to the intersection with the line $T_m = T_c$ in the Hoffman-Weeks plot for the case of a fully recrystallized material, e.g. heating at 5 K/min, the resulting value corresponds to 330 °C. This value is in close agreement with the crystal melting temperature of 335 °C reported in the literature.

Early stages of crystallization in PEEK

In order to critically revise the model of a possible two-stage crystallization taking place during isothermal crystallization of PEEK an experimental approach was designed where the PEEK specimen was subject to isothermal crystallization for different crystallization times. The resulting partially crystallized samples were then subject to fast heating calorimetric measurements. When the sample is heated at heating rates higher than the critical value both melting peaks appear simultaneously on the nanocalorimetry curve even in the very early stages of the crystallization process. From this observation, the idea of a two-stage crystallization seems unreasonable since the recrystallization process occurs during heating and its suppression depends on the heating rate applied.

The recrystallization diagram for PEEK

From the temperature evolution of the second melting peak onset, a first recrystallization diagram for PEEK was generated as a function of temperature. The diagram shows the transition from the situation where the recrystallization occurs during heating to the situation where this is suppressed. Thus for crystallization temperatures between 170 °C and 190 °C the critical heating rate is between 1000 and 2000 K/s, while it decreases to about 500 K/s for the temperature of 250 °C. For higher crystallization temperatures the critical heating rate decreases further. However, since the accurate determination of $T_m^{on}P(II)$ is more difficult with the increase of the crystallization temperature for the reason of merging of both melting peaks together, an alternative approach should be found to estimate the presence of the reorganization process.

Structural signature of the PEEK recrystallization during heating

When it comes to the combined approach of nanocalorimetry with simultaneous X-ray micro-diffraction the structural signature of the recrystallization of PEEK during heating was identified by conducting in-situ heating experiments far below the critical heating rate which was derived from the calorimetric data gathered before.

The structural signature of recrystallization was identified as a reduction of the lattice a -parameter setting in with the onset of the final melting transition. This reduction of the a -parameter is connected to the fact that the "equilibrium" lattice parameters decrease with increasing isothermal crystallization temperature. This "equilibrium" lattice parameters describe the unit cell of PEEK when measured at the same temperature at which it was crystallized.

Having the information on the recrystallization signature experiments combining fast chip calorimetry in-situ with X-ray micro-diffraction was conducted to follow the recrystallization process at varying heating rates ranging from 50 to 2000 K/s for PEEK isothermally crystallized in the temperature range from 190 to 300 °C. In order to complete the picture, the information from the in-situ fast heating experiments were complemented with slow heating experiments conducted at the BM26 beamline covering variable temperature X-ray diffraction experiments for heating rates comprised between 5 and 80 K/min.

Combining all the experimental data it was found that with the increase of the heating rate as well as with increasing crystallization temperature a decrease of the recrystallization tendency can be observed. Furthermore, the critical heating rate for each crystallization temperature could be identified above which the recrystallization process is suppressed. However, it should be mentioned that there is no sharp transition between the two regimes.

Based on these findings, the recrystallization diagram for PEEK was drawn using the combined approach. Comparing the results from both approaches it could be concluded that for low crystallization temperatures, where both melting peaks are well separated in the temperature domain, nanocalorimetry is sufficient to predict the critical heating rate above which the recrystallization is suppressed. However, for high crystallization temperatures, this approach starts to become insufficient due to convolution of both melting peaks. This makes additional structural information compulsory.

Combining the information collected from all the experiments a general assessment of the complex melting behavior for isothermally crystallized PEEK can be made. Thus it appears that the complex melting behavior cannot be explained solely by one of the initially proposed causes, i.e. melting and subsequent recrystallization upon heating, existence of multiple crystal populations generated during isothermal crystallization, or by the biased sequential melting, but is a rather a complex combination of several factors and processes taking place during heating.

Based on the nanocalorimetric measurements it can be shown that there are two critical heating rates observable on heating of isothermally crystallized PEEK. While the first critical heating rate $\beta_{crit,I}$ is connected to the low-temperature melting peak the second critical heating rate $\beta_{crit,II}$ is connected to the behavior of the second melting peak. Thus, $\beta_{crit,I}$ marks the critical heating rate above which the first melting peak correlates with the stability of the initially crystallized crystals. This conclusion is drawn from the fact that the extrapolation of the first melting peak onset toward the $T_c = T_m$ line in the Hoffmann-Weeks plot gives the established equilibrium melting temperature for PEEK of 395 °C for the values derived with the above critical heating rates. On the other hand, the second critical heating rate in PEEK, $\beta_{crit,II}$ correlates to the condition above which no recrystallization can be observed in PEEK, based on structural information. The fact that the ratio of both melting peak onsets as a function of the crystallization temperature reveals a strict linear behavior indicates that at the heating rates above the critical one, both melting peaks are the signature of the same initially formed crystals rather than caused by melting of independent crystal populations as sometimes stated in the literature.

Another remarkable conclusion is that for isothermally crystallized PEEK heated above $\beta_{crit,II}$, where the recrystallization is suppressed, the double melting behavior is still observed. Therefore, alternative mechanisms explaining the double melting in PEEK have to be explored, e.g. the biased sequential melting of crystals. In order to evaluate if the biased sequential melting model can be applied to PEEK, information concerning the morphological evolution during fast heating is essential. Hence, an experiment combining fast chip calorimetry combined with millisecond time-resolved small-angle X-ray scattering would be a promising candidate for the continuation of the current project.

Outlook

When thinking about future applications of this approach combining these two complementary methodologies to shed light on long-standing debates, or to explore novel materials under extreme but also industrially and technologically relevant conditions, the underlying contradiction in requirements for these both methodologies appears detrimental. The fact that for the application of higher heating rates, the sample mass has to be reduced further, seems to be in contradiction with the need of sufficient scattering volume, needed to generate a viable scattering signal. As realized in the course of the conducted project it seems that the applied heating rates in the order a few thousand Kelvin per second mark the limit of what can be technically done at the moment. Even if acquisition rates of new detectors could be increased by an order of magnitude or more, the intensity of the scattering signal is the limiting factor.

However, with the upcoming upgrade of the ESRF to become a fourth-generation synchrotron radiation source - ESRF-EBS¹⁶³ (Extremely Brilliant Source), new exciting possibilities arise. The very fact that the brilliance of the beam will increase by a factor of 30 - 50 for the ID13 beamline, not even considering possible further upgrades of the beamline, opens a large window of opportunities for the combination of complementary methodologies. Together with the development of faster and more sensitive detectors that can operate in the 10 to 100 kHz regime, the increased brilliance would allow for acquisition times close to the μ s range for weak scattering materials such as bio-materials and bio-polymers.

However, the projected increase in flux density will come at a price. In future experiments using the EBS beam, radiation induced damage will become a growing issue. Yet, applying smart data acquisition regimes combined with novel sample delivery and conditioning systems such as liquid jets and droplet generators, inspired by developments at X-ray free electron lasers (X-FEL) where at any moment in time a new freshly conditioned sample will be delivered to the probing location, would allow circumventing the accumulation radiation damage.

Facing this leap in beam flux intensity it might come in reach to combine the fast heating capability with high-resolution scanning and μ s time-resolved nano-diffraction. Thus, it would be possible to follow fast structural changes in heterogeneous materials with unprecedented spatial and temperature resolution in real time. Consequently, the new source

will allow exploring fast structural transitions and metastable phases in flexible polymers such as polyethylene or even metals with unprecedented time resolution. Thus, mimicking industrially relevant processes for in-situ experiments, for instance, related to additive manufacturing such as laser sintering of metals and other materials, will become possible. Also, with such an increase in photon flux together with the reduction of the size of the X-ray source, the generation of low divergence micro-beams appears to be well feasible. Then, the design of fast chip calorimetry experiments combined with low-q micro-beam SAXS would allow addressing a whole new world of open issues in the macromolecular physics world and beyond.

7 References

1. Furushima Y, Toda A, Rousseaux V, Bailly C, Zhuravlev E, Schick C. Quantitative understanding of two distinct melting kinetics of an isothermally crystallized poly(ether ether ketone). *Polym (United Kingdom)*. 2016. doi:10.1016/j.polymer.2016.07.005
2. Strobl G. The physics of polymers. *Polymer (Guildf)*. 1974;15(5):258. doi:10.1016/0032-3861(74)90120-7
3. Storks KH. An Electron Diffraction Examination of Some Linear High Polymers. *J Am Chem Soc*. 1938;60(8):1753-1761. doi:10.1021/ja01275a013
4. Herrmann K. Zur röntgenographischen Strukturereforchung. 1930:371-394.
5. Flory PJ. On the Morphology of the Crystalline State in Polymers. *J Am Chem Soc*. 1962;84(15):2857-2867. doi:10.1021/ja00874a004
6. Zachmann HG. Statistische Thermodynamik des Kristallisierens und Schmelzens von hochpolymeren Stoffen. *Kolloid-Zeitschrift Zeitschrift für Polym*. 1969;231(1-2):504-534. doi:10.1007/BF01500013
7. Geil PH. Polymer deformation. II. Drawing of polyethylene single crystals. *J Polym Sci Part A Gen Pap*. 1964;2(9):3813-3833. doi:10.1002/pol.1964.100020901
8. Zhang M, Guo B-H, Xu J. *A Review on Polymer Crystallization Theories*. Vol 7.; 2016. doi:10.3390/cryst7010004
9. Keller A, O'Connor A. Large periods in polyethylene: The origin of low-angle x-ray scattering [27]. *Nature*. 1957;180(4597):1289-1290. doi:10.1038/1801289a0
10. Jaccodine R. Observations of spiral growth steps in ethylene polymer [4]. *Nature*. 1955;176(4476):305-306. doi:10.1038/176305b0
11. Till PH. The Growth of Single Crystals of Linear Polyethylene. *J Polym Sci*. 1957;XXIV(106):21-21. doi:10.2307/j.ctt46nrxb.16
12. Keller A. Polymer crystals. *Rep Prog Phys*. 1968;31:623. doi:10.1088/0034-4885/77/5/056502
13. Flory PJ. The configuration of real polymer chains. *J Chem Phys*. 1949;17(3):303-310. doi:10.1063/1.1747243
14. De Gennes PG. Reptation of a polymer chain in the presence of fixed obstacles. *J Chem Phys*. 1971;55(2):572-579. doi:10.1063/1.1675789
15. De Gennes P-G. *Scaling Concepts in Polymer Physics*. NY, USA: Cornell University Press: Ithaca; 1979.
16. Dargazany R, Khiêm VN, Poshtan EA, Itskov M. Constitutive modeling of strain-induced crystallization in filled rubbers. *Phys Rev E - Stat Nonlinear, Soft Matter Phys*. 2014;89(2):1-12. doi:10.1103/PhysRevE.89.022604
17. Dettenmaier M, Fischer EW, Stamm M. Calculation of small-angle neutron scattering by macromolecules in the semicrystalline state. *Colloid Polym Sci Kolloid Zeitschrift Zeitschrift für Polym*. 1980;258(3):343-349. doi:10.1007/BF01466672
18. Flory PJ, Yeung Yoon D. Molecular morphology in semicrystalline polymers. *Nature*. 1978;272:226-229. <https://www.nature.com/articles/272226a0.pdf>. Accessed November 29, 2018.

-
19. Ballard DGH, Cheshire P, Longman GW, Schelten J. Small-angle neutron scattering studies of isotropic polypropylene. *Polymer (Guildf)*. 1978;19(4):379-385. doi:10.1016/0032-3861(78)90241-0
 20. Schelten J, Ballard DGH, Wignall GD, Longman G, Schmatz W. Small-angle neutron scattering studies of molten and crystalline polyethylene. *Polymer (Guildf)*. 1976;17(9):751-757. doi:10.1016/0032-3861(76)90028-8
 21. Hoffman JD, Lauritzen JI. Crystallization of bulk polymers with chain folding: theory of growth of lamellar spherulites. *J Res Natl Bur Stand Sect A Phys Chem*. 1961;65A(4):297. doi:10.6028/jres.065a.035
 22. Muthukumar M. *Advances in Chemical Physics - Google Books*. Vol 128.; 2004. <http://books.google.com/books?hl=en&lr=&id=wK3Vhq-VnBQC&oi=fnd&pg=PA1&dq=NUCLEATION+IN+POLYMER+CRYSTALLIZATION&ots=GbLESFj-e7&sig=lBx-kwms5p3pMr-p3Xx2pr9rmDI%5Cnpapers2://publication/uuid/FD9A3B13-46D0-4499-B8DC-A961D197F820>.
 23. Nishi M, Hikosaka M, Ghosh SK, Toda A, Yamada K. Molecular Weight Dependence of Primary Nucleation Rate of Polyethylene I. An Extended Chain Single Crystal. *Polym J*. 1999;31(9):749-758. doi:10.1017/CBO9781107415324.004
 24. Lu J, Huang R, Li L, Luo J. Growth of large polymer extended-chain single crystals in a poly(ethylene terephthalate)/bisphenol A polycarbonate blend under high pressure. *Macromol Rapid Commun*. 2005;26(18):1478-1482. doi:10.1002/marc.200500346
 25. Organ S, Keller A. Solution crystallization of polyethylene at high temperatures. *J Mater Sci*. 1985;20:1602-1615. doi:10.1007/BF00555261
 26. Keller A, Ungar G. Radiation effects and crystallinity in polyethylene. *Radiat Phys Chem*. 1983;22(1-2):155-181. doi:10.1016/0146-5724(83)90201-7
 27. Canetti M, Bertini F, Scavia G, Porzio W. Structural investigation on bulk poly(3-hexylthiophene): Combined SAXS, WAXD, and AFM studies. *Eur Polym J*. 2009;45(9):2572-2579. doi:10.1016/j.eurpolymj.2009.06.012
 28. Yamada K, Hikosaka M, Toda A, Yamazaki S, Tagashira K. Equilibrium melting temperature of isotactic polypropylene with high tacticity. 2. Determination by optical microscopy. *Macromolecules*. 2003;36(13):4802-4812. doi:10.1021/ma021207a
 29. Hoffman JD, Weeks JJ. Melting process and the equilibrium melting temperature of polychlorotrifluoroethylene. *J Res Natl Bur Stand Sect A Phys Chem*. 1962;66A(1):13. doi:10.6028/jres.066a.003
 30. Avramov I. Kinetics of distribution of infections in networks. *Phys A Stat Mech its Appl*. 2007;379(2):615-620. doi:10.1016/j.physa.2007.02.002
 31. Avrami M. Kinetics of phase change. I: General theory. *J Chem Phys*. 1939;7(12):1103-1112. doi:10.1063/1.1750380
 32. Avrami M. Kinetics of phase change. II Transformation-time relations for random distribution of nuclei. *J Chem Phys*. 1940;8(2):212-224. doi:10.1063/1.1750631
 33. Avrami M. Granulation, phase change, and microstructure kinetics of phase change. III. *J Chem Phys*. 1941;9(2):177-184. doi:10.1063/1.1750872
 34. HAY JN. Application of the modified Avrami equations to polymer crystallisation kinetics. *Brit Polym J*. 1971;3(2):74-82.
 35. Choi HW, Kim YH, Rim YH, Yang YS. Crystallization kinetics of lithium niobate glass: Determination of the Johnson-Mehl-Avrami-Kolmogorov parameters. *Phys Chem Chem Phys*. 2013;15(24):9940-9946. doi:10.1039/c3cp50909e

Chapter 7 References

36. Grenier D, Prud Homme RE'. Avrami analysis: Three experimental limiting factors. *J Polym Sci Polym Phys Ed.* 1980;18(7):1655-1657. doi:10.1002/pol.1980.180180715
37. Wang RY, Zou SF, Jiang BY, et al. A Generalized Avrami Equation for Crystallization Kinetics of Polymers with Concomitant Double Crystallization Processes. *Cryst Growth Des.* 2017;17(11):5908-5917. doi:10.1021/acs.cgd.7b01016
38. Tardif X, Pignon B, Boyard N, et al. Experimental study of crystallization of PolyEtherEtherKetone (PEEK) over a large temperature range using a nano-calorimeter. *Polym Test.* 2014;36:10-19. doi:10.1016/j.polymertesting.2014.03.013
39. Lee Y, Porter RS. Double-melting behavior of poly(ether ether ketone). *Macromolecules.* 1987. doi:10.1021/ma00172a028
40. Rim PB, Runt JP. Melting Behavior of Crystalline/Compatible Polymer Blends: Poly(ϵ -caprolactone)/Poly(styrene-co-acrylonitrile). *Macromolecules.* 1983;16(5):762-768. doi:10.1021/ma00239a012
41. Yagfarov MS. Recrystallization phenomena in high molecular weight compounds and their role in the dynamics of melting. *Polym Sci USSR.* 1982;24(12):2915-2922. doi:10.1016/0032-3950(82)90244-1
42. Yagfarov MS, Mitrofanova EP. Recrystallization and secondary crystallization in polymers. *Polym Sci USSR.* 1986;28(5):1011-1017. doi:10.1016/0032-3950(86)90246-7
43. Statton WO, Geil PH. Recrystallization of polyethylene during annealing. *J Appl Polym Sci.* 1960;3(9):357-361. doi:10.1002/app.1960.070030913
44. Heck B, Siegenführ S, Strobl G, Thomann R. A law controlling polymer recrystallization showing up in experiments on s-polypropylene. *Polymer (Guildf).* 2007;48(5):1352-1359. doi:10.1016/j.polymer.2007.01.025
45. Boettinger WJ, Kattner UR, Moon K-W, Perepezko JH. DTA and Heat-Flux DSC Measurements of Alloy Melting and Freezing. *Natl Inst Stand Technol.* 2006;(Spec. Publ. 960-15):151-221. doi:10.1016/b978-008044629-5/50005-7
46. Hickey AJ, Giovagnoli S. Pharmaceutical Powder and Particles. 2018:43-53. doi:10.1007/978-3-319-91220-2
47. Demetzos C, Pippa N. *Thermodynamics and Biophysics of Biomedical Nanosystems.*; 2019. doi:10.1007/978-981-13-0989-2
48. Wunderlich B, Wunderlich B. *Thermal Analysis of Polymeric Materials - Bernhard Wunderlich - 2005.Pdf.*
49. Investigation of Polymers with Differential Scanning Calorimetry. In: *HUMBOLDT UNIVERSITÄT ZU BERLIN.* <https://polymerscience.physik.hu-berlin.de/docs/manuals/DSC.pdf>.
50. Balani K, Verma V, Agarwal A, Narayan R. Physical, Thermal, and Mechanical Properties of Polymers. *Biosurfaces.* 2015:329-344. doi:10.1002/9781118950623.app1
51. Wrasidlo W. Transitions and Relaxations in Aromatic Polymers. *J Polym Sci Part A-2 Polym Phys.* 1971;9:1603-1627.
52. Queen DR, Hellman F. Thin film nanocalorimeter for heat capacity measurements of 30 nm films. *Rev Sci Instrum.* 2009;80(6). doi:10.1063/1.3142463
53. Allen LH, Ramanath G, Lai SL, et al. 1 000 000°C/s thin film electrical heater: In situ resistivity measurements of Al and Ti/Si thin films during ultra rapid thermal annealing. *Appl Phys Lett.* 1994;64(4):417-419. doi:10.1063/1.111116
54. Yi F, La Van DA. Nanoscale thermal analysis for nanomedicine by nanocalorimetry. *Wiley*

-
- Interdiscip Rev Nanomedicine Nanobiotechnology*. 2012;4(1):31-41. doi:10.1002/wnan.155
55. Swaminathan P, Burke BG, Holness AE, et al. Optical calibration for nanocalorimeter measurements. *Thermochim Acta*. 2011;522(1-2):60-65. doi:10.1016/j.tca.2011.03.006
 56. Schick C, Mathot VBF. *Fast Scanning Calorimetry*. Springer; 2016. doi:10.3139/9781569906446.008
 57. Olson EA, Efremov MY, Zhang M, Zhang Z, Allen LH. The design and operation of a MEMS differential scanning nanocalorimeter for high-speed heat capacity measurements of ultrathin films. *J Microelectromechanical Syst*. 2003;12(3):355-364. doi:10.1109/JMEMS.2003.811755
 58. Minakov AA, Adamovsky SA, Schick C. Non-adiabatic thin-film (chip) nanocalorimetry. *Thermochim Acta*. 2005;432(2):177-185. doi:10.1016/j.tca.2005.01.073
 59. Lai SL, Ramanath G, Allen LH, Infante P, Ma Z. High-speed (10^4 °C/s) scanning microcalorimetry with monolayer sensitivity (J/m^2). *Appl Phys Lett*. 1995;67(1995):1229. doi:10.1063/1.115016
 60. Zhang M, Efremov MY, Schiettekatte F, et al. Size-dependent melting point depression of nanostructures: Nanocalorimetric measurements. *Phys Rev B - Condens Matter Mater Phys*. 2000;62(15):10548-10557. doi:10.1103/PhysRevB.62.10548
 61. Kwan AT, Efremov MY, Olson EA, et al. Nanoscale calorimetry of isolated polyethylene single crystals. *J Polym Sci Part B Polym Phys*. 2001;39(11):1237-1245. doi:10.1002/polb.1097
 62. Grapes MD, Santala MK, Campbell GH, LaVan DA, Weihs TP. A detailed study of the Al₃Ni formation reaction using nanocalorimetry. *Thermochim Acta*. 2017;658:72-83. doi:10.1016/j.tca.2017.10.018
 63. Yi F, Stevanovic A, Osborn WA, Kolmakov A, LaVan DA. A multi-environment nanocalorimeter with electrical contacts for use in a scanning electron microscope. *Mater Horizons*. 2017;4(6):1128-1134. doi:10.1039/c7mh00513j
 64. Yi F, Delisio JB, Zachariah MR, LaVan DA. Nanocalorimetry-Coupled Time-of-Flight Mass Spectrometry: Identifying Evolved Species during High-Rate Thermal Measurements. *Anal Chem*. 2015;87(19):9740-9744. doi:10.1021/acs.analchem.5b01872
 65. Lee W, Fon W, Axelrod BW, Roukes ML. High-sensitivity microfluidic calorimeters for biological and chemical applications. *Proc Natl Acad Sci*. 2009;106(42):18040-18040. doi:10.1073/pnas.0910577106
 66. Torres FE, Kuhn P, Bruyker D De, et al. Enthalpy arrays. *PNAS*. 2004;101(26):9517-9522. <http://www.pnas.org/content/101/26/9517.full.pdf%5Cnpapers2://publication/uuid/1F09773E-50D7-45A2-933B-2FF1B5E2E3D9>.
 67. Recht MI, Bruyker D De, Bell AG, et al. Enthalpy array analysis of enzymatic and binding reactions. *Anal Biochem*. 2008;377(1):33-39. doi:10.1016/j.ab.2008.03.007
 68. Chancellor EB, Wikswo JP, Baudenbacher F, Radparvar M, Osterman D. Heat conduction calorimeter for massively parallel high throughput measurements with picoliter sample volumes. *Appl Phys Lett*. 2004;85(12):2408-2410. doi:10.1063/1.1790075
 69. McCluskey PJ, Xiao K, Gregoire JM, Dale D, Vlassak JJ. Application of in-situ nano-scanning calorimetry and X-ray diffraction to characterize Ni-Ti-Hf high-temperature shape memory alloys. *Thermochim Acta*. 2015;603:53-62. doi:10.1016/j.tca.2014.07.023
 70. Gregoire JM, Xiao K, McCluskey PJ, Dale D, Cuddalorepatta G, Vlassak JJ. In-situ X-ray diffraction combined with scanning AC nanocalorimetry applied to a Fe_{0.84}Ni_{0.16} thin-film sample. *Appl Phys Lett*. 2013;102(20):100-103. doi:10.1063/1.4806972
 71. Willa K, Diao Z, Campanini D, et al. Nanocalorimeter platform for in situ specific heat measurements and x-ray diffraction at low temperature. *Rev Sci Instrum*. 2017;88(12).

Chapter 7 References

- doi:10.1063/1.5016592
72. Pannetier J. Powder diffraction techniques. In: Baruchel J, Hodeau JL, Lehmann MS, Regnard JR, Schlenker C, eds. *Neutron and Synchrotron Radiation for Condensed Matter Studies*. Springer; 1994:444.
 73. Pecharsky VK, Zavalij PY. *Fundamentals of Powder Diffraction and Structural Characterization of Materials.*; 2005.
 74. Murthy NS. X-ray diffraction from polymers. *Polym Morphol Princ Charact Process*. 2016;14-36. doi:10.1002/9781118892756.ch2
 75. David WIF, Shankland K, McCusker LB, Baerlocher C. Structure Determination from Powder Diffraction Data. *Struct Determ from Powder Diffr Data*. 2010;9780199205:1-360. doi:10.1093/acprof:oso/978019920530.001.0001
 76. Langford JI. A rapid method for analysing the breadths of diffraction and spectral lines using the Voigt function. *J Appl Crystallogr*. 1978;11(1):10-14. doi:10.1107/s0021889878012601
 77. Langford JI, Wilson AJC. Seherrer after Sixty Years: A Survey and Some New Results in the Determination of Crystallite Size. *J Appl Cryst*. 1978;11:102-113. doi:10.1061/9780784479896.140
 78. Murthy NS, Minor H. General procedure for evaluating amorphous scattering and crystallinity from X-ray diffraction scans of semicrystalline polymers. *Polymer (Guildf)*. 1989;31:996-1002.
 79. Hermans PH, Weidinger A. Estimation of crystallinity of some polymers from x-ray intensity measurements. *J Polym Sci*. 1949;4(6):709-723. doi:10.1002/pol.1949.120040604
 80. Mo Z, Zhang H. The Degree of Crystallinity in Polymers by Wide-Angle X-Ray Diffraction (WAXD). *J Macromol Sci Part C*. 1995;35(4):555-580. doi:10.1080/15321799508021751
 81. Murthy NS, Minor H, Bednarczyk C, Krimm S. Structure of the Amorphous Phase in Oriented Polymers. *Macromolecules*. 1993;26(7):1712-1721. doi:10.1021/ma00059a034
 82. Scheme of storage ring, ESRF. <http://www.esrf.fr/about/synchrotron-science/synchrotron>.
 83. Eiger 4M, Dectris. <https://www.dectris.com/products/eiger/eiger-x-for-synchrotron/details/eiger-x-4m>.
 84. Attwood TE, Dawson PC, Freeman JL, Hoy LRJ, Rose JB, Staniland PA. Synthesis and properties of polyaryletherketones. *Polymer (Guildf)*. 1981;22(8):1096-1103. doi:10.1016/0032-3861(81)90299-8
 85. Kurtz SM. *An Overview of PEEK Biomaterials*. Elsevier Inc.; 2012. doi:10.1016/B978-1-4377-4463-7.10001-6
 86. Dawson PC, Blundell DJ. X-ray data for poly(aryl ether ketones). *Polymer (Guildf)*. 1980;21(5):577-578. doi:10.1016/0032-3861(80)90228-1
 87. Atkinson JR, Hay JN, Jenkins MJ. Enthalpic relaxation in semi-crystalline PEEK. *Polymer (Guildf)*. 2001;43(3):731-735. doi:10.1016/S0032-3861(01)00668-1
 88. Jonas A, Legras R. Relation between PEEK Semicrystalline Morphology and Its Subglass Relaxations and Glass Transition. *Macromolecules*. 1993;26(4):813-824. doi:10.1021/ma00056a036
 89. Cebe P, Chung SY, Hong S -D. Effect of thermal history on mechanical properties of polyetheretherketone below the glass transition temperature. *J Appl Polym Sci*. 1987;33(2):487-503. doi:10.1002/app.1987.070330217
 90. Cebe P, Hong SD. Crystallization behaviour of poly(ether-ether-ketone). *Polymer (Guildf)*. 1986;27(8):1183-1192. doi:10.1016/0032-3861(86)90006-6

-
91. Lee Y, Porter RS. Effects of Thermal History on Crystallization of Poly(ether ether ketone) (PEEK). *Macromolecules*. 1988;21(9):2770-2776. doi:10.1021/ma00187a022
 92. Blundell DJ, Osborn BN. The morphology of poly(aryl-ether-ether-ketone). *Polymer (Guildf)*. 1983;24(8):953-958. doi:10.1016/0032-3861(83)90144-1
 93. Kumar S, Anderson DP, Adams WW. Crystallization and morphology of poly(aryl-ether-ether-ketone). *Polymer (Guildf)*. 1986. doi:10.1016/0032-3861(86)90145-X
 94. Fratini A V., Cross EM, Whitaker RB, Adams WW. Refinement of the structure of PEEK fibre in an orthorhombic unit cell. *Polymer (Guildf)*. 1986;27(6):861-865. doi:10.1016/0032-3861(86)90295-8
 95. Blundell DJ, D'Mello J. Variations in the crystal lattice of PEEK and related para-substituted aromatic polymers: 2. Effect of sequence and proportion of ether and ketone links. *Polymer (Guildf)*. 1991. doi:10.1016/0032-3861(91)90018-E
 96. Jin L, Ball J, Bremner T, Sue H-J. Crystallization behavior and morphological characterization of poly(ether ether ketone). *Polymer (Guildf)*. 2014;55(20):5255-5265. doi:10.1016/j.polymer.2014.08.045
 97. Hay JN, Langford JI, Lloyd JR. Variation in unit cell parameters of aromatic polymers with crystallization temperature. *Polymer (Guildf)*. 1989;30(3):489-493. doi:10.1016/0032-3861(89)90019-0
 98. Wakelyn NT. Variation of Unit Cell Parameters of Poly(Arylene Ether Ether Ketone) Film With Annealing Temperature. *J Polym Sci Part C Polym Lett*. 1987;25(1):25-28. doi:10.1002/pol.1987.140250105
 99. Blundell DJ, D 'mello J. Variations in the crystal lattice of PEEK and related para-substituted aromatic polymers: 1. Thermal expansion.
 100. Blundell DJ. On the interpretation of multiple melting peaks in poly(ether ether ketone). *Polymer (Guildf)*. 1987;28(13):2248-2251. doi:10.1016/0032-3861(87)90382-X
 101. Mehmet-Alkan AA, Hay JN. The crystallinity of poly(ether ether ketone). *Polymer (Guildf)*. 1992;33(16):3527-3530. doi:10.1016/0032-3861(92)91116-J
 102. Lee Y, Porter RS, Lin JS. On the Double-Melting Behavior of Poly(ether ether ketone). *Macromolecules*. 1989;22(4):1756-1760. doi:10.1021/ma00194a043
 103. Holdsworth PJ, Turner-Jones A. The melting behaviour of heat crystallized poly(ethylene terephthalate). *Polymer (Guildf)*. 1971;12(3):195-208. doi:10.1016/0032-3861(71)90045-0
 104. Krüger KN, Zachmann HG. Investigation of the Melting Behavior of Poly(aryl ether ketones) by Simultaneous Measurements of SAXS and WAXS Employing Synchrotron Radiation. *Macromolecules*. 1993;26(19):5202-5208. doi:10.1021/ma00071a035
 105. Groeninckx G, Reynaers H. Morphology and melting behavior of semicrystalline poly(ethylene terephthalate). II. Annealed PET. *J Polym Sci Polym Phys Ed*. 1980;18(6):1325-1341. doi:10.1002/pol.1980.180180613
 106. Jonas AM, Russell TP, Yoon DY. *Synchrotron X-Ray Scattering Studies of Crystallization of Poly(Ether-Ether-Ketone) from the Glass and Structural Changes during Subsequent Heating-Cooling Processes*. Vol 28.; 1995. <https://pubs.acs.org/sharingguidelines>. Accessed November 21, 2018.
 107. Fakirov S, Fischert EW, Hoffmann R, Schmidt GF. Structure and properties of poly(ethylene terephthalate) crystallized by annealing in the highly oriented state: 2.Melting behaviour and the mosaic block structure of the crystalline layers. *Polymer (Guildf)*. 1977;18(1):1121-1129.
 108. Ivanov DA, Legras R, Jonas AM. The crystallization of poly(aryl-ether-ether-ketone) (PEEK): Reorganization processes during gradual reheating of cold-crystallized samples. *Polymer (Guildf)*. 2000;41(10):3719-3727. doi:10.1016/S0032-3861(99)00549-2

Chapter 7 References

109. Ivanov DA, Jonas AM. A comparison of the alpha-relaxation of amorphous poly(aryl-ether-ether-ketone) (PEEK) probed by dielectric and dynamic mechanical analysis. *Polymer (Guildf)*. 1998;39(15):3577-3581. doi:http://dx.doi.org/10.1016/S0032-3861(97)10267-1
110. Al-Hussein M, Strobl G. The mechanisms of recrystallization after melting in syndiotactic polypropylene and isotactic polystyrene. *Eur Phys J E*. 2001;6(4):305-314. doi:10.1007/s10189-001-8045-5
111. Ivanov DA, Hocquet S, Dosi re M, Koch MHJ. Exploring the melting of a semirigid-chain polymer with temperature-resolved small-angle X-ray scattering. *Eur Phys J E*. 2004;13(4):363-378. doi:10.1140/epje/i2003-10082-x
112. Bair HE, Salovey R, Huseby TW. Melting and Annealing of Polyethylene single crystals. *Polymer (Guildf)*. 1967;8(9).
113. Roberts RC. Poly(ethylene terephthalate) II - Morphological Changes on Annealing. *Polymer (Guildf)*. 1969;10:117-125.
114. Zachmann HG, Schmidt GF. Schmelz und Kristallisationserscheinungen bei makromolekularen Substanzen. *Macromol Chem*. 1962;52:23-36.
115. Hughes MA, Sheldon RP. Some Thermal Studies on Poly(ethylene terephthalate). *J Appl Polym Sci*. 1964;8:1541-1548.
116. Kim HG, Robertson RE. A new approach for estimating the recrystallization rate and equilibrium melting temperature. *J Polym Sci Part B Polym Phys*. 1998;36(1):133-141. doi:10.1002/(SICI)1099-0488(19980115)36:1<133::AID-POLB15>3.0.CO;2-D
117. Bassett DC, Olley RH, Al Raheil IAM. On crystallization phenomena in PEEK. *Polymer (Guildf)*. 1988;29(10):1745-1754. doi:10.1016/0032-3861(88)90386-2
118. Lu SX, Cebe P, Capel M. Thermal stability and thermal expansion studies of PEEK and related polyimides. *Polymer (Guildf)*. 1996;37(14):2999-3009. doi:10.1016/0032-3861(96)89397-9
119. Bell JP, Murayama T. Relations between dynamic mechanical properties and melting behavior of nylon 66 and poly(ethylene terephthalate). *J Polym Sci Part A-2 Polym Phys*. 1969;7(6):1059-1073. doi:10.1002/pol.1969.160070607
120. Marand H, Prasad A. On the Observation of a New Morphology in Poly(arylene ether ether ketone). A Further Examination of the Double Endothermic Behavior of Poly(arylene ether ether ketone). *Macromolecules*. 1992;25(6):1731-1736. doi:10.1021/ma00032a017
121. Verma R, Marand H, Hsiao B. Morphological Changes during Secondary Crystallization and Subsequent Melting in Poly(ether ether ketone) as Studied by Real Time Small Angle X-ray Scattering. *Macromolecules*. 1996;29(24):7767-7775. doi:10.1021/ma951727o
122. Lovinger AJ, Davis DD. Electron-microscopic investigation of the morphology of a melt-crystallized polyaryletherketone. *J Appl Phys*. 1985;58(8):2843-2853. doi:10.1063/1.335856
123. Lovinger AJ, Davis DD. Solution Crystallization of Poly(ether ether ketone). *Macromolecules*. 1986;19(7):1861-1867. doi:10.1021/ma00161a014
124. Ko TY, Woo EM. Changes and distribution of lamellae in the spherulites of poly(ether ether ketone) upon stepwise crystallization. *Polymer (Guildf)*. 1996;37(7):1167-1175. doi:10.1016/0032-3861(96)80843-3
125. Lattimer MP, Hobbs JK, Hill MJ, Barham PJ. On the origin of the multiple endotherms in PEEK. *Polymer (Guildf)*. 1992;33(18):3971-3973.
126. Imberty A, Perez S. A revisit to the three-dimensional structure of B-type starch. *Biopolymers*. 1988. doi:10.1002/bip.360270803

-
127. Verma RK, Velikov V, Kander RG, Marand H, Chu B, Hsiao BS. SAXS studies of lamellar level morphological changes during crystallization and melting in PEEK. *Polymer (Guildf)*. 1996;37(24):5357-5365. doi:10.1016/S0032-3861(96)00387-4
 128. Cheng SZD, Cao MY, Wunderlich B. Glass Transition and Melting Behavior of Poly(oxy-1,4-phenyleneoxy-1,4-phenylenecarbonyl-1,4-phenylene). *Macromolecules*. 1986;19(7):1868-1876. doi:10.1021/ma00161a015
 129. Marand H, Alizadeh A, Farmer R, Desai R, Velikov V. Influence of structural and topological constraints on the crystallization and melting behavior of polymers. 2. Poly(arylene ether ether ketone). *Macromolecules*. 2000;33(9):3392-3403. doi:10.1021/ma9913562
 130. Tan S, Su A, Luo J, Zhou E. Crystallization kinetics of poly (ether ether ketone)(PEEK) from its metastable melt. *Polymer (Guildf)*. 1999;40(5):1223-1231. doi:10.1016/S0032-3861(98)00275-4
 131. Wang J, Alvarez M, Li Y, et al. Synchrotron Small-angle X-ray Scattering Study of Crystalline Structures and Isothermal Crystallization Kinetics of Poly(aryl ether ether ketones). *Macromolecules*. 1992;25(25):6943-6951. doi:10.1021/ma00051a035
 132. Hsiao BS, Gardner KH, Wu DQ. Time-resolved X-ray study of poly(aryl ether ether ketone) crystallization and melting behaviour: 2. Melting. *Polymer (Guildf)*. 1993;34(19):3996-4003. doi:10.1007/978-94-011-1950-4_37
 133. Hsiao BS, Sauer BB, Verma RK, et al. New Insight of Isothermal Melt Crystallization in Poly(aryl ether ether ketone) via Time-Resolved Simultaneous Small-Angle X-ray Scattering/Wide-Angle X-ray Diffraction Measurements. *Macromolecules*. 1995;28(20):6931-6936. doi:10.1021/ma00124a032
 134. Fournies C, Damman P, Dosière M, Koch MHJ. Time-Resolved SAXS, WAXS, and DSC Study of Melting of Poly(aryl ether ether ketone) (PEEK) Annealed from the Amorphous State. *Macromolecules*. 1996;30:1392-1399.
 135. Medellín-Rodríguez FJ, Phillips PJ, Lin JS. Melting behavior of high-temperature polymers. *Macromolecules*. 1996;29(23):7491-7501. doi:10.1021/ma9511659
 136. Sauer BB, Kampert WG, Neal Blanchard E, Threefoot SA, Hsiao BS. Temperature modulated DSC studies of melting and recrystallization in polymers exhibiting multiple endotherms. *Polymer (Guildf)*. 2000;41(3):1099-1108. doi:10.1016/S0032-3861(99)00258-X
 137. Kampert WG, Sauer BB. Temperature modulated DSC studies of melting and recrystallization in poly(oxy-1,4-phenyleneoxy-1,4-phenylenecarbonyl-1,4-phenylene) (PEEK). *Polym Eng Sci*. 2001;41(10):1714-1730. doi:10.1002/pen.10869
 138. Ivanov DA, Legras R, Jonas AM. Interdependencies between the Evolution of Amorphous and Crystalline Regions during Isothermal Cold Crystallization of Poly(ether-ether-ketone). *Macromolecules*. 1999;32(5):1582-1592. doi:10.1021/ma981220o
 139. Ivanov DA, Bar G, Dosière M, Koch MHJ. A novel view on crystallization and melting of semirigid chain polymers: The case of poly(trimethylene terephthalate). *Macromolecules*. 2008;41(23):9224-9233. doi:10.1021/ma801604a
 140. Melnikov AP, Rosenthal M, Rodygin AI, et al. Re-exploring the double-melting behavior of semirigid-chain polymers with an in-situ combination of synchrotron nano-focus X-ray scattering and nanocalorimetry. *Eur Polym J*. 2016;81:598-606. doi:10.1016/j.eurpolymj.2015.12.031
 141. Melnikov AP, Rosenthal M, Burghammer M, Anokhin D V, Ivanov DA. Study of Melting Processes in Semicrystalline Polymers Using a Combination of Ultrafast Chip Calorimetry and Nanofocus Synchrotron X-Ray Diffraction. 2016;11(11):5-6. doi:10.1134/S1995078016030113
 142. Rosenthal M, Melnikov AP, Burghammer M, Ivanov DA. Reorganization of semicrystalline

- polymers on heating: Analyzing common misconceptions in the interpretation of calorimetric data. Response on the “Comment on “Re-exploring the double-melting behavior of semirigid-chain polymers with an in-situ combinatio. *Eur Polym J.* 2017;(June). doi:10.1016/j.eurpolymj.2017.06.036
143. Melnikov AP, Rosenthal M, Ivanov DA. What Thermal Analysis Can Tell Us About Melting of Semicrystalline Polymers: Exploring the General Validity of the Technique. *ACS Macroletters.* 2018;7:1426-1431. doi:10.1021/acsmacrolett.8b00754
 144. Rosenthal M, Melnikov AP, Burghammer M, Ivanov DA. Reorganization of semicrystalline polymers on heating: Analyzing common misconceptions in the interpretation of calorimetric data. Response on the “Comment on “Re-exploring the double-melting behavior of semirigid-chain polymers with an in-situ combinatio. *Eur Polym J.* 2017. doi:10.1016/j.eurpolymj.2017.06.036
 145. Vaughan AS, Stevens GC. On crystallization, morphology and radiation effects in poly(ether ether ketone). *Polymer (Guildf).* 1995;36(8):1531-1540. doi:10.1016/0032-3861(95)98996-Z
 146. Vaughan AS, Stevens GC. On radiation effects in poly(ethylene terephthalate): a comparison with poly(ether ether ketone). *Polymer (Guildf).* 1995;36(8):1541-1547. doi:10.1016/0032-3861(95)98997-2
 147. Day M, Sally D, Wiles DM. Thermal degradation of Poly(Aryl Ether Ether Ketone): Experimental Evaluation of Crosslinking Reactions. *Appl Polym Sci.* 1990;40:1615.
 148. Baeten D, Mathot VBF, Pijpers TFJ, et al. Simultaneous synchrotron WAXD and fast scanning (chip) calorimetry: On the (isothermal) crystallization of HDPE and PA11 at high supercoolings and cooling rates up to 200 °c s⁻¹. *Macromol Rapid Commun.* 2015;36(12):1184-1191. doi:10.1002/marc.201500081
 149. Rosenthal M, Doblas D, Hernandez JJ, et al. High-resolution thermal imaging with a combination of nano-focus X-ray diffraction and ultra-fast chip calorimetry. *J Synchrotron Radiat.* 2014;21(1):223-228. doi:10.1107/S1600577513024892
 150. van Herwaarden S. Application Note for Xensor’s Calorimeter Chips of XEN-39390 Series. 2016;31(May):1-20. <http://www.xensor.nl/pdf/files/sheets/nanogas3939.pdf>.
 151. Doblas D. Doctoral thesis: Exploration and detection of ultra-traces of explosives by chip calorimetry. 2015.
 152. Rosenthal M, Melnikov AP, Rychkov AA, et al. Design of a combined setup for in-situ nanocalorimetry / nano-and micro- focus X-ray scattering to address fast structure formation processes. *Appl Mech Mater.* 2015;788:136-142.
 153. Kieffer J. pyFAI Documentation. 2016;Release 0.
 154. Kieffer J, Ashiotis G. PyFAI: a Python library for high performance azimuthal integration on GPU. 2014;(Euroscipy):3-10. doi:10.1017/S0885715613000924
 155. Kieffer J, Karkoulis D. pyFAI, a versatile library for azimuthal regrouping. Data analysis unit, European Synchrotron Radiation Facility. <https://pyfai.readthedocs.io/en/latest/pyFAI.html>.
 156. Berera R, van Grondelle R, Kennis JTM. Ultrafast transient absorption spectroscopy: Principles and application to photosynthetic systems. *Photosynth Res.* 2009;101(2-3):105-118. doi:10.1007/s11120-009-9454-y
 157. Wulff M, Kong Q, Cammarata M, et al. Picosecond diffraction at the ESRF: How far have we come and where are we going? *AIP Conf Proc.* 2007;879(February 2007):1187-1194. doi:10.1063/1.2436276
 158. Graceffa R, Accardo A, Rosenthal M, Vlasova M, Riekel C. Perspectives: DOD Inkjets at High and Ultra-Brilliant Light Sources. *NanoWorld J.* 2019;04(04):54-60.

doi:10.17756/nwj.2018-061

159. Sasuga T, Hagiwara M. Mechanical relaxation of crystalline poly(aryl-ether-ether-ketone) (PEEK) and influence of electron beam irradiation. *Polymer (Guildf)*. 1986;27(6):821-826. doi:10.1016/0032-3861(86)90288-0
160. Yoda O. Radiation Effect on Non-Crystalline Poly(Aryl-Ether-Ketone) As Revealed By X-Ray Diffraction and Thermal Analysis. *Polym Commun (Guildford, England)*. 1984;25(8):238-240.
161. Bassett DC. *Developments in Crystalline Polymers—1*. (Basset DC, ed.). Applied Science Publishers; 1982. doi:10.1007/978-94-009-7343-5
162. Rosenthal M, Melnikov A., Rychkov AA, Doblus D, Anokhin, D.V. Burghammer M, Ivanov DA. Design of an In Situ Setup Combining Nanocalorimetry and Nano- or Micro-focus X-Ray Scattering to Address Fast Structure Formation Processes. In: Mathot V, Schick C, eds. *Fast Scanning Calorimetry*. Springer; 2016:299.
163. Dimper R, Reichert H, Raimondi P, Ortiz LS, Sette F, Susini J. ESRF Upgrade Programme Phase II (2015-2022). 2015:1-194. http://www.esrf.eu/Archive_files/Upgrade/ESRF-orange-book.pdf%5Cpapers3://publication/uuid/15E113D0-D98A-4676-BEEA-DEC0A05ACBE5.